University of Alberta

Multiaxial Fatigue of an Epoxy Polymer
- Experiments and Theories

by

Gang Tao ©

A thesis submited to the Faculty of Graduate Studies and Research
in partial fulfillment of the requirements for the degree of
Doctor of Philosophy

Department of Mechanical Engineering

Edmonton, Alberta

Fall 2007

Library and
Archives Canada

Published Heritage
Branch

395 Wellington Street
Ottawa ON K1A 0N4
Canada

Bibliothèque et
Archives Canada

Direction du
Patrimoine de l'édition

395, rue Wellington
Ottawa ON K1A 0N4
Canada

Your file Votre référence
ISBN: 978-0-494-33075-3
Our file Notre référence
ISBN: 978-0-494-33075-3

NOTICE:
The author has granted a non-exclusive license allowing Library and Archives Canada to reproduce, publish, archive, preserve, conserve, communicate to the public by telecommunication or on the Internet, loan, distribute and sell theses worldwide, for commercial or non-commercial purposes, in microform, paper, electronic and/or any other formats.

The author retains copyright ownership and moral rights in this thesis. Neither the thesis nor substantial extracts from it may be printed or otherwise reproduced without the author's permission.

AVIS:
L'auteur a accordé une licence non exclusive permettant à la Bibliothèque et Archives Canada de reproduire, publier, archiver, sauvegarder, conserver, transmettre au public par télécommunication ou par l'Internet, prêter, distribuer et vendre des thèses partout dans le monde, à des fins commerciales ou autres, sur support microforme, papier, électronique et/ou autres formats.

L'auteur conserve la propriété du droit d'auteur et des droits moraux qui protège cette thèse. Ni la thèse ni des extraits substantiels de celle-ci ne doivent être imprimés ou autrement reproduits sans son autorisation.

In compliance with the Canadian Privacy Act some supporting forms may have been removed from this thesis.

While these forms may be included in the document page count, their removal does not represent any loss of content from the thesis.

Conformément à la loi canadienne sur la protection de la vie privée, quelques formulaires secondaires ont été enlevés de cette thèse.

Bien que ces formulaires aient inclus dans la pagination, il n'y aura aucun contenu manquant.

Canada

Abstract

Due to extensive utilization of epoxy polymers in industries, the durability and reliability of these materials become more and more critical issues for applications. The aim of this research project is to investigate the uniaxial and multiaxial fatigue behavior of an epoxy polymer (EPON 826/EPI-CURE Curing Agent 9551) under various loading conditions.

A fatigue testing platform, including a non-contact real-time strain measurement system based on the Digital Image Correlation Method (DICM), has been established. This system eliminates the problem brought by using the traditional extensometers, which would introduce considerable stress concentration on the surface of soft materials and thus accelerate the failure. By tracking the in-plane displacements of the pre-painted marks on the surface of the specimen, both axial strain and shear strain can be measured simultaneously in real-time mode. An optimized search algorithm enables high precision and fast data acquisition frequency in the strain measurement.

Series of uniaxial and multiaxial fatigue tests have been carried out under either stress-controlled or strain-range-controlled mode. Moreover, mean strains were superimposed in strain-range-controlled fatigue tests to investigate the mean stress/strain effect on fatigue life. Ratcheting strain effect was also studied by stress-controlled fatigue tests with mean stresses. Pure shear fatigue tests with and without mean strains, along with combined axial-shear fatigue tests with mean strains, were also performed to investigate the multiaxial fatigue behavior.

Three types of multiaxial fatigue life prediction theories, i.e. stress-based, strain-based and energy-based approaches, were examined in correlation with the comprehensive fatigue test results of the epoxy polymer studied. Mean stress/strain effect was included in these theories by incorporating mean stress/strain functions into the damage parameters. It was found that the Stassi criteria are more appropriate to evaluate the equivalent stress/strain in multiaxial fatigue for the studied polymer material which shows anisotropy in tensile and compressive behaviors. Good agreement between the prediction curves and the experimental data was obtained by using stress-based and energy-based criteria, among which the energy-based approach performed the best. Relatively large dispersion exists in the strain-based approach for the multiaxial fatigue data with mean strains, which could be attributed to its inability to account for the effect of mean stress relaxation.

Acknowledgements

I would like to express my sincere appreciation to my supervisor, Dr. Zihui Xia, for his invaluable guidance, encouragement and financial support throughout this endeavor. I would also like to thank all the members of the Advanced Composite Materials Engineering group for their help and suggestions on my research.

I wish to express thanks to Mr. Bernie Faulkner for his help on the testing equipments, Mr. Rick Bubenko for his preparation of specimens. I also wish to thank my committee members, Dr. Jason Carey and Dr. Pean-Yue Ben Jar, for their effort and valuable feedback to my thesis.

I would also like to express gratitude to my parents in China, for their encouragement and consistent support during my life. And my special thanks go to my wife, Han Wang, to whom this thesis is dedicated, for her love, understanding and patience throughout the course of the degree.

Table of Contents

1. Introduction **1**

1.1 Polymer 2

1.2 Mechanical behavior of polymers 9

1.2.1 Mechanical tests 9

1.2.1.1 Uniaxial Stress-Strain Tests 10

1.2.1.2 Creep tests 12

1.2.1.3 Stress relaxation tests 13

1.2.1.4 Dynamic mechanical tests 14

1.2.2 Constitutive modeling 16

1.3 Fatigue behavior of polymers 18

1.4 Overview of fatigue theories 27

1.4.1 Stress-based approach 28

1.4.2 Strain-based approach 29

1.4.3 Energy-based approach 30

1.4.4 Mean stress effect 32

1.4.5 Ratcheting effect 34

1.5 Objectives of current study 35

Bibliography 37

2. Fatigue testing system 45

2.1 Introduction 45

2.2 Specimens and testing system 48

2.2.1 Specimens and fabrication 48

2.2.2 Testing systems 52

2.3 Non-contact real-time strain measurement system 54

2.3.1 Principle of Digital Image Correlation Method (DICM) 54

2.3.2 Fast searching algorithm in DICM 56

2.3.3 Strain derivations 59

2.4 Preliminary test results 62

2.5 Discussions 70

2.6 Conclusions 72

Bibliography 74

3. Uniaxial fatigue behavior 77

3.1 Introduction 77

3.2 Fatigue behavior under fully-reversed loading 79

3.2.1 Strain Range – Fatigue Life relation 80

3.2.2 Evolution of mechanical properties 81

3.2.3 Preliminary tests on mean strain effect 88

3.2.4 Fatigue mechanism of the epoxy polymer 92

3.2.5 Fractographic analysis 93

3.3 Mean stress/strain effect 96

3.3.1 Overview of mean stress/strain effect 96

3.3.2 Experimental procedure 98

3.3.3 Evolution of mechanical properties 101

3.3.4 Mean stress/strain functions 109

3.3.5 Fatigue life prediction with three approaches 113

3.4 Ratcheting behavior and its effect on fatigue life 121

3.4.1 Introduction 121

3.4.2 Experimental procedure 123

3.4.3 Evolution of mechanical properties 125

3.4.4 Ratcheting effect on fatigue life 132

3.4.5 Mechanism of ratcheting strain in epoxy polymer 135

3.5 Conclusions 137

Bibliography 141

4. Multiaxial fatigue behavior 144

4.1 Introduction 144

4.2 Fully-reversed cyclic shear fatigue 146

4.2.1 Experimental procedure 146

4.2.2 Evolution of mechanical properties 147

4.2.3 Fatigue life prediction with three approaches 154

4.3 Proportional axial-shear fatigue tests with mean strains 161

4.3.1 Experimental procedure 161

4.3.2 Mechanical properties 163

4.3.3 Fatigue life prediction with three approaches 168

4.3.3.1 Equivalent Stress/Strain 169

4.3.3.2 Mean Stress/Strain Effect 170

4.3.3.3 Hydrostatic Pressure Effect 171

4.3.3.4 Fatigue Life Prediction 174

4.4 Conclusions 176

Bibliography 178

5. Summary **181**

Bibliography 186

List of Tables

Table 2.1. Physical and mechanical parameters of EPON 826/EPI-CURE Curing Agent 9551 49

Table 3.1 Test conditions and fatigue lives of strain-range-controlled uniaxial fatigue tests with same strain amplitude but different mean strain ratios 89

Table 3.2 Parameters and results of uniaxial fatigue tests with mean strains 100

Table 3.3 Parameters and results of uniaxial fatigue tests under stress-controlled mode with mean stresses 124

Table 4.1 Parameters and results of fully-reversed cyclic shear fatigue test 146

Table 4.2 Parameters and results of proportional axial-shear fatigue tests 162

List of Figures

Fig. 1.1 Structure of polymer molecules 2

Fig. 1.2 Two states of polymer molecules: (a) amorphous; (b) semi-crystalline polymers 3

Fig. 1.3 Relationship between stiffness and degree of polymerization 4

Fig. 1.4 Schematic of the molecular structures of different polyethylenes 5

Fig. 1.5 Different polypropylene structures 6

Fig. 1.6 Random conformation of a polymer chain's carbon-carbon backbone 7

Fig. 1.7 A typical molecular weight distribution of a polymer 7

Fig. 1.8 Tensile stress-strain curves of several polymers and metals 10

Fig. 1.9 Stress-strain behavior of the EPON 826/EPI-CURE 9551 at various strain rates 11

Fig. 1.10 Creep and recovery curves at different stress levels of the EPON 826/EPI-CURE Curing Agent 9551 13

Fig. 1.11 Stress relaxation tests 14

Fig. 1.12 Phase lag angle δ of stress response to an inputting sinusoidal strain 15

Fig. 1.13 Mechanical models (a) Maxwell model and (b) Voigt model 17

Fig. 1.14 Fatigue lives against $R_{\max}$ 22

Fig. 1.15 Dispersion of the N-values against $R_{\max}$ 23

Fig. 1.16 Illustration of the strain energy density components 32

Fig. 1.17 Soderberg, Goodman and Morrow's diagrams 33

Fig. 2.1 Drawings and photo of the specimens: (a) Solid specimen (for uniaxial fatigue test) ; (b) Tubular specimen (for multiaxial fatigue test); (c) Photo of solid and tubular specimens with end-tabs 51

Fig. 2.2 Fatigue testing machines: (a) A modified MTS system for biaxial fatigue test (axial, internal and external pressure); (b) A triaxial fatigue test system (axial, torsional, internal and external pressure) 53

Fig. 2.3 Configuration of the non-contact strain measurement and control system 54

Fig. 2.4 Flow chart of searching procedure of DICM in real-time strain measurement 58

Fig. 2.5 Correlation coefficient distribution in DICM at sub-pixel level 59

Fig. 2.6 A schematic illustration for strain calculation 60

Fig. 2.7 Comparison of recorded stress-strain curves by using traditional extensometer and using the non-contact real-time strain measurement and control system 62

Fig. 2.8 Stress-controlled uniaxial cyclic test with mean stress: (a) stress-strain loops of the first 5 cycles; (b) stress-strain loops of the 1st, 20th, 50th and 100th cycle; (c) maximum strains of each cycle; (d) minimum strains of each cycle 63

Fig. 2.9 Strain-range-controlled uniaxial cyclic test with mean strain: (a) stress-strain loops of the first 5 cycles; (b) stress-strain loops of the 1st, 50th and 238th cycle; (c) maximum stresses of each cycle; (d) minimum stresses of each cycle 65

Fig. 2.10 Stress-controlled pure shear cyclic test with mean stress: (a) stress-strain loops of the first 5 cycles; (b) stress-strain loops of the 1st, 100th, 1000th and 3000th cycle; (c) maximum shear strains of each cycle; (d) minimum shear strains of each cycle 66

Fig. 2.11 Proportional strain-range-controlled biaxial cyclic test under combined axial-shear loading: (a) axial stress-strain loops of the first 5 cycles and the 50th, 1000th and 1700th cycle; (b) shear stress-strain loops of the first 5 cycles and the 50th, 1000th and 1700th cycle; (c) axial mean stress in each cycle; (d) shear mean stress in each cycle 68

Fig. 2.12 Non-proportional stress-controlled biaxial cyclic test under combined axial-shear loading: (a) biaxial loading path; (b) biaxial strain response of the first 10 cycles and the 50th, 200th and 700th cycle; (c) axial mean strain in each cycle; (d) shear mean strain in each cycle 69

Fig. 2.13 Processing time of the non-contact real-time strain measurement system 70

Fig. 2.14 Histograms of the deviation of the strain range: (a) the deviation of the maximum strain; (b) the deviation of the minimum strain 72

Fig. 3.1 Strain amplitude vs. fatigue life curve from strain-range-controlled fully-reversed uniaxial fatigue tests 81

Fig. 3.2 Hysteresis loops of strain-range-controlled fully-reversed uniaxial fatigue tests: (a) The test with the highest strain range level; (b) The test with the lowest strain range level 82

Fig. 3.3 Evolutions of stress range during the entire fatigue life period of the strain-range-controlled fully-reversed uniaxial fatigue tests 84

Fig. 3.4 Evolutions of modulus during the entire fatigue life period of the strain-range-controlled fully-reversed uniaxial fatigue tests 86

Fig. 3.5 Evolutions of nonlinear strain range during the entire fatigue life period of strain-range-controlled fully-reversed uniaxial fatigue tests 87

Fig. 3.6 Evolutions of dissipated strain energy density per cycle during the entire fatigue life period of strain-range-controlled fully-reversed uniaxial fatigue tests 88

Fig. 3.7 Evolutions of stress ranges during the entire fatigue life period under the same strain amplitude but with different mean strain ratios 90

Fig. 3.8 Evolutions of modulus during the entire fatigue life period under the same strain amplitude but with different mean strain ratios 91

Fig. 3.9 Evolutions of nonlinear strain ranges during the entire fatigue life period under the same strain amplitude but with different mean strain ratios 91

Fig. 3.10 State of epoxy molecules: (a) before cyclic loading; (b) after cycle loading 92

Fig. 3.11 Fracture surface of the fatigue crack initiated from the specimen surface 94

Fig. 3.12 Fracture surface of the fatigue crack initiated from the inside of the specimen 94

Fig. 3.13 Striations in the stable fatigue crack propagation zone taken by SEM 95

Fig. 3.14 Fracture surface of the fatigue crack under tension-tension cyclic loading condition 96

Fig. 3.15 Strain amplitude vs. fatigue life of uniaxial fatigue tests with 4 different mean strain ratios 99

Fig. 3.16 Evolution of stress-strain loops of fatigue tests: (a). Test S20; (b) Test S30. 101

Fig. 3.17 Stress range evolution of all strain-range-controlled uniaxial fatigue tests with 4 different mean strain ratios: (a) $R_m = 0$; (b) $R_m = 0.33$; (c) $R_m = 1$; (d) $R_m = 2.1$. 102

Fig. 3.18 Evolution coefficient, α, vs. strain amplitude of all the strain-range-controlled uniaxial fatigue tests with 4 different mean strain ratios 103

Fig. 3.19 Mean stress relaxation of all the strain-range-controlled uniaxial fatigue tests with 4 different mean strain ratios: (a) $R_m = 0$; (b) $R_m = 0.33$; (c) $R_m = 1$; (d) $R_m = 2.1$. 104

Fig. 3.20 Stress relaxation coefficient, β, vs. strain amplitude of all the strain-range-controlled uniaxial fatigue tests with 4 different mean strain ratios 105

Fig. 3.21 Evolution of dissipated strain energy density of all the strain-range-controlled uniaxial fatigue tests with 4 different mean strain ratios: (a) $R_m = 0$; (b) $R_m = 0.33$; (c) $R_m = 1$; (d) $R_m = 2.1$. 107

Fig. 3.22 Dissipated strain energy density vs. strain amplitude of all the strain-range-controlled uniaxial fatigue tests with 4 different mean strain ratios 107

Fig. 3.23 Evolution of elastic strain energy density amplitude of all the strain-range-controlled uniaxial fatigue tests with 4 different mean strain ratios: (a) $R_m = 0$; (b) $R_m = 0.33$; (c) $R_m = 1$; (d) $R_m = 2.1$. 108

Fig. 3.24 Elastic strain energy density amplitude vs. strain amplitude of all the strain-range-controlled uniaxial fatigue tests with 4 different mean strain ratios 109

Fig. 3.25 Mean stress function with different values of material constants 112

Fig. 3.26 Mean strain function for strain approach 114

Fig. 3.27 Equivalent strain amplitude vs. fatigue life 115

Fig. 3.28 Mean stress function for stress approach 118

Fig. 3.29 Equivalent stress amplitude vs. fatigue life 118

Fig. 3.30 Mean stress function for energy approach 120

Fig. 3.31 Total strain energy density vs. fatigue life 120

Fig. 3.32 Stress-strain loops of the first 5 cycles, the mid-life cycle and the last cycle of two tests. (a). Test S1; (b) Test S7. 125

Fig. 3.33 Ratcheting strain of fatigue tests under stress-controlled mode. (a) same mean stress ratio; (b) same stress amplitude; (c) same mean stress. 127

Fig. 3.34 Ratcheting strain and ratcheting strain rate of test S7. (a) ratcheting strain; (b) ratcheting strain rate. 127

Fig. 3.35 Strain range of fatigue tests under stress-controlled mode. (a) same mean stress ratio; (b) same stress amplitude; (c) same mean stress. 129

Fig. 3.36 Dissipated strain energy density of fatigue tests under stress-controlled mode. (a) same mean stress ratio; (b) same stress amplitude; (c) same mean stress. 131

Fig. 3.37 Elastic strain energy density amplitude of fatigue tests under stress-controlled mode. (a) same mean stress ratio; (b) same stress amplitude; (c) same mean stress. 132

Fig. 3.38 Equivalent stress amplitude vs. fatigue life in stress-controlled fatigue tests with mean stresses 134

Fig. 3.39 Total strain energy density vs. fatigue life in stress-controlled fatigue tests with mean stresses 135
Fig. 3.40 Ratcheting strain of fatigue tests with and without resting period 137
Fig. 4.1 Evolution of stress-strain loop of fatigue test S2 147
Fig. 4.2 Evolutions of shear modulus during the entire fatigue life periods of strain-range-controlled fully reversed cyclic torsional fatigue tests 148
Fig. 4.3 Evolutions of shear stress ranges during the entire fatigue life periods of strain-range-controlled fully reversed cyclic torsional fatigue tests 150
Fig. 4.4 Illustration of the strain energy density components 151
Fig. 4.5 Evolutions of dissipated strain energy densities during the entire fatigue life periods of strain-range-controlled fully reversed cyclic torsional fatigue tests 152
Fig. 4.6 Evolutions of elastic strain energy density amplitudes during the entire fatigue life periods of strain-range-controlled fully reversed cyclic torsional fatigue tests 153
Fig. 4.7 Comparison of von Mises and Stassi equivalent stress envelops of Epon 826 Resin/Epi-Cure Curing Agent 9551 156
Fig. 4.8 Equivalent stress amplitude vs. fatigue life 157
Fig. 4.9 Equivalent strain amplitude vs. fatigue life 159
Fig. 4.10 Total strain energy density vs. fatigue life 160
Fig. 4.11 Illustration of biaxial principle stress ratio 163

Fig. 4.12 Stress-strain loops of test S1-5 164

Fig. 4.13 Evolution of mechanical components of test S1-5. (a) Stress amplitude; (b) Mean Stress; (c) Dissipated strain energy density; (d) Elastic strain energy density amplitude. 165

Fig. 4.14 Stress-strain loops of test S3-2. (a) Axial; (b) Shear. 166

Fig. 4.15 Evolution of mechanical components of test S3-2 in axial direction. (a) Stress amplitude; (b) Mean Stress; (c) Dissipated strain energy density; (d) Elastic strain energy density amplitude. 167

Fig. 4.16 Evolution of mechanical components of test S3-2 in shear direction. (a) Stress amplitude; (b) Mean Stress; (c) Dissipated strain energy density; (d) Elastic strain energy density amplitude. 168

Fig. 4.17 Mean stress/strain sensitivity factors 173

Fig. 4.18 Equivalent stress amplitude vs. fatigue life 174

Fig. 4.19 Equivalent strain amplitude vs. fatigue life 175

Fig. 4.20 Total strain energy density vs. fatigue life 175

Nomenclature

C	correlation coefficient
D	compliance
E	Young's modulus
$f(x_i, y_j)$	gray values of each pixel in the reference image
$g(x_i^*, y_j^*)$	gray values of each pixel in the target image
G	shear modulus
$G^{'}$	storage modulus
$G^{''}$	loss modulus
I_1	the first invariant of the stress tensor
I_1^{ε}	the first invariant of the strain tensor
$\overline{M}_n$	number average molecular weight
$\overline{M}_v$	viscosity average molecular weight
$\overline{M}_w$	weight average molecular weight
N	number of cycles
N_f	fatigue life represented by total number of cycles to failure
R	the ratio of the uniaxial compressive yield stress to the tensile yield stress
R_a	averaged size of surface defects
R_m	mean strain ratio

$R_{\max}$	maximum size of surface defects
$R_{m,stress}$	mean stress ratio
R_{stress}	stress ratio
ΔW	total strain energy density
ΔW_0	fatigue limit in terms of total strain energy density
ΔW_{eq}	equivalent total strain energy density
ΔW^d	plastic or dissipated strain energy density
ΔW^d_{avg}	averaged value of dissipated strain energy density
$\Delta W^d_{x,avg}$	averaged value of dissipated strain energy density related to the axial loading
$\Delta W^d_{xy,avg}$	averaged value of dissipated strain energy density related to the shear loading
ΔW^e	elastic strain energy density
ΔW^e_{avg}	averaged value of elastic strain energy density amplitude
$\Delta W^e_{x,avg}$	averaged value of elastic strain energy density amplitude related to the axial loading
$\Delta W^e_{xy,avg}$	averaged value of elastic strain energy density amplitude related to the shear loading
γ_a	shear strain amplitude
$\gamma_{xy,a}$	shear strain amplitude in proportional axial-shear tests

$\gamma_{xy,m}$	mean shear strain in proportional axial-shear tests
ε_{-1}	strain amplitude under fully-reversed cyclic loading at fatigue limit
ε_1^e, ε_2^e	elastic strain components in the principle directions
ε_a	strain amplitude
ε_{eq}	equivalent strain
ε_f', c	fatigue ductility coefficient and fatigue ductility exponent
$\varepsilon_{i,r}$	accumulated ratcheting strain until *i*-th cycle
ε_m	mean strain
ε_{seq}	Stassi equivalent strain
$\varepsilon_{seq,a}$	Stassi equivalent strain amplitude
$\varepsilon_{seq,m}$	mean Stassi equivalent strain
$\varepsilon_{x,a}$	axial strain amplitude in proportional axial-shear tests
$\varepsilon_{x,m}$	mean axial strain in proportional axial-shear tests
$\Delta\varepsilon$	strain range
$\Delta\varepsilon^e$	elastic strain range
$\Delta\varepsilon_{FL}$	fatigue limit in terms of strain range
$\Delta\varepsilon^p$	plastic strain range
$\Delta\varepsilon^{nl}$	nonlinear strain range
$\Delta\varepsilon^t$	total strain range
η	mean stress/strain sensitivity factor

η_σ	mean stress sensitivity factor in stress-based approach
η_ε	mean strain sensitivity factor in strain-based approach
η_W	mean stress sensitivity factor in energy-based approach
υ	Poisson's ratio
σ_{-1}	stress amplitude under fully-reversed cyclic loading at fatigue limit
σ_1, σ_2	principle stress components
σ_a	stress amplitude
σ_{eq}	equivalent stress
$\sigma_f^{'}$, b	Basquin coefficients
σ_{FL}	fatigue strength limit
σ_m	mean stress
σ_{seq}	Stassi equivalent stress
$\sigma_{seq,a}$	Stassi equivalent stress amplitude
$\sigma_{seq,m}$	mean Stassi equivalent stress
σ_u	ultimate strength
$\sigma_{x,a}$	axial stress amplitude in proportional axial-shear tests
$\sigma_{x,m}$	mean axial stress in proportional axial-shear tests
σ_y	yield stress
$\Delta\sigma$	stress range
τ_a	shear stress amplitude

$\tau_{xy,a}$	shear stress amplitude in proportional axial-shear tests
$\tau_{xy,m}$	mean shear stress in proportional axial-shear tests
χ	hydrostatic stress ratio
ψ	damage parameter
ψ_0	fatigue limit

Chapter 1

Introduction

Polymers have been extensively utilized in modern industries due to some superior advantages over conventional materials. A good example is polymeric matrix composite materials, which possess high specific stiffness and strength, high corrosion resistance and good fatigue strength. From the mechanics point of view, to serve as load bearing parts in structures, the complicated mechanical behaviors of polymers need in-depth investigations to avoid catastrophic failure and disastrous accident. Research on the mechanical response, creep and damage modes, along with constitutive modeling of the polymers, would increase prediction reliability and hence efficiently optimize the application. Among mechanical behaviors, fatigue would be a significant concern for structures under cyclic loading conditions, which is ubiquitous in practical applications. Since in most cases, fatigue cracks usually initiate within the matrix in polymer composites, research on fatigue behavior of polymers would be crucial for well understanding the fatigue property of polymer-reinforced composite materials. The objective of this study is to investigate the fatigue behavior of one of the most commonly used epoxy polymer in the composite material industry, under various uniaxial and multiaxial cyclic loading conditions.

1.1 Polymer

The first production of natural polymers dates back centuries ago; however, it was not until the 20th century that mass production of synthetic polymers occured and the modern industries were greatly influenced by the extensive utilization of polymeric materials. Ease of manufacturing process makes synthetic polymers superior to most conventional materials, such as metals, and hence polymers can be used as alternatives to them in many applications. As the name itself states, polymers are generally referred to macromolecules composed of a large amount of monomers connected by covalent bonds along the chain. The structures of polymer molecules can be generally classified into three categories: linear, branched and cross-linked, shown as Fig.1.1.

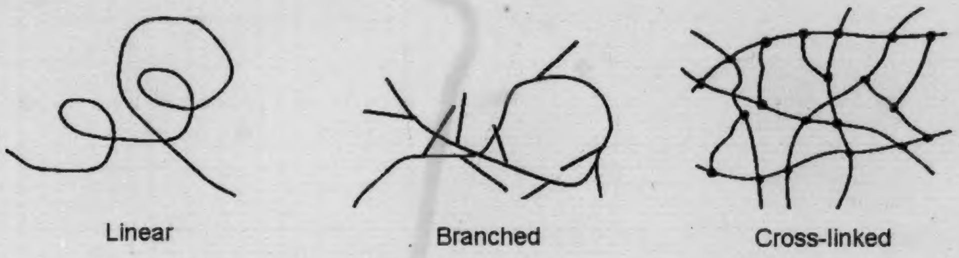

Fig. 1.1 Structure of polymer molecules (adopted from Anderson, 1991)

According to various criteria, polymers can be classified into different categories. Generally, all polymers can be placed into natural macromolecules and synthetic polymers categories. Within synthetic polymers, there are three types: thermoplastics, thermosets and rubbers (also called elastomers). The molecular structure of thermoplastics is uncrosslinked and they can be melted and solidified many times, while thermosets cannot be melted or dissolved due to its cross-linked molecular structure. For different arrangement of molecular chains, polymers can also be classified into two classes: amorphous and semi-crystalline polymers as shown in Fig.1.2. The molecules of amorphous polymers remain disordered as they cool. However for semi-crystalline polymers, some molecules are highly oriented and regularly arranged in crystalline phase and some remain disordered in amorphous phase.

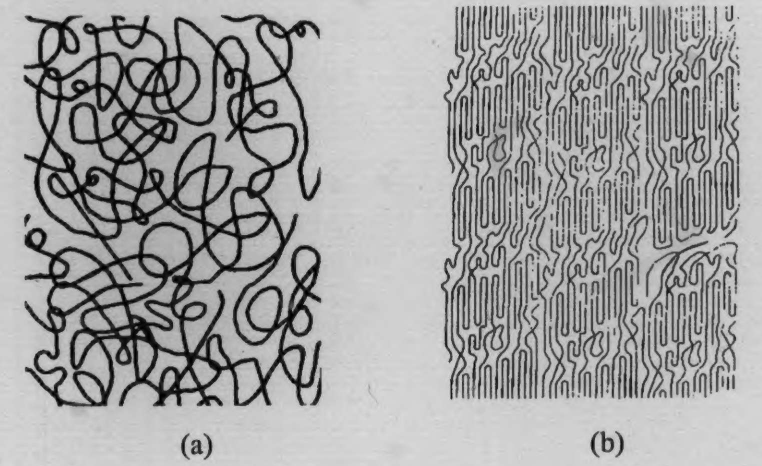
(a) (b)

Fig. 1.2 Two states of polymer molecules: (a) amorphous; (b) semi-crystalline polymers (adopted from Kausch, 1987)

Besides the chemical composition, the size of the polymer molecules has a great effect on the properties of polymers. The size of the molecules can be reflected by the degree of polymerization (DP) defined as:

$$DP = \frac{M}{M_0} \tag{1.1}$$

where M is the averaged molecular weight and M_0 is the formula weight of the repeating unit. The mechanical properties of polymers are affected by the molecular weight, and therefore they are also affected by the DP. For example, generally, the effect of molecular weight or DP on stiffness of polymers is schematically shown in Fig.1.3 (Rudin, 1999).

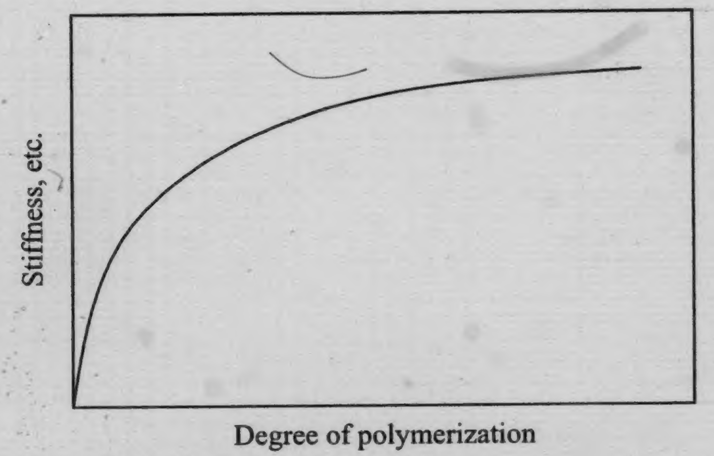

Fig. 1.3 Relationship between stiffness and degree of polymerization

In addition to chemical composition and DP, molecular architecture affects the properties of polymers significantly. Isomerism, defined as a phenomenon that substances have identical molecular formula but different structures, widely exists in polymers. There are three types of isomerism in polymers: constitutional, configurational and conformational. Constitutional isomerism usually results from different branching of the polymer chains. Figure 1.4 shows the branching architecture of high density, low density and linear low density polyethylenes, respectively.

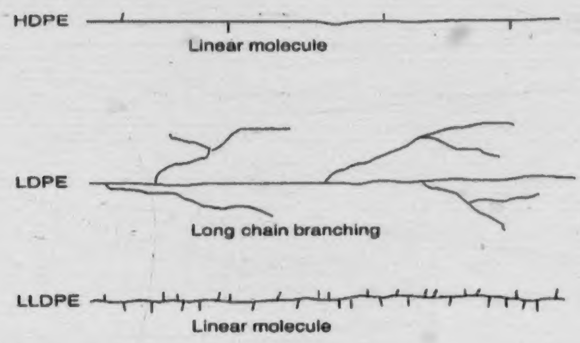

Fig. 1.4 Schematic of the molecular structures of different polyethylenes (modified from Osswald, 2003)

With the same constitution, polymers can have different configurational structures. The configuration gives information about the distribution and spatial organization of the molecule. As shown in Fig.1.5, the CH_3 groups can be placed in different directions resulting in different polypropylene molecular structures. The order in which they are arranged is called the tacticity. The polymers whose side groups are all on the same side are called isotactic, and those molecules with regularly alternating side groups are called syndiotactic. While the polymers with side groups that are placed randomly are called atactic. Both isotactic and syndiotactic polymers can crystallize, while atactic polymers cannot crystallize.

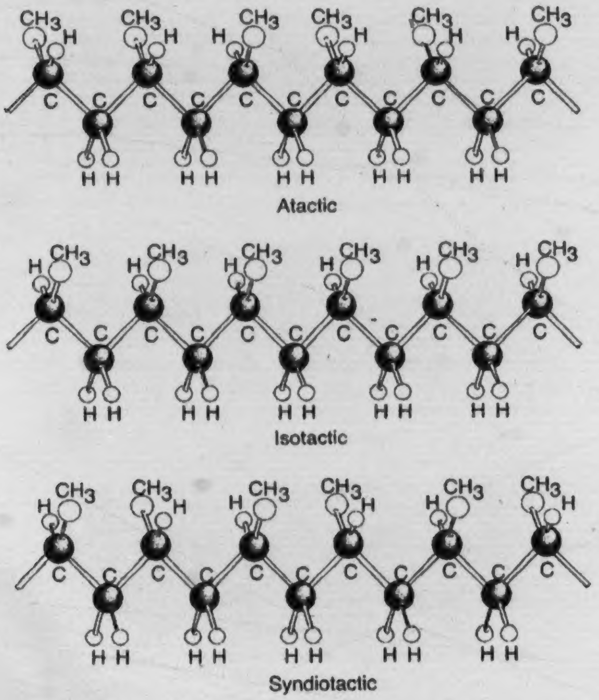

Fig. 1.5 Different polypropylene structures (adopted from Osswald, 2003)

Given the same constitution and configuration, polymer molecules can adopt different spatial arrangement because of rotation about single bonds. As shown in Fig.1.6, the tetrahedral geometry of carbon atoms results in a 109.5° bond angle. This angle is maintained between carbon atoms on the backbone of a polymer molecule and each bond is free to rotate. Both constitution and configuration are controlled by polymerization process. However, conformation is affected by the processing conditions and temperature.

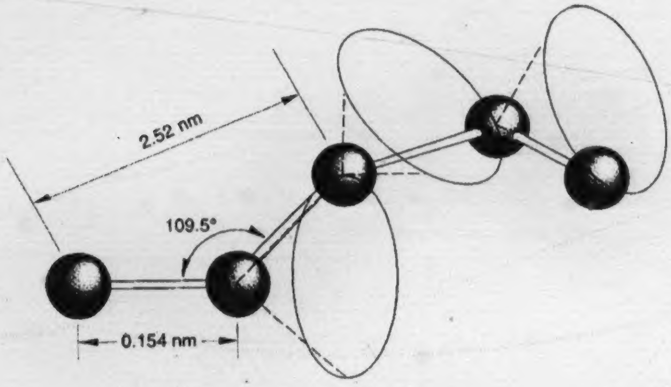

Fig. 1.6 Random conformation of a polymer chain's carbon-carbon backbone (adopted from Osswald, 2003)

Molecular weight is one of the important parameters of polymers. Usually a polymer may consist of chains of various lengths. A typical molecular weight distribution in a polymer is shown in Fig.1.7. Mechanical and processing properties of polymers are sensitive to both molecular weight and molecular weight distributions (Osswald, 2003).

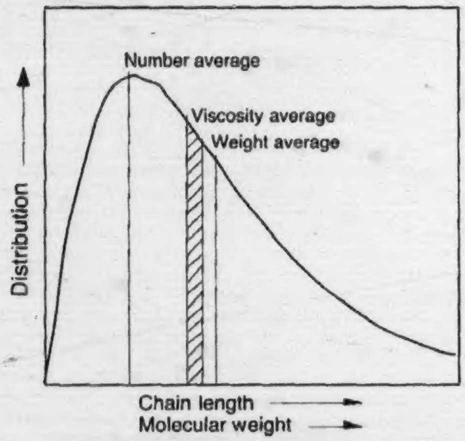

Fig. 1.7 A typical molecular weight distribution of a polymer (adopted from Osswald, 2003)

Various forms of molecular weight can be defined, Such as the number average molecular weight, weight average molecular weight and viscosity average molecular weight defined in Eq.(1.2), Eq.(1.3) and Eq.(1.4), respectively.

$$\overline{M}_n = \frac{\sum_i n_i M_i}{\sum_i n_i} \tag{1.2}$$

$$\overline{M}_w = \frac{\sum_i n_i M_i^2}{\sum_i n_i M_i} \tag{1.3}$$

$$\overline{M}_v = \left(\frac{\sum_i n_i M_i^{1+\alpha}}{\sum_i n_i M_i} \right)^{\frac{1}{\alpha}} \tag{1.4}$$

where n_i is the number of molecules with molecular weight of M_i, α is a material dependent parameter related to the intrinsic viscosity. For a monodisperse polymer sample composed of a single weight molecule species, one can obtain:

$$\overline{M}_w = \overline{M}_v = \overline{M}_n \tag{1.5}$$

And for a polydisperse polymer containing molecules with a range of molecular weights, one find:

$$\overline{M}_w > \overline{M}_v > \overline{M}_n \tag{1.6}$$

For a polydisperse polymer, the values of $\overline{M}_n$, $\overline{M}_w$ and $\overline{M}_v$ are schematically shown in Fig.1.7. A measure of broadness of a polymer's molecular weight distribution is the polydispersity index which is defined as:

$$PI = \frac{\overline{M}_w}{\overline{M}_n} \tag{1.7}$$

The lowest PI reported in laboratory is 1.04, which is obtained by anionic polymerization of styrene in laboratory. Normally, the polydispersity index of commercial polymers ranges from 1.5 to 20.

1.2 Mechanical behavior of polymers

Due to the unique macromolecular structures of polymers, their mechanical behavior can be complicated. Compared with those of metals, polymer properties show a much stronger dependence on temperature and time. This strong time and temperature sensitivity of polymer properties is a consequence of their viscoelastic nature. To understand their mechanical responses under complex loading conditions, experimental characterization and constitutive modeling of the polymers has been performed (Brown, 1986, Chen et al., 2005, Hu et al., 2003, Knauss et al., 1987, Krishnaswamy et al., 1992, Kwon et al., 2005, Shen et al., 2004, Xia et al., 2003, 2005a, 2005b, among others).

1.2.1 Mechanical tests

A variety of test methods exist to determine the mechanical performances of polymeric materials under various loading conditions. These range from simple tension, compression, and shear tests to those designed to test complex stress states and polymer time-temperature response. In this section, some typical mechanical tests mostly utilized to determine the viscoelastic behavior of polymers are briefly introduced.

1.2.1.1 Uniaxial stress-strain tests

The most commonly used mechanical test is the uniaxial test, in which the specimen is deformed under tensile or compressive load at a constant rate (stress, strain or displacement). The stress-strain data are recorded simultaneously. Polymers exhibit a wide variation of behavior in stress-strain tests as shown in Fig.1.8, where the stress-strain curves of copper and steel are also presented for comparison.

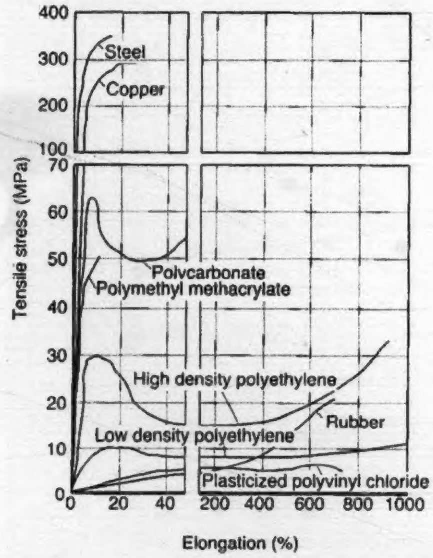

Fig. 1.8 Tensile stress-strain curves of several polymers and metals (adopted from Osswald, 2003)

One can see that most polymers exhibit much higher ultimate strains than metals, although their ultimate strengths are usually lower. The utility of stress-strain tests for design with polymeric materials can be greatly enhanced if tests are carried out over a wide range of temperatures and strain rates. As shown in Fig.1.9, the epoxy polymer studied in this work exhibits variation in mechanical responses under various loading rates at room temperature (Hu, 2002).

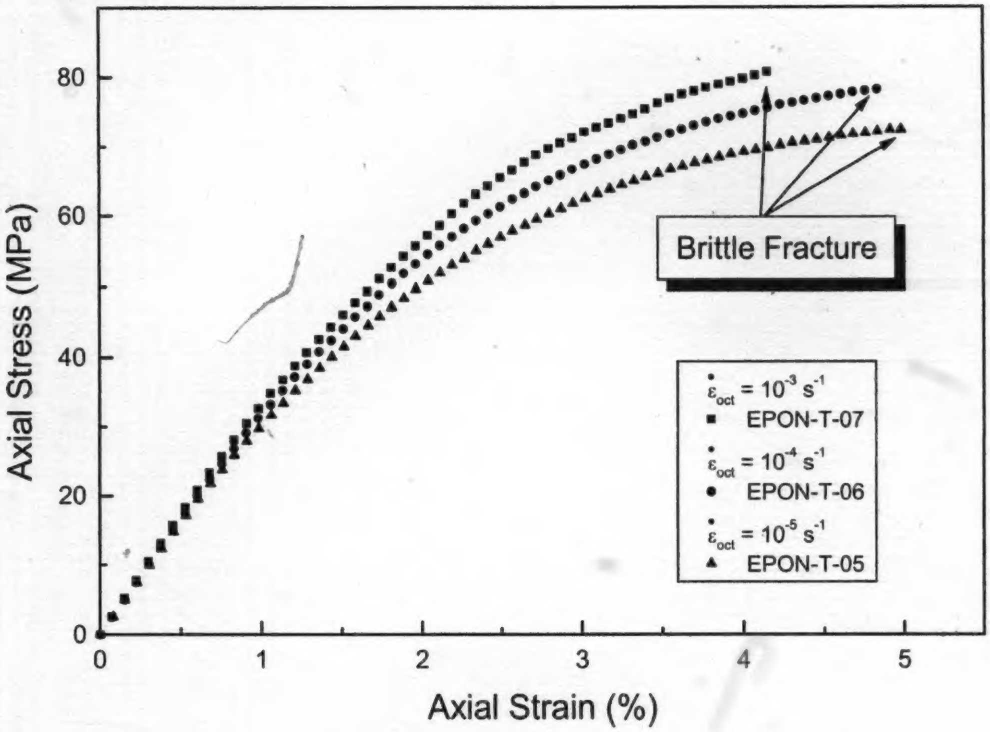

Fig. 1.9 Stress-strain behavior of the EPON 826/EPI-CURE 9551 at various strain rates (adopted from Hu, 2002)

1.2.1.2 Creep tests

In a creep test, a specimen is subjected to a constant load, and the strain is measured as a function of time. The creep test can be conducted under tensile, compressive or torsional load. An important parameter called creep compliance is mostly of interest to engineers:

$$D(\sigma_0, t) = \frac{\varepsilon_a(t)}{\sigma_0} \tag{1.8}$$

where σ_0 is the applied constant stress and $\varepsilon_a(t)$ is the corresponding creep strain. Once the load is removed, a continuously decrease of strain would occur following an initial elastic recovery. Creep-recovery curves may be used to characterize the material parameters and/or functions for some viscoelastic constitutive models, see e.g. Lou and Schapery (1971). Series of creep-recovery tests on the epoxy polymer investigated in this work have been performed by Hu et al. (2002) at various stress levels as shown in Fig.1.10.

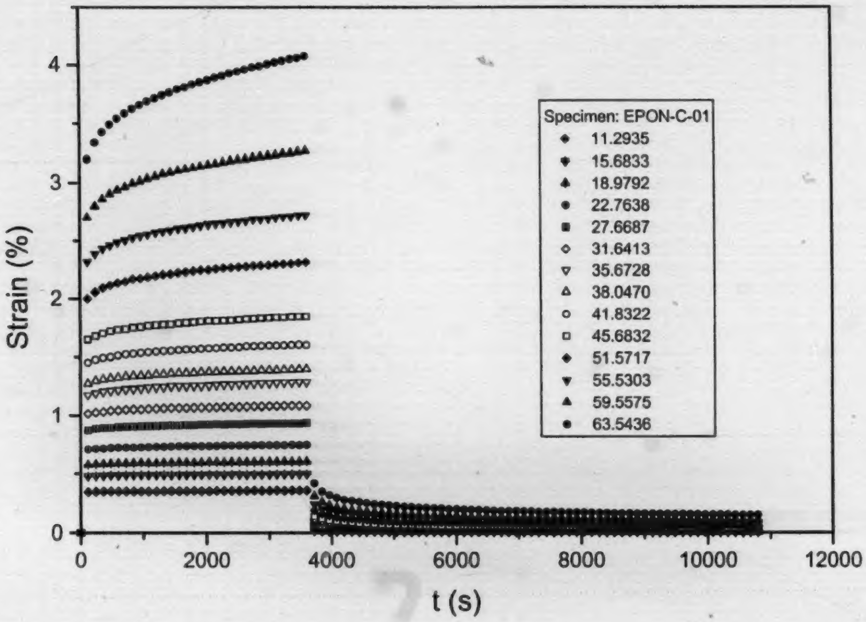

Fig.1.10 Creep and recovery curves at different stress levels of the EPON 826/EPI-CURE Curing Agent 9551 (adopted from Hu, 2002)

1.2.1.3 Stress relaxation tests

When an instantaneous strain is applied to a specimen, an initial stress level would be achieved and followed by a trend of decrease with time, as seen in Fig.1.11. Stress relaxation modulus can be defined as the ratio between the stress and strain:

$$E(\varepsilon_0, t) = \frac{\sigma_a(t)}{\varepsilon_0} \tag{1.9}$$

where $\sigma_a(t)$ is the stress as a function of time and ε_0 is the applied constant strain. Stress relaxation tests also provide useful information about the viscoelastic nature of polymers.

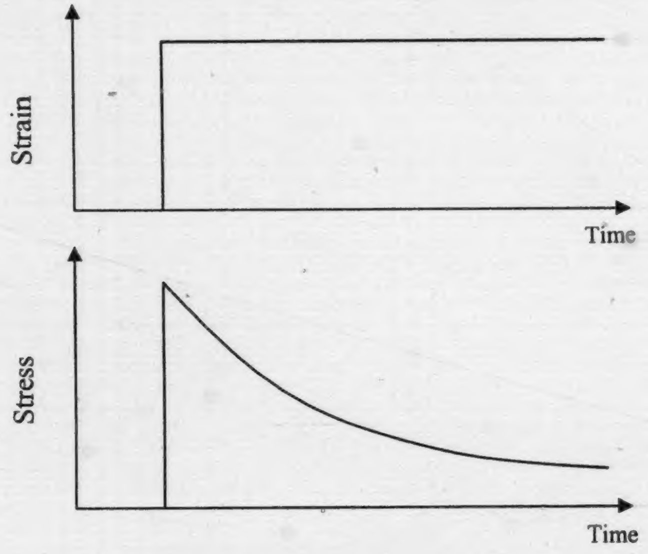

Fig. 1.11 Stress relaxation tests

1.2.1.4 Dynamic mechanical tests

Creep and stress relaxation tests may require a long time to acquire the complete description of the viscoelastic properties of a material. Therefore, an alternative experimental procedure is dynamic mechanical test, where the specimen is subjected to an alternating strain and the stress is simultaneously measured. If a sinusoidal strain is inputted, the resulting stress will be also sinusoidal. For an elastic material, the stress and strain will be in phase. However, for polymers, they are usually out of phase due to the viscoelastic nature as shown in Fig.1.12.

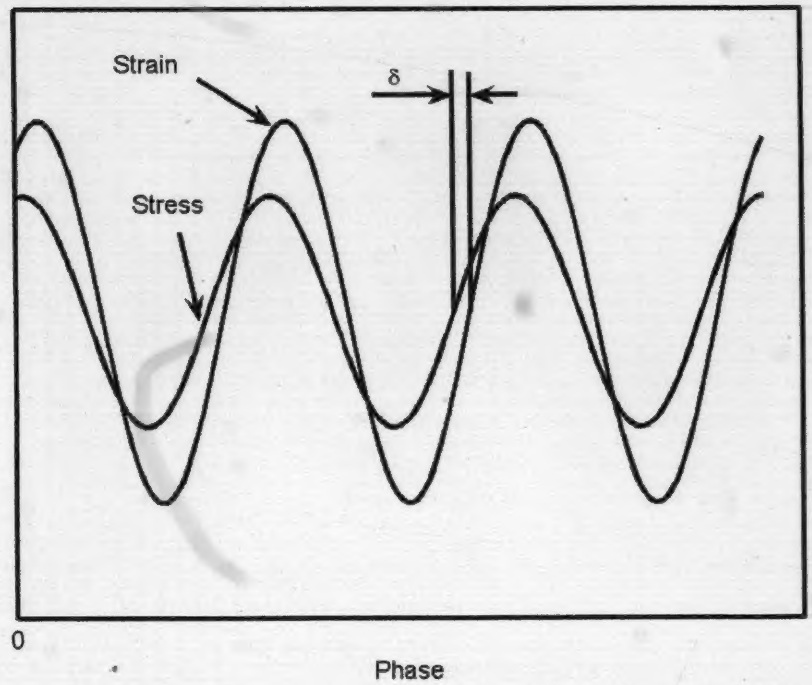

Fig. 1.12 Phase lag angle δ of stress response to an inputting sinusoidal strain

The stress can be decomposed into two components, in-phase and 90° out-of-phase parts, respectively. The storage modulus $G^{'}$ is then defined as the ratio of the in-phase stress amplitude to the strain amplitude. The loss modulus $G^{''}$ is the ratio of the out-of-phase stress amplitude to the strain amplitude. Both $G^{'}$ and $G^{''}$ are functions of the loading frequency. And the relationship between the phase angle and $G^{'}$ and $G^{''}$ is:

$$\tan\delta = \frac{G^{''}}{G^{'}} \tag{1.10}$$

Physically, $\tan\delta$ denotes the material damping characteristics. It is a measure of the ratio of the energy dissipated as heat to the maximum energy stored in the material during one cycle of oscillation.

1.2.2 Constitutive modeling

Many attempts have been made on the modeling of the constitutive relation of polymers. In general, those models can be classified into two categories: linear viscoelastic and nonlinear viscoelastic, In linear viscoelastic case, the ratio of stress to strain is independent of the stress or strain. For instance, in creep tests of a linear viscoelastic material, the creep compliance Eq.(1.8) is only a function of time (Krishnaswamy et al., 1992).

The models to be discussed here will be limited to the phenomenological approaches and are independent of the structural details of the materials. Two mechanical components, a spring element and a dashpot, are usually adopted to simulate the elastic solid and Newtonian flow behaviors of materials. Two combinations of the spring and dashpot result in two simple models, Maxwell model and Voigt model as shown in Fig.1.13.

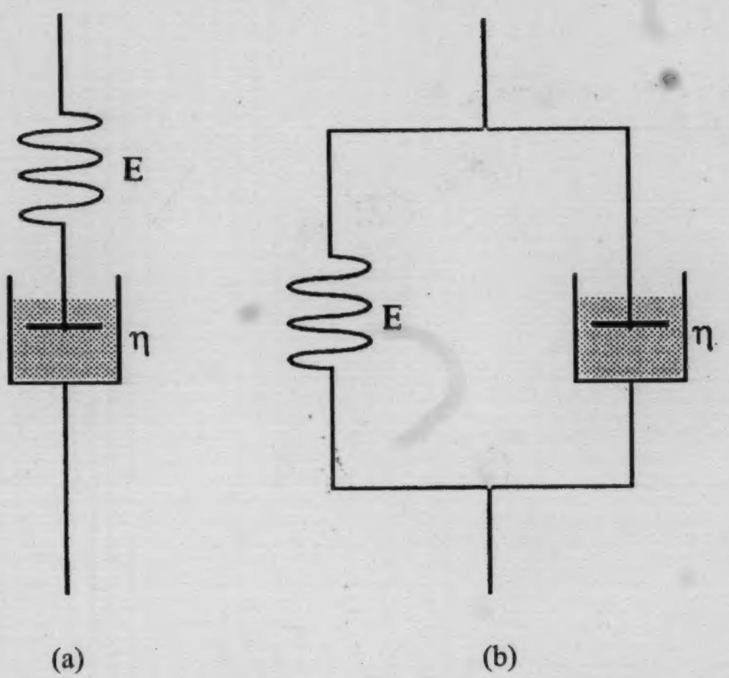

Fig. 1.13 Mechanical models (a) Maxwell model and (b) Voigt model

The equations of motion of Maxwell model and Voigt model are expressed in Eq.(1.11) and Eq.(1.12), respectively.

$$\frac{d\varepsilon(t)}{dt} = \frac{1}{E}\frac{d\sigma(t)}{dt} + \frac{\sigma(t)}{\eta} \tag{1.11}$$

$$\sigma(t) = \varepsilon(t)E + \eta\frac{d\varepsilon(t)}{dt} \tag{1.12}$$

However, a single Maxwell or Voigt model may not precisely represent the mechanical response of a viscoelastic material. Arbitrary combination of numbers of Maxwell and Voigt models can be adopted. In addition, to reflect the nonlinear viscoelastic nature of the epoxy polymer, an attempt has been made to let the elastic modulus of the spring in

Voigt elements as a function of the equivalent stress in Xia's differential model (2003). There have also been some other constitutive models, such as the Scahpery's integral model (1969a, 1969b) and its modification by Lai and Bakker (1996), the free volume approach by Knauss and Emri (1981, 1987). For the EPON 826/EPI-CURE Curing Agent 9551, which is investigated in this work, Xia's differential model exhibits good performance in predicting complicated viscoelastic deformation behavior of the epoxy polymer (Xia et al., 2003, 2005a, 2005b).

1.3 Fatigue behavior of polymers

In most practical applications, engineering materials are subjected to cyclic loadings. The micro structures of the materials could change over time, which would lead to the initiation of local defects. The continuous growth of these defects would finally evolve to macro-scale cracks and result in structural failure. This phenomenon is called fatigue. The extensive use of engineering materials over a wide range of applications has generated extraordinary interest in the deformation behavior and fatigue durability of these materials under uniaxial and multiaxial loading conditions. Estimation of fatigue life under various multiaxial loadings has been a challenging task for researchers over the last several decades.

Due to extensive utilization of epoxy polymers in modern industries, the research on fatigue behavior of epoxy polymer materials appears to be quite important for understanding fatigue damage mechanisms and avoiding catastrophic failure of load-bearing components made of epoxy polymers. For epoxy polymeric composite, fatigue crack usually initiates from the relatively weak epoxy matrix or interface between the epoxy matrix and reinforcing phase (Gamstedt et al., 2001). Therefore, in-depth investigation on fatigue behavior of epoxy polymers also helps in understanding the fatigue failure of such composite materials. There have been numerous publications on fatigue behaviors of epoxy composite materials (Lifshitz, 1988, Gilchrist et al., 1999, Kaynak et al., 2001, Al-Assaf et al., 2007, Qi et al., 2007). There were also many research works on fatigue behavior of thermoplastics (Takemori, 1984, Liang, 1996, Kawagoe, 1997, Wang, 2001, Kwon, 2005). However, there have been relatively few studies on fatigue behavior of pure epoxy polymers. Some of the works on fatigue behavior of epoxy polymers are reviewed in this section.

Nagasawa et al. (1995) have studies the mechanical fatigue mechanism of E828 epoxy resin (a bisphenol A/epichlorohydrin type epoxy). Cyclic fatigue tests and static fatigue tests (a static load was applied) have been carried out. No meaningful difference was found in S-N curves (stress amplitude – number of cycle to failure curves) for different degree of cross-linking in rotary bending fatigue tests. While in static fatigue, the critical stress under which no fatigue failure occurs, as well as the tensile and bending strength, is dependent of the degree of cross-linking. A clear difference was observed on the fracture surface of annealed and unannealed samples. SEM of a fracture surface in rotary-bending fatigue tests clearly showed the crack nuclei on the surface of the specimen, but not the extended flaws inside the material. Three regions were observed on the fracture surface: nucleation of the crack, crack propagation region and final fracture region. They found that some strain may be accumulated on the surface of the specimen through cyclic deformations. But the strain accumulated is recoverable. In their rotary-bending fatigue tests, the procedure was interrupted at 80% of the expected life time of the specimens. Subsequently, the specimens were rested for one night at room temperature or at glass transition temperature and then well polished before being subjected to the same rotary-bending fatigue tests. The same treatment was repeated ten times for each specimen. No specimen ruptured during this period. It was assumed that fatigue accumulated during this period is reversible and can be fully healed if provided enough time to rest. Furthermore, under a metallurgical microscope, they confirmed that no visible defects were created on the surfaces of those specimens before they fractured. They concluded that the nucleation of a fatal crack may occur at the instant before the visible failure of the specimen. The life of the specimen is mainly determined by the period required for incubation of a crack. The temperature effect was also studied in their experiments. With the increase of the loading frequency and loading amplitude, the temperature of the surface of the specimen increased. And the S-N curves were obtained at room temperature and 100℃, respectively. It was shown that specimen life at 100℃ will be less than that at room temperature. They also confirmed that the S-N curves obtained in argon atmosphere had no significant difference to that obtained in air. This showed that cyclic fatigue of epoxy resins is neither due to air oxidation nor air vapor hydrolysis. Two kinds of atomic bonds must be broken for fracture of epoxy resin: primary covalent bonds in the main chain and secondary bonds such as van der Waal's force and dipole interaction working between segments. The factor controlling specimen life in rotary bending fatigue test may be the secondary forces working between segments or the state of the segment packing on the surface because of the fact found in their experiments that the degree of cross-linking has little effect on the S-N curves. It seems that a reversible strain may be accumulated in the state of arrangement of secondary bonded segments. The distorted segment arrangement can return to the original state due to the contractile force of the network structure. If the reversible strain turns into an irreversible defect, it cannot return to its initial state but would initiate a crack. Such a transition seems to be possible in epoxy resins, considering that epoxy resins are in a glassy state and have interstitial vacancies. Irreversible transitions may be induced in such vacancies.

Trotignon et al. (1991) studied the roughness effects on the fatigue behavior of an epoxy matrix, which was based on diglycicyl ether of bisphenol A (DGEBA) with a degree of polymerization close to zero and the stoichiometric concentration of diaminodiphenyl methane (DDM). It was found that the most important parameter is the maximum size of the defects $R_{\max}$. Static tests were performed on two different sample families with different $R_{\max}$. Although the flexural modulus remained unchanged, the flexural strength and tensile strength appeared to be enhanced by polishing. However, under a certain stress amplitude level, the increase of fatigue life was distinctive with the decrease of $R_{\max}$ as shown in Fig1.14 and followed the relationship as Eq.(1.13).

$$\ln N = 1 + 20R_{\max}^{-1} \tag{1.13}$$

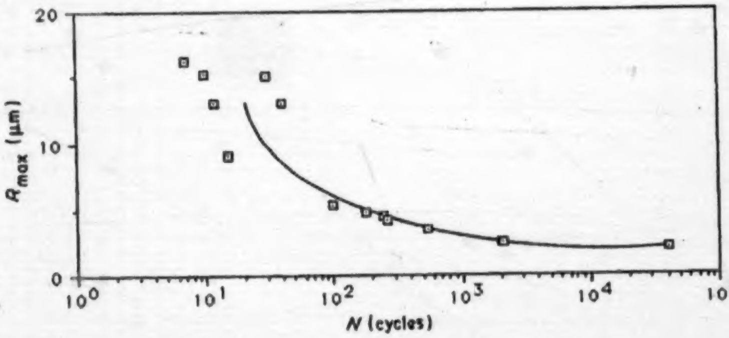

Fig. 1.14 Fatigue lives against $R_{\max}$ (adopted from Trotignon et al., 1991)

Note that the coefficient in Eq.(1.13) depends on the loading conditions, especially the stress amplitude. They also found that the dispersion, Eq.(1.14), on N-values (for given fatigue test conditions) is an increasing function of $R_{\max}$ as shown in Fig.1.15.

$$D = \frac{N_{\max} - N_{\min}}{N_{aver}} \tag{1.14}$$

where $N_{\max}$, $N_{\min}$ and N_{aver} are the maximum, minimum and average number of cycles to rupture.

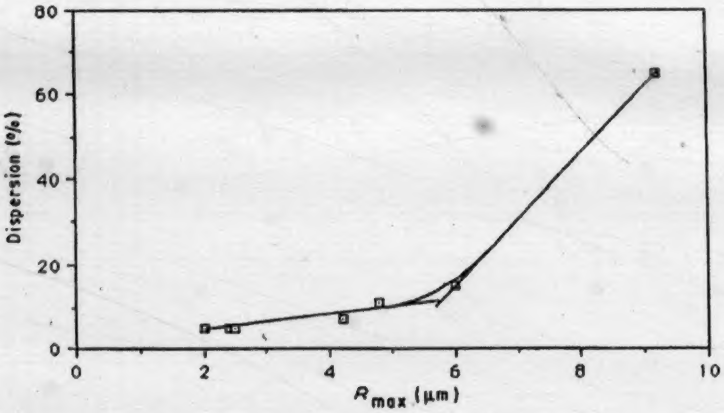

Fig. 1.15 Dispersion of the N-values against $R_{\max}$ (adopted from Trotignon et al., 1991)

Therefore, a "critical roughness" could be defined under which acceptable results can be obtained. In this case, 5 to 6 μm of the size of the maximum surface defects is the critical value under which 10% dispersion ratio can be achieved.

The effect of ductility on the fatigue behavior of epoxy resins has been studied by Lorenzo et al. (1986). Two kinds of DGEBA-based (diglycidyl ether of bisphenol A) epoxy resins, ductile Epon 815/Versamid 140 and brittle Epon 828/Epon Z, were investigated. Ductility of Epon 815/Versamid 140 mixture is due to the introduction of flexibilizer and the presence of large molecular chains with low crosslink density because of large spacing between crosslink points. The brittle Epon 828/Epon Z system has shorter spacing between reacting points and presents aromatic rings along the chain that restrict segmental motions, reducing chain flexibility. All the fatigue tests were performed under load-controlled mode with sinusoidal waveform and stress ratio R of 0.1. Permanent residual strains were observed for both epoxies after cyclic loading, where the ductile epoxy exhibited larger permanent strain than the brittle epoxy. The failed specimens showed residual fringes and yield bands under polarized light, which is a clear evidence of non-elastic deformation. In the static testing, micro-cracks normal to the loading direction were observed on the surfaces of both ductile and brittle epoxies. The micro-cracks propagated stably from the imperfections on the external surfaces of the ductile epoxy; while in the brittle epoxy, micro-cracks did not develop. Yield bands oriented at 45° with respect to the applied load were observed to grow from large crystal colonies. Band length hardly increased in brittle epoxy specimens that failed before yielding. However, at fast loading rates, neither ductile nor brittle specimens showed any growth of micro-cracks. In fatigue tests, dispersed micro-cracks did not develop in either epoxy regardless of the stress level. Three regions were distinguished on the fracture surface. Discontinuous crack growth bands and striations were seen in the stable crack growth region. The distance between bands and band width increased with increase of the distance from the crack initiation site. Band width was typically larger in ductile epoxy specimen. The striation corresponds to the growth of the crack in one cycle; however, they were not always present on the fatigue fracture surface of the epoxies, especially in very brittle epoxy.

Sauer (1980) performed an extensive review of research on fatigue of various polymers up to 1980. Molecular mechanisms and micromechanics aspects of the fatigue fracture process were described in this review. Thermal fatigue, mechanical fatigue, effects of various experimental (external) variables and material (internal) variables were summarized. The external variables include stress amplitude, stress intensity factor range, frequency, mean stress, temperature, surface condition and environment (aging time and moisture content). Internal variables, such as polymer structure, viscoelastic characters, molecular weight, molecular weight distribution, rubber inclusions, fillers and diluents were mentioned. These variables may influence fatigue behavior of different polymers, depending on their composition and structure, in markedly different ways.

In addition, there was also published research addressing particular aspects of polymer under cyclic/fatigue loading. The mean stress effect on fatigue behavior of polystyrene was investigated by Sauer et al. (1976). Clark et al. (1993) studied the effect of molecular weight and mean stress on the fatigue mechanism in poly(methyl methacrylate). Chen et al. (2005) investigated the ratcheting behavior of PTFE under cyclic compression loading conditions.

Although some research has been carried out on various epoxy polymers, there is still no systematic investigation on fatigue behavior and fatigue life prediction models of epoxy polymers under various multiaxial loading conditions. Some critical issues relating to the fatigue behavior of epoxy materials have not been carefully investigated, for example, the effects of various loading conditions (stress/strain controlled mode, mean stress/mean strain, ratcheting strains/stress relaxation, multiaxial loading paths etc.), or the evolution of various mechanical properties during cyclic loading process (drop of elastic modulus, cyclic hardening or softening, etc.). These factors are expected to have significant influence on the fatigue property of epoxy materials because of their distinct viscoelastic nature as described in previous investigations (Hu et al., 2003, Shen et al., 2004, Xia, 2005b). The insufficiency in research on fatigue of epoxy polymer may be partly attributed to the unavailability of an effective technique to accurately measure strain during the entire fatigue testing of soft polymer specimens. Extensometers have been commonly used as strain measurement devices in fatigue tests for metals and other relatively hard materials; however, they are not suitable for fatigue tests of flexible materials such as polymers. The knives of the extensometers can introduce stress concentration on the specimen surface and accelerate failure even with a protective cloth on the specimens' surface. Not surprisingly, almost all previous fatigue tests of polymers were conducted under stress-controlled mode or displacement-controlled (by controlling a certain global displacement, such as grip displacement or rotation angle) mode (Ives et al., 1971, Brown, 1986). The actual strains in the gauge area could not be carefully monitored for the entire fatigue test process; thus, it was difficult to make an accurate assessment on the change in mechanical properties during the cyclic fatigue process. Kanchanomai et al. (2002) pioneered use of a digital image system in strain-range-controlled uniaxial fatigue tests of solder materials. However, the precision of their measurement suffered from the ambiguity of the mark edges. Therefore, as claimed in the reference, the minimum detectable strain was only 0.08%. Furthermore, this method has not been applied to multiaxial fatigue test. Therefore, it is important to develop an effective non-contact strain measurement system for study on fatigue behavior of polymeric materials. Based on the measurement system, a fatigue testing platform for uniaxial and multiaxial fatigue tests of polymers can be established. Then fatigue behavior of the epoxy polymer under various loading conditions, including mean stress/strain effect, ratcheting effect under uniaxial or multiaxial loading conditions, can be investigated.

1.4 Overview of fatigue theories

Fatigue failure problems were brought to attention since the advent of industrial revolution where mechanical devices were subjected to repeated loading. Increasing demands were addressed to prevent the fatigue failure in load bearing components. The first systematic study on metal fatigue was done by Wöhler on rotating axles (1871). Since that, most fatigue data have been presented in the form of S-N curves in the semi-log or log-log scale, where S is the engineering stress amplitude and N is the number of cycles to failure. There have been several topics in fatigue research, such as high- and low-cycle fatigue, fatigue of notched members and the fatigue crack propagations. Majority of investigations have been focused on the phenomenological aspect of fatigue life predictions. No distinction is made between the crack initiation and propagation phases in this approach. Efforts have been concentrated on defining an appropriate damage parameter ψ, by which a best correlation can be obtained with the fatigue life represented by number of cycles to failure. The typical relationship between damage parameter and fatigue life can be expressed as:

$$\psi = \kappa \cdot (N_f)^{\gamma} + \psi_0 \tag{1.15}$$

where N_f is the fatigue life represented by total number of cycles to failure, κ and γ are material constants, ψ_0 is the fatigue limit which defines a certain level of damage parameter under which the specimen may reach infinite life. Generally, the phenomenological fatigue theories can be classified into three categories, stress-based, strain-based and energy-based approaches, depending on the kind of chosen damage parameter which can be the function of stress, strain or strain energy density (Ellyin, 1997).

1.4.1 Stress-based approach

Stress-based approach was firstly adopted by Wöhler in 1871, where the engineering stress amplitude was selected as the damage parameter. Taking the true stress amplitude as the damage parameter, the relation proposed by Basquin (1910) can be expressed as:

$$\sigma_a = \Delta\sigma/2 = \sigma'_f \left(N_f\right)^b \tag{1.16}$$

where $\sigma_f^{'}$ and b are Basquin coefficients evaluated by best fit technique from experimental data. The fatigue limit of certain metals can be accounted by introducing a fatigue strength limit σ_{FL} and it will result in:

$$\sigma_a = \sigma_f^{'}\left(N_f\right)^b + \sigma_{FL} \tag{1.17}$$

In the case of multiaxial fatigue, the most applied practice is to define an appropriate equivalent stress amplitude and find a relation with the simple uniaxial fatigue test data. Numerous multiaxial fatigue test results of ductile materials can be reasonably predicted by appropriate definition of the equivalent stress. Critical plane criteria (Findley, 1959, McDiarmid, 1991, Fatemi et al., 1988, Jiang, 2000) indicating a relationship between the maximum shear stress and the normal stress on the plane of the maximum shear stress, is also considered as a special form of derivation from stress-based approach as illustrated in (Ellyin, 1997). Stress-based approach is mostly applicable to the high-cycle fatigue regime where the strains are essentially elastic.

1.4.2 Strain-based approach

Strain-based approaches were essentially derived from the stress-based approaches. Coffin (1954) and Manson (1954) independently established the relation between the plastic strain amplitude and the fatigue life:

$$\frac{\Delta\varepsilon^p}{2} = \varepsilon_f^{'}\left(N_f\right)^c \tag{1.18}$$

where ε'_f is the fatigue ductility coefficient and c is the fatigue ductility exponent. By adding the elastic and plastic component of strain amplitude, the total strain amplitude – life curve can be expressed as:

$$\frac{\Delta\varepsilon}{2} = \frac{\Delta\varepsilon^e}{2} + \frac{\Delta\varepsilon^p}{2} = \frac{\sigma'_f}{E}\left(N_f\right)^b + \varepsilon'_f\left(N_f\right)^c \tag{1.19}$$

where the elastic portion was derived from Eq.(1.16) by assuming linear elastic stress-strain relationship. The strain-based approach was essentially introduced for thermal and low-cycle fatigue. The closed-loop testing facility developed in the early sixties enabled precisely strain-controlled cyclic fatigue tests and accelerated the progress in fatigue studies. Similar to the stress-based approach, the extension to multiaxial stress state has been through a suitable definition of the equivalent strain amplitude. The most adopted are the von Mises equivalent strain amplitude and its various derivatives. Critical plane theory in terms of shear and normal strains at the plane with maximum shear strain is also a special case of strain-based approach (Ellyin, 1997).

1.4.3 Energy-based approach

Numerous publications have focused on strain energy during the fatigue process and its relevance to fatigue life (Bairstow, 1910, Behan, 1961a, 1961b, Ellyin et al., 1984, Enomoto, 1955, Martin, 1961, Halford, 1966). Strain energy has demonstrated to be appropriate for characterization of the damage in each cycle of fatigue process (Ellyin, 1997). The nature of fatigue process in both macroscopic and microscopic aspect has been unified in energy approach. Moreover, the stress-strain relationship is also inherently included in energy parameters. The strain energy imposed by the external loads is composed of two parts: recoverable (elastic) and irrecoverable (plastic). The irrecoverable part, represented by the area of hysteresis loop, is dissipated during each cycle in fatigue tests and is related to the damage that occurs in the material. Therefore, assumption was made that the damage occurred is proportional to the dissipated strain energy. However, as the fatigue life approaches the material fatigue limit, the dissipated strain energy becomes a very small value and is therefore difficult to measure accurately. To overcome this problem, the sum of plastic and elastic strain energies can be used. The relation between the total strain energy and the fatigue life can be expressed as:

$$\Delta W = \kappa (N_f)^{\alpha} + \Delta W_0 \tag{1.20}$$

where ΔW is the total strain energy, κ and α are material constants, ΔW_0 is the fatigue limit. Various forms of ΔW have been proposed (Ellyin et al., 1986, Lefebvre et al., 1984, Golos et al., 1987, 1988, Kujawski et al., 1995), among which the one expressed in Eq.(1.21) seems to perform best (Ellyin, 1997).

$$\Delta W = \Delta W^d + f\left(\frac{\sigma_m}{\sigma_a}\right)\Delta W^e \tag{1.21}$$

where $f\left(\frac{\sigma_m}{\sigma_a}\right)$ is the mean stress function (see section 3.3) which accounts for the mean stress effect on fatigue life, ΔW^d and ΔW^e are the plastic strain energy and the elastic strain energy, respectively, as shown in Fig.1.16.

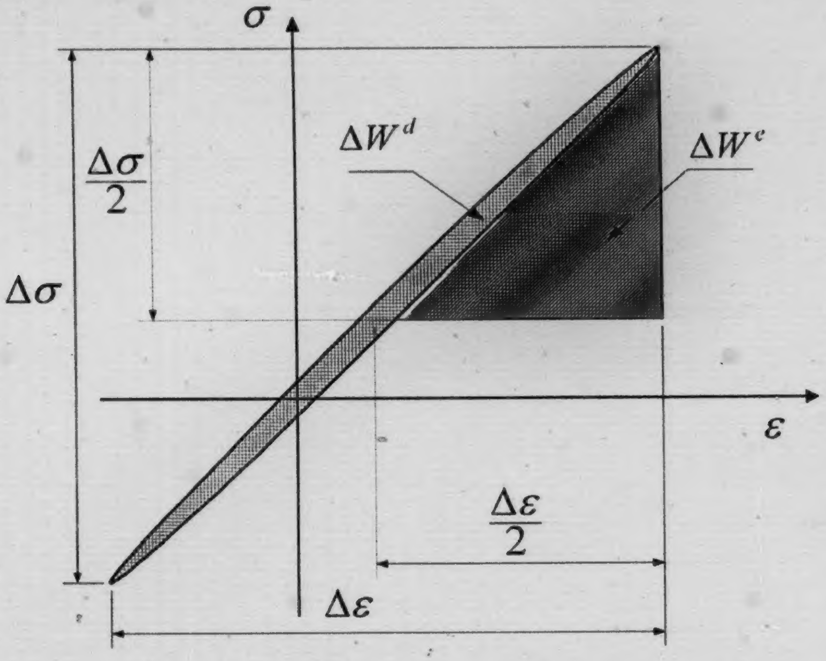
σ
$\frac{\Delta\sigma}{2}$
ΔW^d
ΔW^e
$\Delta\sigma$
ε
$\frac{\Delta\varepsilon}{2}$
$\Delta\varepsilon$

Fig. 1.16 Illustration of the strain energy density components.

1.4.4 Mean stress effect

Engineering components are not usually subjected to symmetric cyclic loading. The presence of a mean stress was found to greatly influence the crack initiation and fatigue life of specimens. Usually a tensile mean stress would result in a reduced fatigue life and therefore the accurate prediction of the fatigue life of the investigated materials under such circumstance becomes of the prime importance. For metals and alloys, various criteria have been proposed to deal with the mean stress effect on fatigue life, such as the well-known Soderberg's diagram (1930), Goodman's diagram (1899), Gerber's diagram (1874), Morrow's diagram (1965) and Smith-Watson-Topper (SWT) parameter (1970).

The Soderberg, Goodman or Morrow's relation was originally introduced to describe the mean stress effect of the material near the fatigue limit and is usually expressed as:

$$\frac{\sigma_a}{\sigma_{-1}} + \frac{\sigma_m}{\sigma_r} = 1 \tag{1.22}$$

where σ_a is the stress amplitude, σ_m is the mean stress, σ_{-1} is the stress amplitude under fully-reversed cyclic loading at fatigue limit, and σ_r is a reference stress. When σ_r is taken as σ_y, σ_u and σ_f' (as in Eq.1.16), which is yield stress, ultimate strength and fatigue strength coefficient, respectively, Eq.(1.22) will result in Soderberg, Goodman or Morrow's equation. The Soderberg, Goodman and Morrow's diagrams are schematically shown in Fig.1.17.

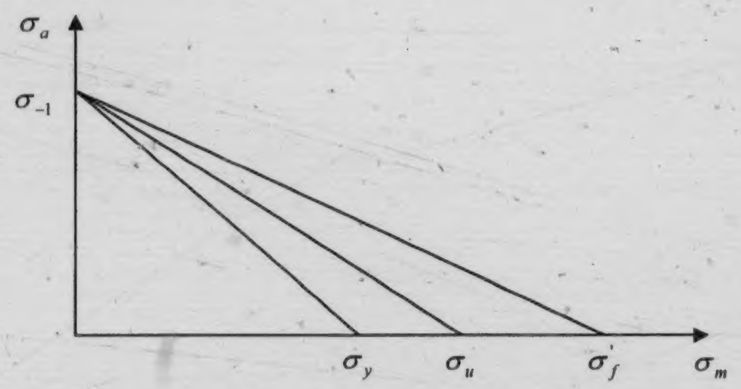

Fig. 1.17 Soderberg, Goodman and Morrow's diagrams

Further investigation of these criteria was conducted by Kujawski et al (1995), where mean stress function in a power law form was proposed and it was demonstrated to be able to unify the above various criteria. An exponential mean stress function was suggested by Kwofie (2001) to relate the mean stress effect to the fatigue strength and life. He also showed that some previous criteria can be seen as particular cases of this mean stress function. The issue of mean stress effect on fatigue life of the epoxy polymer has been studied and will be elaborated in section 3.3.

1.4.5 Ratcheting effect

While materials are subjected to asymmetric cyclic loading, accumulative deformation could occur cycle by cycle, which is called the ratcheting phenomenon. In metals, ratcheting occurs due to the exceeding of yield limit and resulting in plastic deformation in each cycle. Many efforts have been addressed to the ratcheting behavior of metallic materials in both experimental and analytical aspects (Hassan et al., 1994a, 1994b, Xia et al., 1997, Kang et al., 2002, Chen et al., 2003). In addition to cyclic fatigue damage, ratcheting deformation usually leads to extra material damage and could result in reduced fatigue life (Rider et al., 1995, Xia et al., 1996). Therefore, characterization of the ratcheting effect would be quite meaningful to increase the precision of fatigue life prediction. However, due to the coexistence of mean stress effect, determining the ratcheting strain effect was always an extremely challenging task. This might be the reason that there have been only a few publications on this issue (Rider et al., 1995, Xia et al., 1996). However, ratcheting behavior is quite distinct in epoxy polymers under asymmetric cyclic loading (Shen et al., 2004, Xia et al., 2005b). Its effect on fatigue life of the epoxy polymers is of interest for this research. Moreover, due to the viscoelastic nature of the epoxy polymers, the ratcheting mechanism in epoxy polymers could be quite different from metals. The details of the ratcheting behavior and its effect on fatigue life will be illustrated in section 3.4.

1.5 Objectives of current study

The objective of this research is to experimentally investigate the mechanical behavior of an epoxy polymer under various uniaxial and multiaxial cyclic fatigue loading conditions and study the evolutions of its properties and damage mechanisms during the fatigue process. Based on experimental observations, appropriate multiaxial fatigue theory is to be developed and thus an effective design tool for prediction of fatigue lives of the epoxy polymer material under various practical loading conditions will be provided. The above general objective can be further detailed into following sub-objectives or procedures:

1. Since traditional extensometers or strain gauges are not suitable for use in cyclic fatigue tests for soft epoxy polymer materials, a fatigue test system based on the non-contact strain measurement technique needs to be established.

2. Uniaxial fatigue tests are to be performed first to obtain the basic S-N curve. The evolution of mechanical properties of the epoxy polymer during fatigue process will then be analyzed based on the stress-strain data. And the fatigue mechanism of the epoxy polymer can be investigated.

3. Loading conditions in practical applications can be complicated. To investigate the effect of various loading conditions on fatigue life of the epoxy polymer, mean stress and ratcheting strain will be introduced in the fatigue tests. Then the mean stress/strain effect, ratcheting strain effect on fatigue life of the epoxy polymer can be identified. Appropriate damage parameters will then be proposed and the fatigue life prediction models will be established.

4. To extend the applicability of the fatigue life prediction models, a series of multiaxial fatigue tests need to be conducted to investigate the effect of multiaxial loading conditions on fatigue behavior of the epoxy polymer. The evolution of mechanical properties of the epoxy polymer during multiaxial fatigue process will be analyzed. Appropriate multiaxial fatigue life prediction models can be established for the epoxy polymer material.

Bibliography

1. Al-Assaf Y, El Kadi, H. Fatigue life prediction of composite materials using polynomial classifiers and recurrent neural networks. Composite Structures 2007; 77(4):561-569.
2. Anderson, TL. Fracture Mechanics: Fundamentals and Applications, CRC Press, 1991.
3. Bairstow L. The elastic limits of iron and steel under variations of stress. Phil. Trans. R. Soc. London A 1910; 210:35-55.
4. Basquin OH. The exponential law of endurance tests. Proc ASTM 1910; 10(II):625-30.
5. Behan PP. Axial load and strain-cycling fatigue of copper at low endurance. J. Inst. Metals 1961a; 89:328-38.
6. Behan PP, Ford H. Low endurance fatigue of a mild steel and an aluminum alloy. J. Mech. Engng. Sci. 1961b; 3:119-32.
7. Brown RP, Physical Testing of Rubber, 2nd ed. Elsevier Applied Science Publishers, London and New York, 1986.
8. Chen X, Hui S. Ratcheting behavior of PTFE under cyclic compression. Polymer Testing 2005; 24(7):829-33.
9. Chen X, Kim K. Modeling of ratcheting behavior under multiaxial cyclic loading. Acta Mechanica 2003; 163(1-2):9-23.

10. Clark TR, Hertzberg RW, Mohammadi N. Fatigue mechanisms in poly(methyl methacrylate) at threshold: effects of molecular weight and mean stress. J Mat Sci 1993; 28(19):5161-8.
11. Coffin LF. A study of the effects of cyclic thermal stresses on a ductile metal. Trans. ASME, 1954; 76:931-50.
12. Ellyin F, Fatigue Damage, Crack Growth, and Life Prediction. Chapman & Hall, London, UK, 1997.
13. Ellyin F, Kujawski D. Plastic strain energy in fatigue failure. J. Pressure Vessel Technol. Trans. ASME 1984; 106:342-7.
14. Ellyin F, Kujawski D. An energy-based fatigue failure criterion. Microstructure and Mechanical Behavior of Materials, Vol II, EMAS, West Midlands, UK 1986; 541-600.
15. Enomoto, N. On fatigue tests under progressive stress. Proc. ASTM 1955; 55:903-13.
16. Fatemi A, Socie DF. A Critical plane approach to multiaxial fatigue damage including out of phase loading. Fatigue Fract Eng Mater Struct 1988; 11:149-65.
17. Findley WN. A theory for the effect of mean stress on fatigue of metals under combined torsion and axial load or bending. J Engng Ind Trans ASME 1959; 81:301-6.
18. Gamstedt EK, Ostlund S. Fatigue Propagation of Fibre-Bridged Cracks in Unidirectional Polymer-Matrix Composites. Applied Composite Materials 2001; 8(6):385-10.

19. Gerber H. Bestimmung der zulassigen Spannungen in eisen Constructionen. Z Bayer Arch Ing Ver 1874; 6:101-10.
20. Gilchrist MD, Kinloch AJ, Matthews FL. Mechanical performance of carbon-fibre- and glass-fibre-reinforced epoxy I-beams: III. Fatigue performance. Composites Science and Technology 1999; 59(2):179-200.
21. Golos K, Ellyin F. Generalization of cumulative damage criterion to multilevel cyclic loading. Theor Appl Fract Mech 1987; 7:169-76.
22. Golos K, Ellyin F. A total strain energy density theory for cumulative damage. J Pressure Vessal Technol, Trans, 1988; 110:36-41.
23. Goodman J. Mechanics applied to engineering. London: Longmans, Green and Company, 1899.
24. Halford GR. The energy required for fatigue. J. Mater. 1966; 1:3-18
25. Hassan T, Kyriakides S. Ratcheting of cyclically hardening and softening materials: I. Uniaxial behavior. Int J Plast 1994a; 10(2):149-184.
26. Hassan T, Kyriakides S. Ratcheting of cyclically hardening and softening materials: I. Multiaxial behavior. Int J Plast 1994b; 10(2):185-212.
27. Hu Y. Multiaxial Behavior and Viscoelastic Constitutive Modeling of Epoxy Polymers. PhD thesis, Department of Mechanical Engineering, University of Alberta, 2002.
28. Hu Y, Xia Z, Ellyin F. Deformation Behavior of an Epoxy Resin Subject to Multiaxial Loadings. Part I: Experimental Investigations. Polymer Engineering and

Science 2003; 43(3):721-33.

29. Ives GC, Mead JA, Riley MM, Handbook of Plastics Test Methods, CRC Press, Cleveland, Ohio, 1971.
30. Jiang Y. A fatigue criterion for general multiaxial loading. Fatigue Fract Eng Mater Struct 2000; 23:19-32.
31. Kanchanomai C, Yamamoto S, Miyashita Y, Mutoh Y, McEvily AJ. Low cycle fatigue test for solders using non-contact digital image measurement system. International Journal of Fatigue 2002; 24(1):57-67.
32. Kang G, Gao Q, Yang X. A visco-plastic constitutive model incorporated with cyclic hardening for uniaxial/multiaxial ratcheting of SS304 stainless steel at room temperature. Mechanics of Materials 2002; 34(9):521-31.
33. Kausch HH, Polymer Fracture 2nd ed., Springer-Verlag, Berlin, New York, 1987.
34. Kawagoe M, Nomiya M, Qiu J, Morita M, Mizuno W. Fatigue behaviour of injection-moulded polymer blends of polypropylene and liquid crystalline polyester. Polymer 1997; 38(1):113-8.
35. Kaynak C, Mat O. Uniaxial fatigue behavior of filament-wound glass-fiber/epoxy composite tubes. Composites Science and Technology 2001; 61(13):1833-40.
36. Knauss WG, Emri IJ. Non-linear Viscoelasticity Based on Free Volume Consideration. Computers & Structures 1981; 13:123-128.
37. Knauss WG, Emri IJ. Volume Change and the Nonlinearly Thermo-Viscoelastic Constitution of Polymers. Polymer Science and Engineering 1987; 27(1):86-100.

38. Krishnaswamy P, Tuttle ME, Emery AF. Finite Element Modeling of the Time-Dependent Behavior of Nonlinear Ductile Polymers. Polymer Engineering and Science 1992; 32(16):1086-96.

39. Kujawski D, Ellyin F. A unified approach to mean stress effect on fatigue threshold conditions. Int J Fatigue 1995;17(2):101-6.

40. Kwofie S. An exponential stress function for predicting fatigue strength and life due to mean stresses. Int J Fatigue 2001;23(9):829-36.

41. Kwon HJ, Jar P.-Y.B., Xia Z. Characterization of Bi-axial fatigue resistance of polymer plates. Journal of Materials Science 2005; 40(4):965-72.

42. Lai J, Bakker A. 3-D Schapery Representation for Non-linear Visco-elasticity and Finite Element Implementation. Computational Mechanics 1996; 18:182-91.

43. Lefebvre D, Ellyin F. Cyclic response and inelastic strain energy in low-cycle fatigue. Int J Fatigue 1984; 6:9-15

44. Liang T, Tokunaga K, Yamashita A, Takahara A, Kajiyama T. Relationships between nonlinear dynamic viscoelasticity and fatigue behaviors of glassy polymer under various fatigue test conditions. Polymer Bulletin 1996; 36(4):477-82.

45. Lifshitz JM. Compressive fatigue and static properties of a unidirectional graphite epoxy composite. Journal of Composite Technology & Research 1988; 10(3):100-6.

46. Lorenzo L, Hahn HT. Effect of Ductility on the Fatigue Behavior of Epoxy Resins. Polymer Engineering and Science 1986; 26(4):274-84.

47. Lou YC, Schapery RA. Viscoelastic Characterization of a Nonlinear Fiber-reinforced Plastic. Journal of Composite Materials 1971; 5:208-34.

48. Manson SS. Behavior of materials under conditions of thermal stress. NACA 1954 TN-2933, National Advisory Committee for Aeronautic.

49. Martin DE. An energy criterion for low-cycle fatigue. J. Basic Engng. Trans. ASME 1961; 83:565-71.

50. McDiarmid DL. A general criterion for high cycle multiaxial fatigue failure. Fatigue Fract Engng Mater Struct 1991; 14(4):429-53.

51. Morrow J. In 'Internal Friction, Damping, and Cyclic Plasticity', ASTM STP 378, American Society for Testing and Materials, Philadelphia, 1965;45-87.

52. Nagasawa M, Kinuhata H, Koizuka H, Miyamoto K, Tanaka T, Kishimoto H, Koike H. Mechanical fatigue of epoxy resin. Journal of Materials Science 1995; 30(5):1266-72.

53. Osswald TA, Menges G. Materials Science of Polymers for Engineers. Hanser Gardner Publications, Cincinnati, USA, 2003

54. Peters WH, Ranson WF. Digital imaging techniques in experimental stress analysis. Optical Engineering 1982; 21(3):427-31.

55. Qi D, Cheng G. Fatiaue behavior of filament-wound glass fiber reinforced epoxy composite tension/torsion biaxial tubes under loading. Polymer Composites 2007; 28(1): 116-23.

56. Rider RJ, Harvey SJ, Chandler HD. Fatigue and ratcheting interactions. Int J Fatigue

1995; 17(7):507-11.

57. Rudin A. The elements of polymer science and engineering: an introductory text and reference for engineers and chemists, 2nd Ed. Academic Press, San Diego, 1999.
58. Sauer JA, McMaster AD, Morrow DR. Fatigue behavior of polystyrene and effect of mean stress. J Macromol Sci Phys 1976; B12(4):535-62.
59. Sauer JA, Richardson GC. Fatigue of polymers. International Journal of Fracture 1980; 16(6):499-532.
60. Schapery RA. Further Development of a Thermodynamic Constitutive Theory: Stress Formulation. AA&ES Report No. 69-2, 1969a, Purdue University.
61. Schapery RA. On the Characterization of Nonlinear Viscoelastic Materials. Polymer Engineering and Science 1969b; 9:295-310.
62. Shen X, Xia Z, Ellyin F. Cyclic Deformation Behavior of an Epoxy Polymer. Part I: Experimental Investigation. Polymer Engineering and Science 2004; 44(12):2240-6.
63. Smith KN, Watson P, Topper TH. Stress-strain function for the fatigue of metals. J Mater, JMLSA 1970; 5(4):767-778.
64. Soderberg CR, Sweden V. Factor of Safety and Working Stress. ASME Transaction, AER-IS, 1930; 52(2):13-28.
65. Takemori MT. Polymer Fatigue. Annual Review of Materials Science 1984; 14:171-204.
66. Trotignon JP, Verdu J, Morel E. Roughness effects on the fatigue behavior of an epoxy matrix. Journal of Materials Science letters 1991; 10(14):844-6.

67. Wang TJ, Zong Z, Notomi M, Kishimoto K. Experimental investigation of the low cycle fatigue crack propagation in PC/ABS polymer blends ACTA MECHANICA SOLIDA SINICA 2001; 14(4):344-8.

68. Wöhler A. Tests to determine the forces acting on railway carriage axles and the capacity of resistance of the axles. Engineering 1871; 11.

69. Yamaguchi I. A Laser-Speckle Strain-Gauge. Journal of Physics E: Scientific Instruments 1981; 14(11):1270-3.

70. Xia Z, Ellyin F. A constitutive model with capability to simulate complex multiaxial ratcheting behavior of materials. Int J Plast 1997; 13(1-2):127-42.

71. Xia Z, Hu Y, Ellyin F. Deformation Behavior of an Epoxy Resin Subject to Multiaxial Loadings. Part II: Constitutive Modeling and Prediction. Polymer Engineering and Science 2003; 43(3):734-48.

72. Xia X, Kujawski D, Ellyin F. Effect of mean stress and ratcheting strain effect on fatigue life of steel. Int J Fatigue 1996; 18(5):335-41.

73. Xia Z, Shen X, Ellyin F. Cyclic Deformation Behavior of an Epoxy Polymer. Part II: Prediction of Viscoelastic Constitutive Models. Polymer Engineering and Science 2005a; 45(1):103-13.

74. Xia Z, Shen X, Ellyin F. Biaxial Cyclic Deformation of an Epoxy Resin: Experiments and Constitutive Modeling. Journal of Materials Science 2005b; 40(3):643-54.

Chapter 2

Fatigue Testing System

2.1 Introduction

Polymers are viscoelastic or viscoplastic materials with distinct time-dependent deformation behaviors as described in Chapter 1, such as strain recovery, stress relaxation, accumulation of ratcheting strain (cyclic creep) in stress-controlled cyclic tests with mean stress, stress relaxation in strain-controlled cyclic tests with mean strain, etc. It can be foreseen that the control modes, the loading rates and the loading paths will have significant effects on the fatigue behavior of the polymer materials. Therefore, acquisition of strain and stress data during the entire fatigue test process is important for understanding fatigue mechanisms and development of theoretical models. Strain gauges and extensometers have served as conventional strain measurement tools in most mechanical experiments. Their use in cyclic/fatigue tests could meet some difficulties. For example, strain gauges could not be used if fatigue life of the gauges was shorter than that of the material tested. For relatively soft materials such as polymers, the knives of the extensometer could cause local damage even with protective film and thus the obtained fatigue life could be much shorter than that of a specimen with smooth surface. There have been a large number of publications on fatigue tests of polymers, e.g. see refs. (Lorenzo et al., 1986, Nagasawa et al., 1995, Sauer et al., 1980, Takemori, 1984, Trotignon et al., 1991), among others. Fatigue tests can be carried out under load (stress)-controlled or deformation (strain)-controlled modes. For rubbers and plastics the latter type of fatigue tests was usually carried out by controlling a certain global deformation parameter (grip displacement, rotational angle, etc.) (Brown, 1986, Ives et al., 1971). In most cases, the local strain values were not directly measured or carefully monitored during the entire test procedure. Availability of an effective non-contact strain measurement method becomes increasingly necessary to gain more insight into the fatigue behavior of polymer materials.

Kanchanomai, C. et al. (2002) pioneered use of a digital image system in strain-range-controlled uniaxial fatigue tests of solder materials. The precision of their measurement suffered from the ambiguity of the mark edges. Therefore, as claimed in the reference, the minimum detectable strain was only 0.08%. Furthermore, this method has not been applied to multiaxial fatigue test.

Several optical deformation measurement techniques, such as electronic speckle pattern interferometry (ESPI), moiré interferometry and digital image correlation method (DICM), have appeared with well-developed computer technology. They are able to perform non-contact, high precision and whole-field displacement measurement. Traditional ESPI and moiré interferometry are based on fringe processing. For example, in ESPI the difference between two adjacent fringes represents $\lambda/2$ for the out-of-plane deformation and $\lambda/(2\sin\theta)$ for the in-plane deformation, respectively, where λ is the wave length of the laser and θ is the angle between the optical axis and the object illumination beam (Erf, 1978, Sirohi, 1993). Therefore, the measurement range is limited by the degree that the fringes can be clearly distinguished. Temporal Speckle Pattern Interferometry (TSPI), proposed by Joenathan et al. (1998) and Li et al. (2001a, 2001b), is able to perform large deformation measurement. The displacement of each pixel in the image was retrieved by phase analysis in the temporal domain instead of fringe analysis in the spatial domain. Thus, most limitations caused by fringe analysis can be eliminated. This technique has been successfully applied in low frequency harmonic vibration analysis (Li et al., 2002) and study of material mechanical behavior (Tao et al., 2004). However, high requirement for vibration isolation and relatively large capital investment has limited the applications of either ESPI or TSPI.

Digital Image Correlation Method (DICM) introduced by Peters et al. (1982) and Yamaguchi (1981) has been widely utilized in experimental mechanics in recent years. Not only the laser speckle pattern but also the natural texture or artificial pattern on the surface of the object can be used to determine the displacement of the object. Two digitalized images, taken before and after displacement, are matched by correlation operation. Then displacement and displacement derivatives can be retrieved. Furthermore, whole-field deformation can be obtained by analyzing each subset in the image. Many applications have demonstrated the robust applicability of this technique. For example, McNeill et al. (1997) developed a system for measuring surface profiles of objects using DICM. Luo et al. (1993) extended this technique into three-dimensional displacements measurement. Han et al. (1994) employed this method in the crack-tip deformation analysis. Rae et al. (2004) applied digital image cross-correlation in the analysis of whole-field deformation of a polymer bonded explosive. However, the whole-field DICM is quite time-consuming. The displacements or strains need to be retrieved in the post-processing stage. To the best of our knowledge, the DICM method has not been applied in real-time displacement or strain measurements.

In this Chapter, the DICM is introduced to perform real-time non-contact strain measurement for multiaxial cyclic/fatigue tests of the epoxy polymer. The strain data can be fed back to the control system of the test machine to perform a strain-range-controlled fatigue test. Some preliminary test results, including various types of multiaxial cyclic/fatigue tests, are presented to demonstrate the universality and reliability of this new system.

2.2 Specimens and testing system

2.2.1 Specimens and fabrication

The epoxy polymer adopted for investigation is an EPON 826/EPI-CURE Curing Agent 9551, a bisphenol-A epoxy resin and a non-MDA (methylene dianiline) polyamine system. It provides a unique combination of high elongation, high toughness and thermal resistance. This system is ideal as matrix phase of high performance composite parts designed for processing by filament winding or resin transfer molding, such as pressure vessels, where high fatigue and microcracking resistance is required. Some physical and mechanical parameters of this epoxy polymer are listed in Table 2.1.

Table 2.1. Physical and mechanical parameters of EPON 826/EPI-CURE Curing Agent 9551 (Data were adopted from specification manual from Resolution Performance® company and our own test results)

Properties	**Values**
Glass Transition Temperature	110 °C
Thermal expansion Coefficient	56 μ/m °C
Water up-take (14 days at 140 °F)	1.8%
Tensile modulus (21 °C, 10 MPa/s)	2900 MPa
Ultimate strength (21 °C, 10 MPa/s)	87 MPa
Poisson's ratio	0.42

The resin and the curing agent were mixed in the ratio of 100:36 (weight) and cast into steel tubes. The castings were cured in the oven for 2 hours at 50°C and then 2.5 hours at 120°C. The specimens were cooled to room temperature in the oven. Two types of specimens, solid specimen and thin-walled tubular specimen, shown in Fig.2.1 with drawings and photo, were machined by a CNC lathe. The surface of specimen was further polished by fine abrasive paper and alumina powder (size of 5 microns) to reach an average surface roughness $R_a \leq 0.3\mu m$ with the maximum surface roughness $R_{\max} \leq 2\mu m$. At this level, surface roughness effect could be negligible according to Trotignon et al.'s work (1991). To minimize the possible aging effect, each specimen was heat-treated at 80°C for 12 hours and then cooled to room temperature in the oven one day before the test. It was found that more stable and repeatable test data could be obtained by such "thermal recovery treatment" on the epoxy polymer material (Shen et al., 2004).

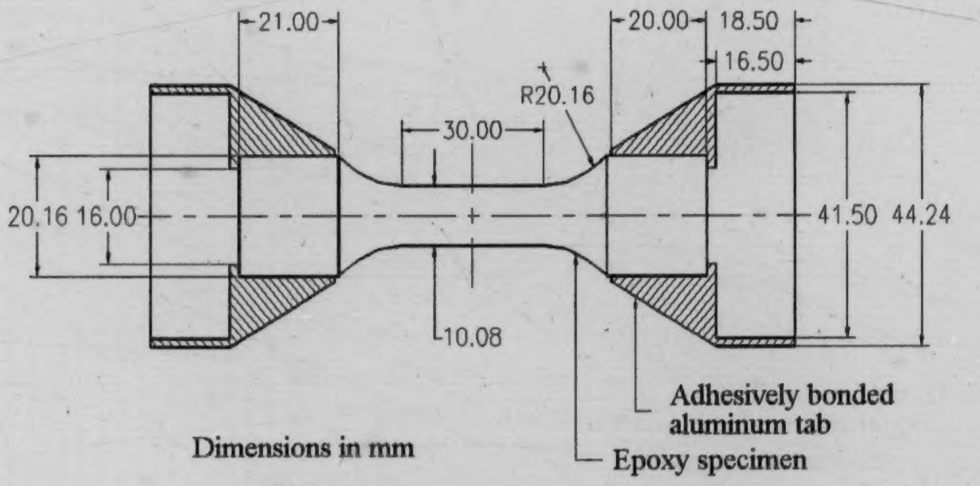
21.00
20.00
18.50
16.50
R20.16
30.00
20.16
16.00
41.50
44.24
10.08
Adhesively bonded aluminum tab
Epoxy specimen
Dimensions in mm

(a) Solid specimen (for uniaxial fatigue test)

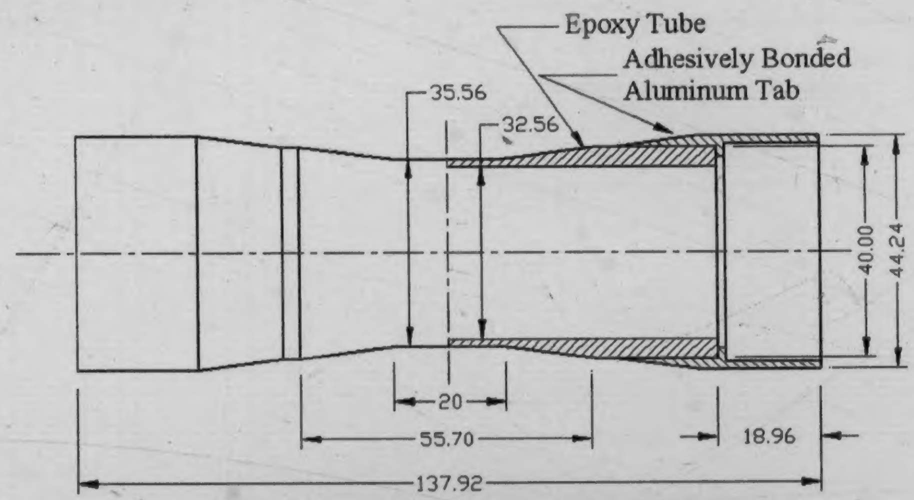
Epoxy Tube
Adhesively Bonded
Aluminum Tab
35.56
32.56
40.00
44.24
20
55.70
18.96
137.92

(b) Tubular specimen (for multiaxial fatigue test)

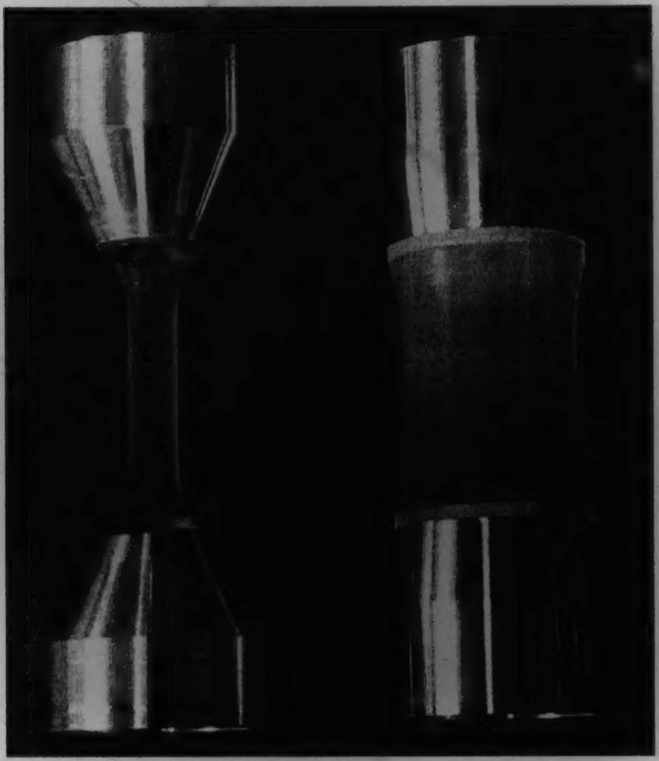

(c) Photo of solid and tubular specimens with end-tabs

Fig. 2.1 Drawings and photo of the specimens

2.2.2 Testing systems

All the uniaxial tests of solid specimens were performed by a modified MTS system as shown in Fig.2.2(a), details of which have been described in (Ellyin, 1997). And all the multiaxial tests of tubular specimen were performed by an in-house-made servo-hydraulic triaxial fatigue test machine (Ellyin et al., 1997) shown in Fig.2.2(b), which is capable of applying axial load, shear load and internal pressure and external pressure simultaneously.

(a) A modified MTS system for biaxial fatigue test (axial, internal and external pressure)

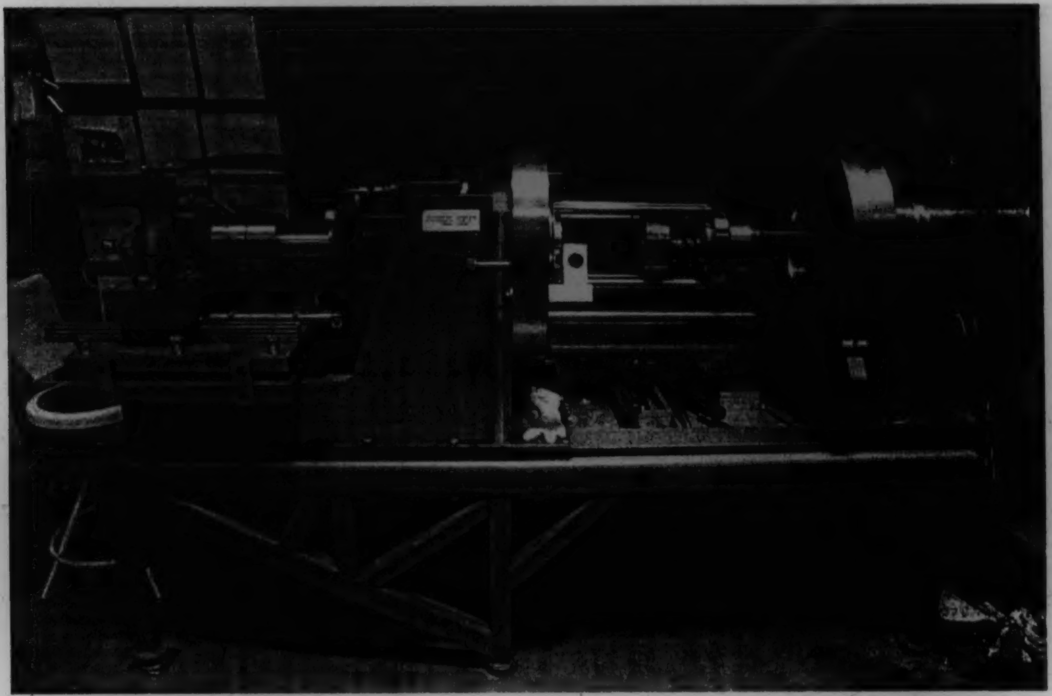

(b) A triaxial fatigue test system (axial, torsional, internal and external pressure)

Fig. 2.2 Fatigue testing machines

The whole test system configuration is schematically shown in Fig.2.3. A Matrox Meteor-II/Multi-Channel frame grabber was installed in a personal computer and connected with a Sony XC-HR70 Monochrome CCD camera (8 bit 1024×768) which was dedicated to image capturing. A National Instrument data acquisition card was installed in the computer for performing the functions of data acquisition and system control. During the test, the camera captures the images of the surface of the specimen continuously. The strain is then retrieved from these images in real-time and the stress is also synchronously recorded.

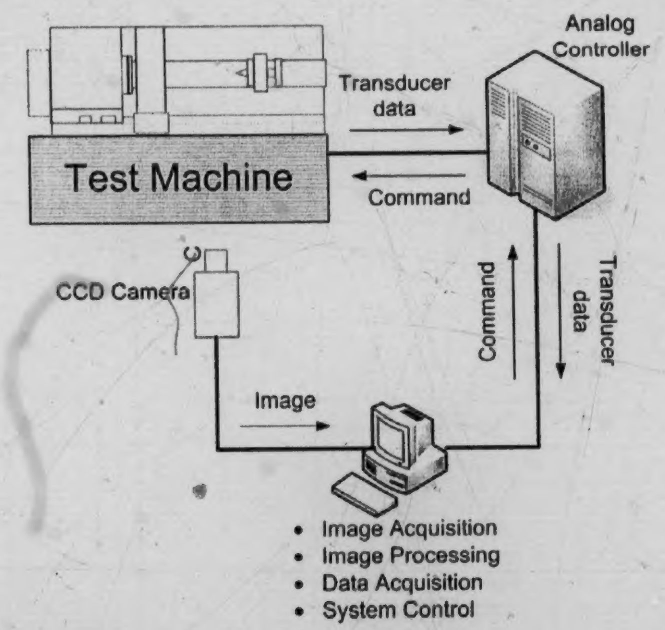
Analog Controller
Transducer data
Test Machine
Command
CCD Camera
Command
Transducer data
Image
Image Acquisition
Image Processing
Data Acquisition
System Control

Fig. 2.3 Configuration of the non-contact strain measurement and control system

2.3 Non-contact real-time strain measurement system

2.3.1 Principle of Digital Image Correlation Method (DICM)

Images, taken before and after deformation of an object, represent the positions of the object at these two moments of time. To retrieve the in-plane displacements at a certain point of interest on the object, a small subset surrounding this point in the reference image (taken before displacement) is selected to match the similar subset area in the target image (taken after displacement). This procedure is called digital image correlation. To quantify the degree of correlation, various correlation coefficients have been introduced, such as cross correlation coefficient (Chu et al., 1985) and its various derivatives (Bruck et al., 1989). Digital image correlation procedures are always time-consuming because considerable calculations should be carried out to obtain the displacement value through searching either maximum or minimum value of the correlation coefficient. In order to perform real-time image processing, a relatively simple correlation coefficient is preferred. A normalized least square correlation coefficient is defined as:

$$C = \frac{\sum_{i=1}^{m}\sum_{j=1}^{n}\left[f(x_i, y_j) - g(x_i^*, y_j^*)\right]^2}{\sum_{i=1}^{m}\sum_{j=1}^{n} f(x_i, y_j)} \tag{2.1}$$

where

$$\begin{aligned} x_i^* &= x_i + u + \frac{\partial u}{\partial x}dx + \frac{\partial u}{\partial y}dy \\ y_j^* &= y_j + \mathrm{v} + \frac{\partial \mathrm{v}}{\partial x}dx + \frac{\partial \mathrm{v}}{\partial y}dy \end{aligned} \tag{2.2}$$

u and v are in-plane displacements of the subset center along x and y directions. $\frac{\partial u}{\partial x}$, $\frac{\partial u}{\partial y}$, $\frac{\partial \mathrm{v}}{\partial x}$ and $\frac{\partial \mathrm{v}}{\partial y}$ are displacement gradients. $f(x_i, y_j)$ and $g(x_i^*, y_j^*)$ are gray values of each pixel in the reference and target images, respectively. All pixels in an m×n pixels subset are taken into the calculation. A minimum value of the correlation coefficient C, which represents difference between these two subsets, will be achieved if the real displacements and displacement gradients, u, v, $\frac{\partial u}{\partial x}$, $\frac{\partial u}{\partial y}$, $\frac{\partial v}{\partial x}$ and $\frac{\partial v}{\partial y}$, are found. To further simplify the calculation, in our application, the correlation coefficient was modified as:

$$C=\sum_{i=1}^{m}\sum_{j=1}^{n}\left|f\left(x_i,y_j\right)-g\left(x_i^*,y_j^*\right)\right| \tag{2.3}$$

Two small marks spaced a certain distance apart along the axial direction were made on the cylindrical surface of the specimens (see Fig.2.1(c)). The mark points areas are selected as the subsets and the sizes of them are around 12×12 pixels (It is worth to be mentioned that the optimized size of the subset needs further investigation. The size of 12 × 12 pixels was found to be a good compromise between the precision and time-consumption in our practical exercises.). Only the displacement of the subset center is concerned and, due to the small size of the subset and the uniformity of the strain field in the gauge area, the values of third and fourth items in the right side of Eq.(2.2) are much smaller in comparison to the values of the second item. Therefore, neglecting derivative items in Eq.(2.2) has little effect on the calculation of displacements of the subset center, i.e. Eq.(2.2) can be approximated as,

$$\begin{aligned} x_i^* &= x_i + u \\ y_j^* &= y_j + \mathrm{v} \end{aligned} \tag{2.4}$$

This will significantly simplify the calculation procedure and increase the search speed.

2.3.2 Fast searching algorithm in DICM

To perform real-time processing, an optimized searching strategy must be utilized. A two step searching strategy, which is similar to the so called coarse-fine search method (Chu et al., 1985), is employed in our image analysis system. In the first step, searching is operated at pixel level. The searching range was predefined by an estimation of the movement range of the subsets. Through the first step, displacements of reference subsets were acquired at integer pixel level. In the second step, searching operates at sub-pixel level. The gray value at sub-pixel position can be obtained by bilinear interpolation. In the second step, a 2-D quadratic surface fitting of the correlation coefficients of adjacent 9 pixels was conducted firstly. Then the sub-pixel displacements were estimated by locating the coordinates of the minimum correlation coefficient. Afterwards, the sub-pixel displacement was further refined by a minimum-value-oriented searching method. With this method, searching is along the minimum coefficient oriented direction instead of calculating coefficient C of each position within the target subset area. Then, only the points along the searching path are required to be calculated. The searching speed can be increased more than 50 times by using this optimized searching method. Fig.2.4 is the flow chart of the searching procedure. Fig.2.5 displays a typical distribution of the correlation coefficient from the experiment data at sub-pixel level. A very smooth surface and a unique minimum value of such a distribution is the prerequisite for the minimum-value-oriented searching method. Minimum displacement of 0.02 pixels can be detected in our system (The subdivision of the interpolation can be adjusted arbitrarily. However, no further improvement in precision was achieved by reducing the subdivision size of less than 0.02 pixels.).

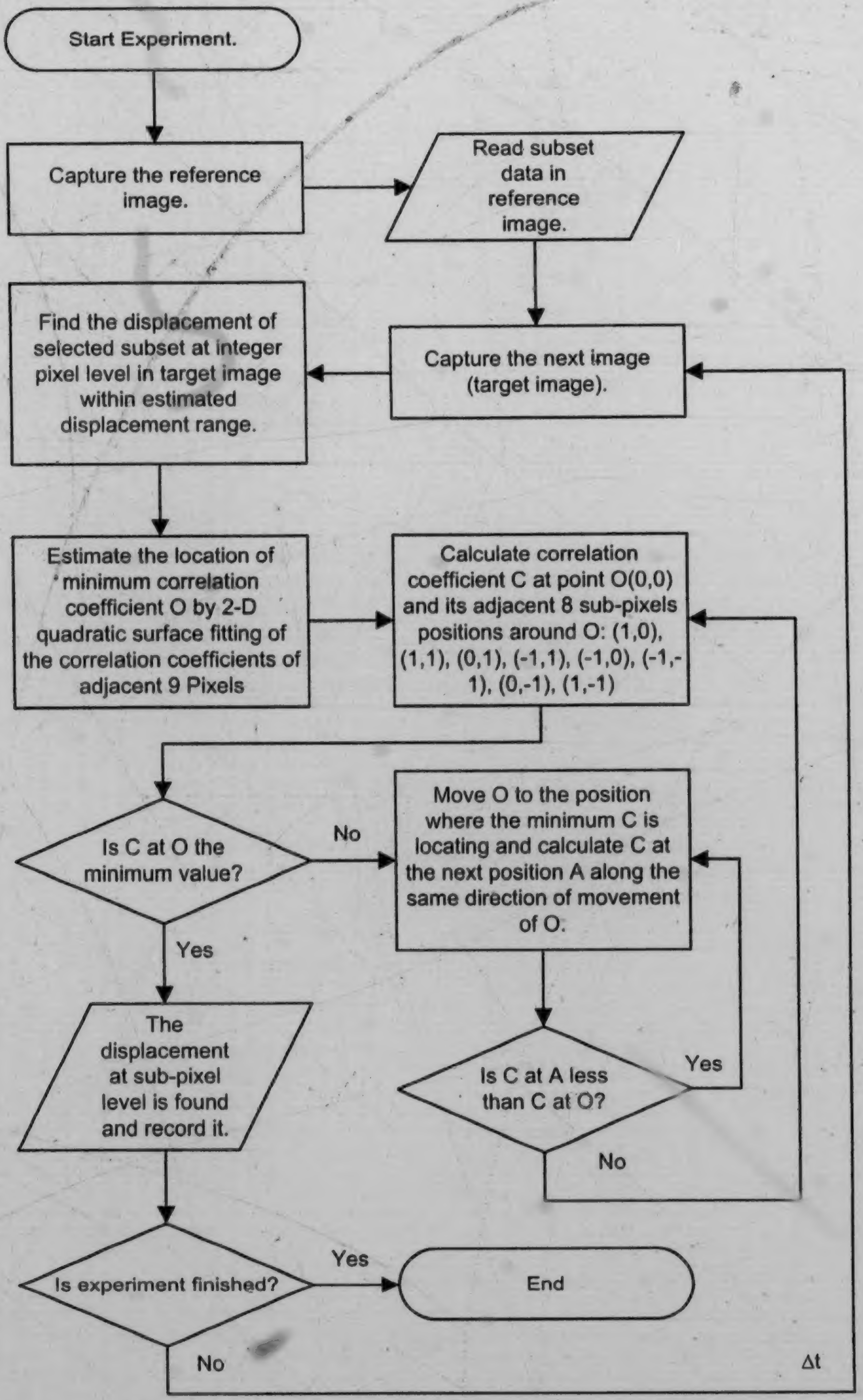
Start Experiment.
Capture the reference image.
Read subset data in reference image.
Find the displacement of selected subset at integer pixel level in target image within estimated displacement range.
Capture the next image (target image).
Estimate the location of minimum correlation coefficient O by 2-D quadratic surface fitting of the correlation coefficients of adjacent 9 Pixels
Calculate correlation coefficient C at point O(0,0) and its adjacent 8 sub-pixels positions around O: (1,0), (1,1), (0,1), (-1,1), (-1,0), (-1,-1), (0,-1), (1,-1)
Is C at O the minimum value?
No
Move O to the position where the minimum C is locating and calculate C at the next position A along the same direction of movement of O.
Yes
The displacement at sub-pixel level is found and record it.
Is C at A less than C at O?
Yes
No
Is experiment finished?
Yes
End
No
Δt

Fig. 2.4 Flow chart of searching procedure of DICM in real-time strain measurement

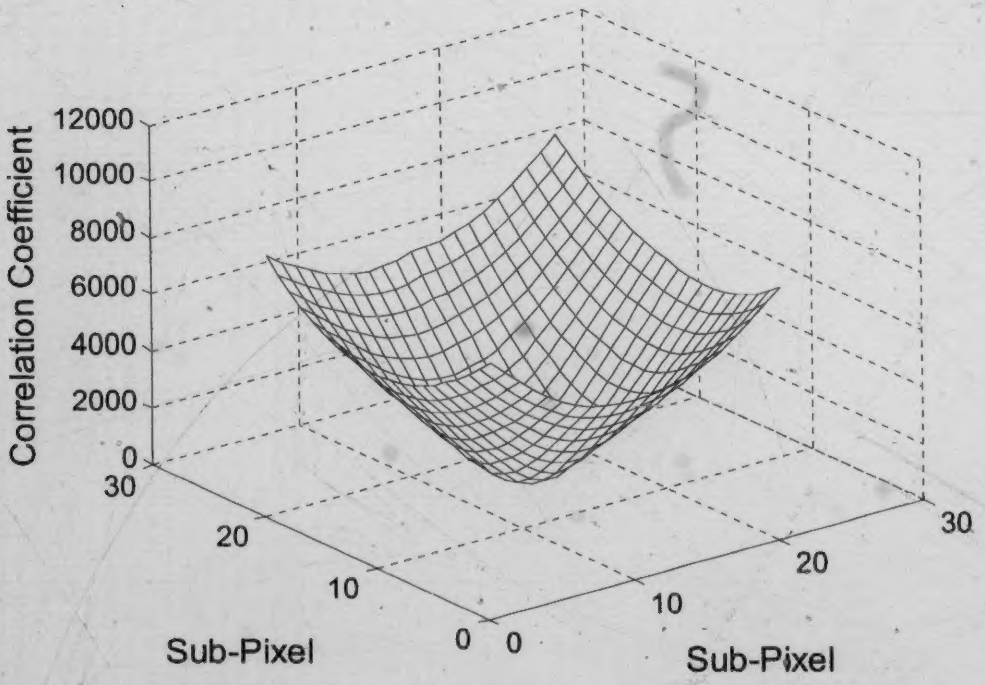

Fig. 2.5 Correlation coefficient distribution in DICM at sub-pixel level.

2.3.3 Strain derivations

Once the displacements of the two mark points are obtained, strains in the gauge area can be derived. Fig.2.6 (a) and (b) show the model for strain calculation. The cross section and side view of the test gauge of the specimen are displayed at the left and right sides of Fig.2.6(a), respectively. Circles 1 and 2 represent initial positions of the two marks before deformation and circles 1' and 2' represent their positions after deformation. R is the radius of the outer surface of the cross section of the specimen and L is the initial axial distance between these two marks under zero loading.

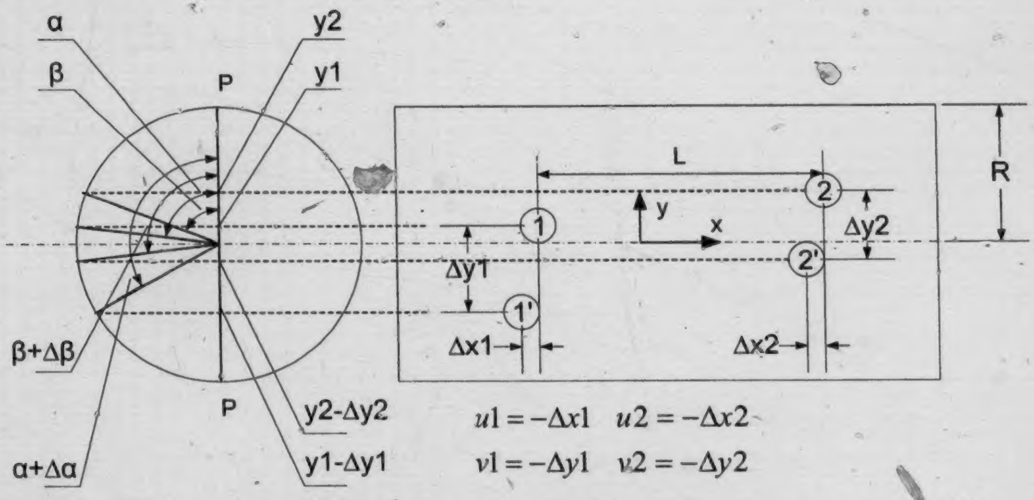
α
β
P
y2
y1
L
R
y
x
1
2
2'
1'
Δy1
Δy2
Δx1
Δx2
β+Δβ
α+Δα
P
y2-Δy2
y1-Δy1
$u1 = -\Delta x1 \quad u2 = -\Delta x2$
$v1 = -\Delta y1 \quad v2 = -\Delta y2$

(a) Cross section and side view of the specimen

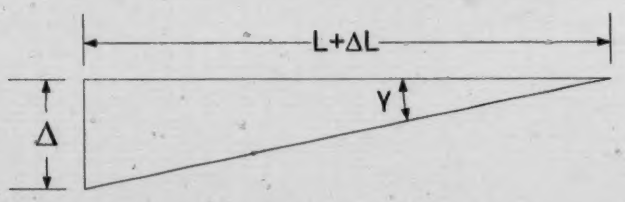

(b) Sketch of shear strain calculation

Fig. 2.6 A schematic illustration for strain calculation

In the case of a biaxial loading condition, the mark points will move along both x and y directions as shown in Fig.2.6(a). Since the specimen undergoes a uniform deformation, difference of initial positions of the mark points will make no difference in the strain calculation. Then the axial strain can be expressed as:

$$\varepsilon_x = \frac{\Delta L}{L} = \frac{u2 - u1}{L} = \frac{\Delta x_1 - \Delta x_2}{L} \tag{2.5}$$

The shear strain can be calculated by:

$$\gamma = \tan^{-1}\frac{\Delta}{L+\Delta L} \tag{2.6}$$

As shown in Fig.2.6(b), Δ is the relative circumferential displacement of the outer surface between two cross sections where marks 1 and 2 are located. Assuming initial angles, α and β, of these two marks according to the projection plane PP are:

$$\begin{aligned} \alpha &= \cos^{-1}\left(\frac{y1}{R}\right) \\ \beta &= \cos^{-1}\left(\frac{y2}{R}\right) \end{aligned} \tag{2.7}$$

After rotation, the angles change to:

$$\begin{aligned} \alpha + \Delta\alpha &= \cos^{-1}\left(\frac{y1+v1}{R}\right) = \cos^{-1}\left(\frac{y1-\Delta y1}{R}\right) \\ \beta + \Delta\beta &= \cos^{-1}\left(\frac{y2+v2}{R}\right) = \cos^{-1}\left(\frac{y2-\Delta y2}{R}\right) \end{aligned} \tag{2.8}$$

and the relative rotation angle between these two cross sections is:

$$\Delta\phi = \Delta\alpha - \Delta\beta \tag{2.9}$$

Thus, the relative circumferential displacement is:

$$\Delta = \Delta\phi \cdot R \tag{2.10}$$

Substitute Eq.(2.10) into Eq.(2.6), the shear strain can be obtained.

The precision of ΔL or Δ is 0.02 pixel, according to Eq.(2.5) and (2.6), the precision of the strains depends on the distance between two marks. For $L = 1000$ pixels (≈ 25 mm), the precision of the normal strain will be 0.002% and the precision of the shear strain will be $\tan^{-1} 0.00002 \approx 0.00002$.

2.4 Preliminary test results

Uniaxial monotonic tensile test

A uniaxial monotonic tensile test was first performed. The strain was measured simultaneously with both extensometer and this new non-contact system. Results from these two methods are compared in Fig.2.7, from which one can see good agreement between them. The small discrepancy at larger strain might result from nonlinear output of the extensometer at high strain levels.

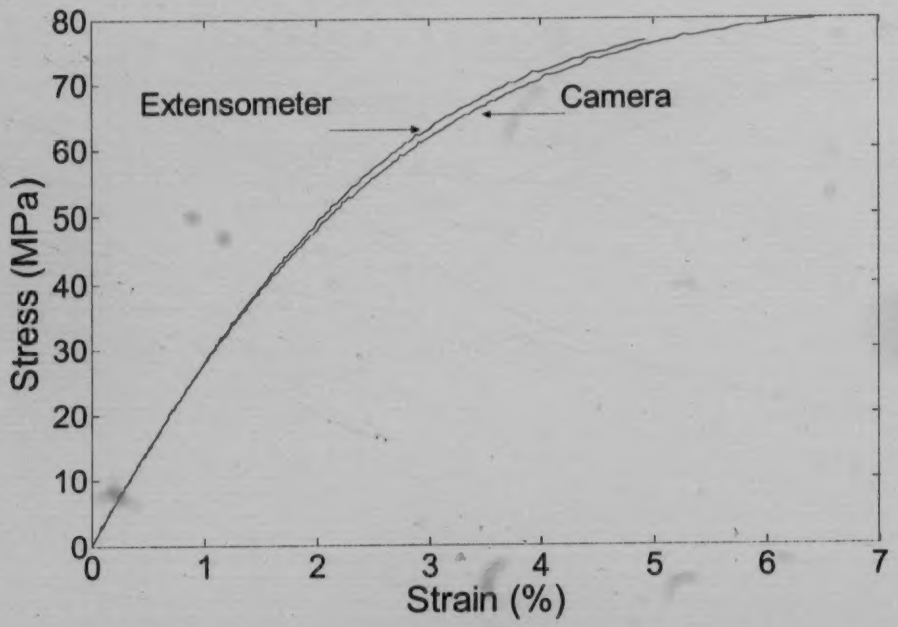

Fig. 2.7 Comparison of recorded stress-strain curves by using traditional extensometer and using the non-contact real-time strain measurement and control system.

Stress-controlled uniaxial tensile cyclic test with mean stress

A stress-controlled uniaxial cyclic test was carried out with stress range of 60 MPa and mean stress of 30 MPa. Fig.2.8 (a) and (b) show the stress-strain loops of the first 5 cycles and 1st, 20th, 50th and 100th cycle. Maximum and minimum strains of each cycle are plotted in Fig.2.8 (c) and (d), respectively.

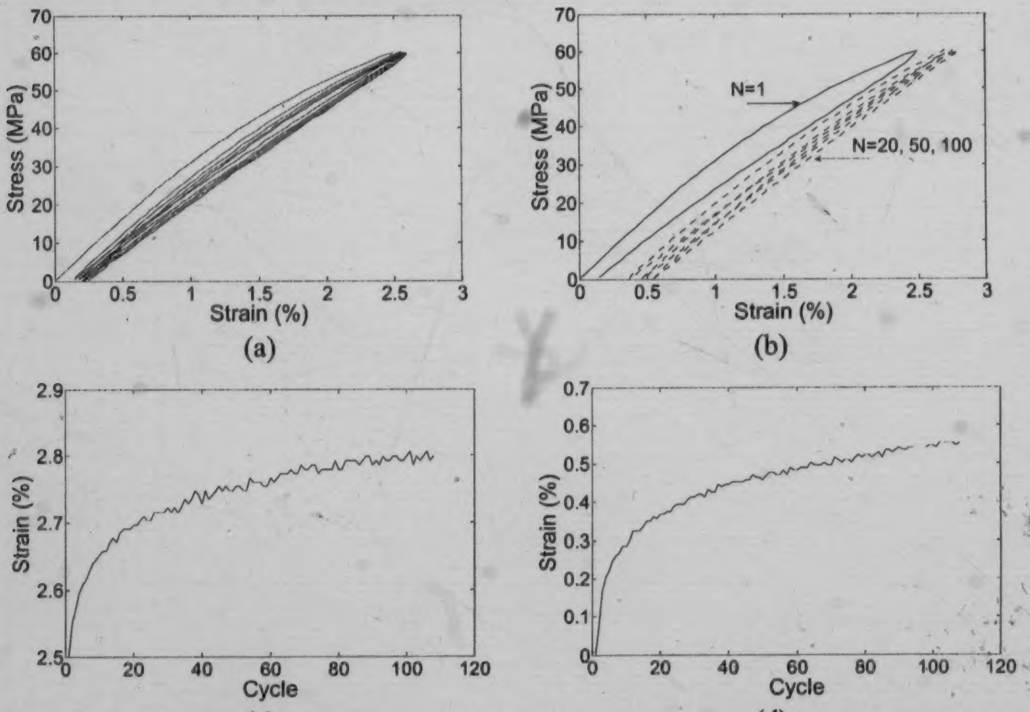

(a) (b)

(c) (d)

Fig. 2.8 Stress-controlled uniaxial cyclic test with mean stress: (a) stress-strain loops of the first 5 cycles; (b) stress-strain loops of the 1st, 20th, 50th and 100th cycle; (c) maximum strains of each cycle; (d) minimum strains of each cycle.

Nonlinear behavior of this material is manifest at higher strain levels. It is noticed from the figures that, with increasing cycles, the stress-strain loops tend to be slimmer and more linear. Ratcheting strain is accumulated from the very beginning of loading and the ratcheting rate decreased cycle by cycle. The ratcheting strain rate became almost zero after the 20th cycle, i.e. an asymptotic stable state has been reached. Total ratcheting strains at the maximum and minimum stresses are 0.3% and 0.55%, respectively. This specimen failed at the 109th cycle.

Strain-range-controlled uniaxial cyclic tests with mean strain

A strain-range-controlled uniaxial cyclic test was also carried out with strain range of 3.2% and mean strain of 1.6%. Fig.2.9 (a) and (b) show the stress-strain loops of the first 5 cycles and the 1st, 50th and 238th cycle. Maximum and minimum stresses of each cycle are plotted in Fig.2.9 (c) and (d). It can also be noticed that, with the increase of cycles, the stress-strain loops tend, again, to be slimmer and more linear. Stress relaxation occurs from the very beginning of testing and the relaxation rate is decreasing with increasing cycles. One can also distinguish that after the 50th cycle the relaxation rate is almost zero and a stable state has been reached. Total stress relaxations at the maximum and minimum strains are -2 MPa and -7 MPa, respectively. This specimen fractured at 239th cycle. It is noted that the strain range in the previous stress-controlled test is about 2.5% (Fig. 7a and b) while in the current test the strain range is 3.2%. However, the fatigue life of the latter is even longer than that of the former. This might be attributed to the different characteristics in the stress/strain responses of the different load control modes. In the former, the ratcheting strain could be a detrimental factor to the fatigue life, while the stress relaxation in the latter could be a beneficial factor to the fatigue life of the materials.

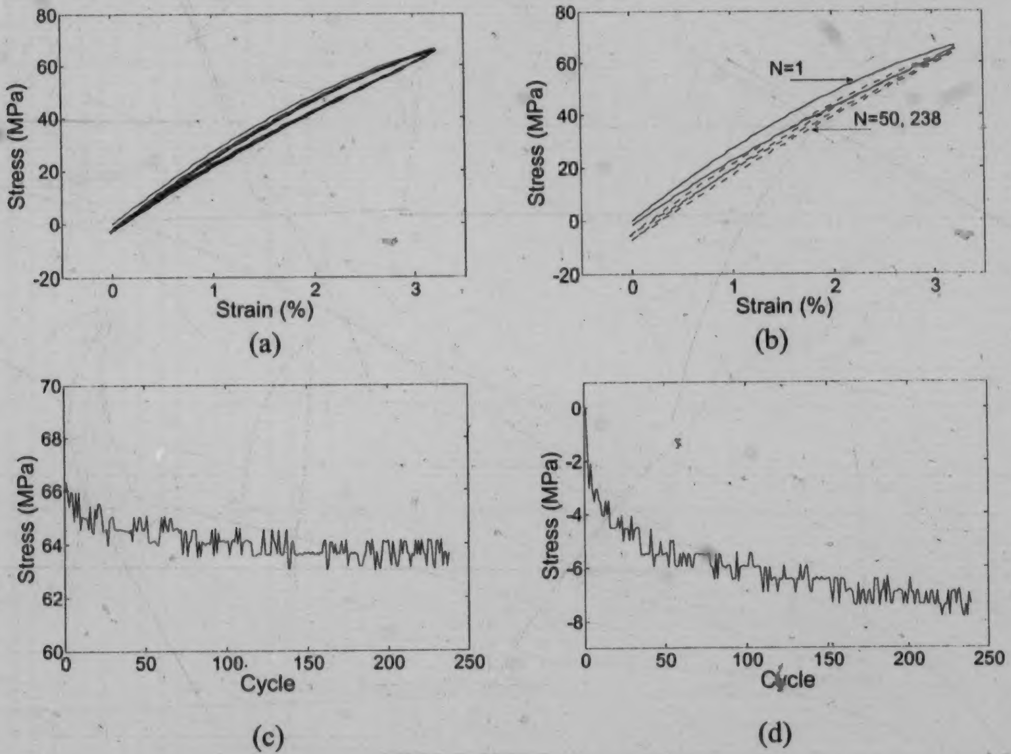

(a) (b) (c) (d)

Fig. 2.9 Strain-range-controlled uniaxial cyclic test with mean strain: (a) stress-strain loops of the first 5 cycles; (b) stress-strain loops of the 1st, 50th and 238th cycle; (c) maximum stresses of each cycle; (d) minimum stresses of each cycle.

Stress-controlled pure shear cyclic test with mean stress

A stress-controlled pure shear cyclic test was performed with shear stress range of 36 MPa and mean stress of 18 MPa. Fig.2.10 (a) and (b) show the stress-strain loops of the first 5 cycles and 1st, 100th, 1000th and 3000th cycle. Maximum and minimum shear strains in each cycle are plotted in Fig.2.10 (c) and (d). Similar to the axial loading tests, the stress-strain loop became slimmer and more linear with increasing cycles. Moreover, ratcheting shear strain was accumulated from the first cycle and its rate decreased with increasing cycles. It is also noticeable that after the 500th cycle the ratcheting rate is almost zero, indicating an asymptotical stable stage reached. It has been reported that the epoxy polymer behaves more plastic under shear mode than tensile mode (Fiedler et al., 2001). However, in comparison of the uniaxial ratcheting strain in Fig.2.8 and the shear ratcheting strain in Fig.2.10, no distinctive difference can be seen between cyclic tension and shear when converte them to the equivalent strains.

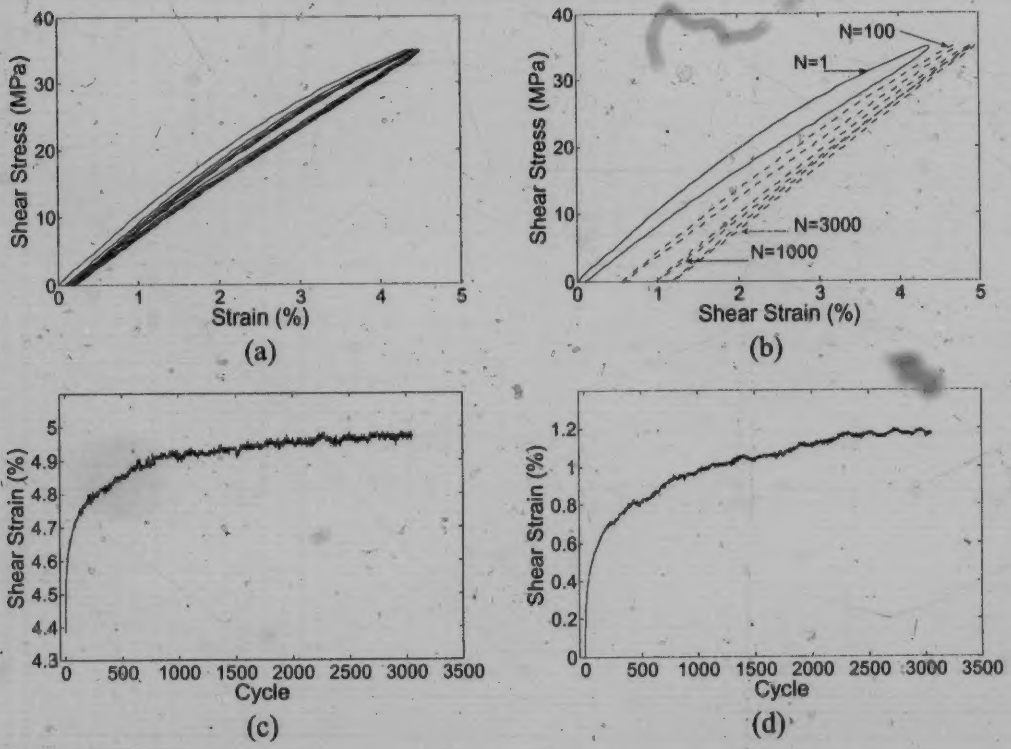

Fig. 2.10 Stress-controlled pure shear cyclic test with mean stress: (a) stress-strain loops of the first 5 cycles; (b) stress-strain loops of the 1st, 100th, 1000th and 3000th cycle; (c) maximum shear strains of each cycle; (d) minimum shear strains of each cycle.

Proportional strain-range-controlled biaxial cyclic test

A proportional axial-shear biaxial cyclic test was performed under strain-range-controlled mode with axial strain range between 0% and 2.06%. The shear loading rate was kept proportional to the axial one in this test. From the experimental results we noticed that, although only axial strain range was controlled, the shear strain was also kept within a constant range during the entire test process. Therefore, proportional strain-range-controlled biaxial cyclic tests can be successfully performed by constrained the strain range in only one direction. Fig.2.11 (a) and (b) show the stress-strain loops of the first 5 cycles and 50th, 1000th and 1700th cycles in the axial and shear directions, respectively. Fig.2.11 (c) and (d) show the mean stresses of each cycle in the axial and shear directions, respectively. Nonlinear behavior can be noticed in both directions and both the axial and shear stress-strain loops become slimmer and more linear with increasing cycles. Stress relaxation occurred in both directions and the rates decreased with increasing cycles. Total mean stress relaxations are 4.0 MPa and 2.2 MPa in axial and shear direction, respectively. This specimen failed at the 1716th cycle.

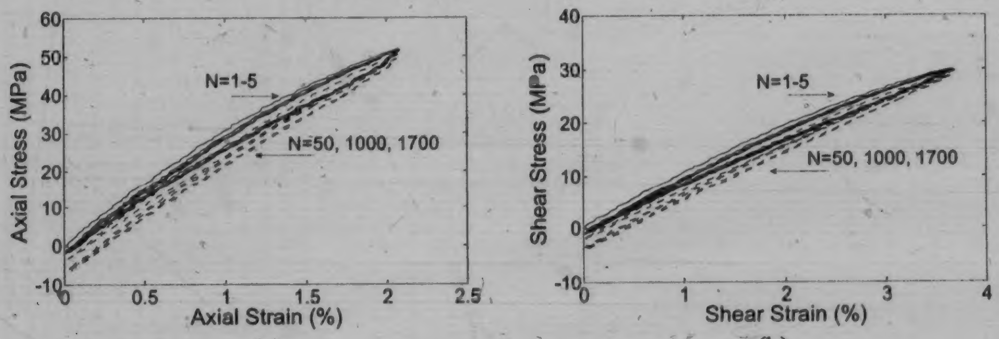

(a) (b)

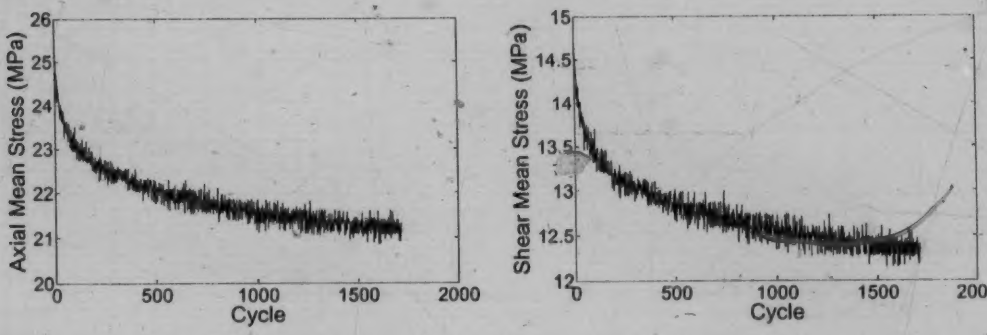

(c) (d)

Fig. 2.11 Proportional strain-range-controlled biaxial cyclic test under combined axial-shear loading: (a) axial stress-strain loops of the first 5 cycles and the 50th, 1000th and 1700th cycle; (b) shear stress-strain loops of the first 5 cycles and the 50th, 1000th and 1700th cycle; (c) axial mean stress in each cycle; (d) shear mean stress in each cycle.

Non proportional stress-controlled biaxial cyclic test

A non-proportional biaxial test was also carried out under stress-controlled mode with axial stress range of 0-50 MPa and shear stress range of 0-28 MPa. Fig.2.12 (a) shows the quarter-circle sectorial loading path of this test. Fig.2.12 (b) shows the fan-shaped strain response of the first 10 cycles and 50th, 200th and 700th cycles of this test. Mean strains of each cycle in the axial and shear directions are plotted in Fig.2.12 (c) and (d), respectively. It is also noticed that ratcheting strains are accumulated in both axial and shear directions. Total ratcheting mean strains are 0.38% and 0.44% in axial and shear directions, respectively. After the 400th cycle the ratcheting rates become zero and material response is in a stable stage. After the 550th cycle, ratcheting rates are seen to increase again until final failure. Such phenomenon is more pronounced in the axial direction. This specimen failed at the 716th cycle.

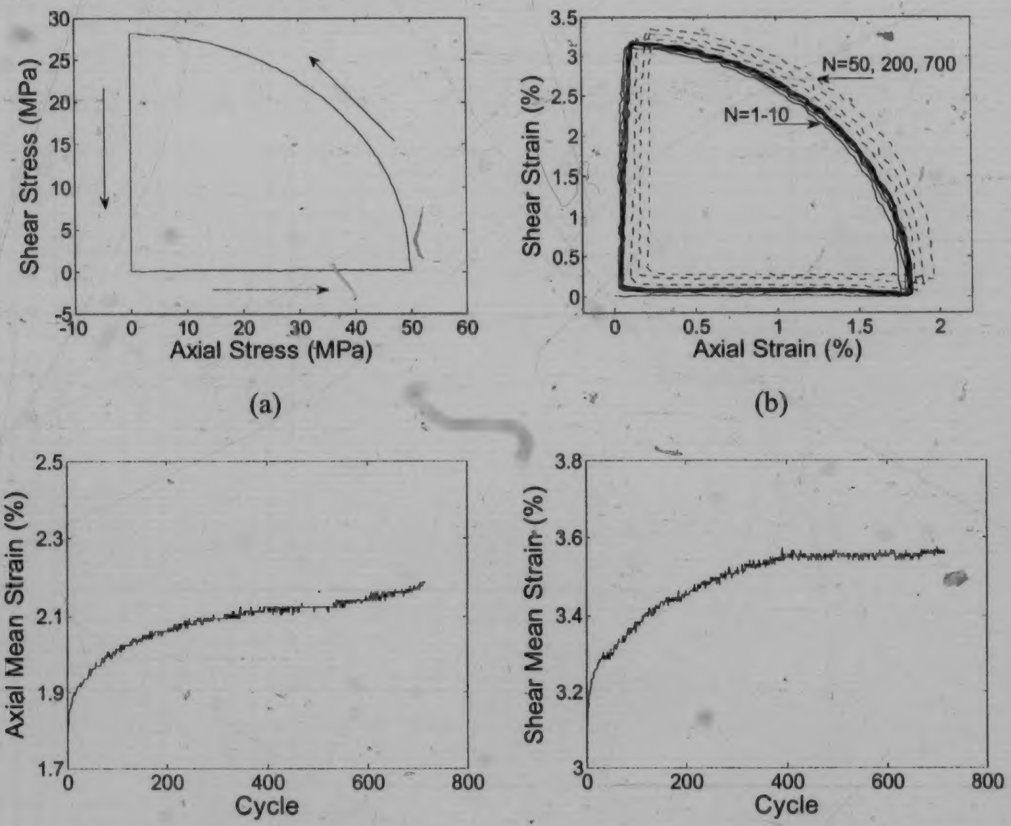

(a) (b)

(c) (d)

Fig. 2.12 Non-proportional stress-controlled biaxial cyclic test under combined axial-shear loading: (a) biaxial loading path; (b) biaxial strain response of the first 10 cycles and the 50th, 200th and 700th cycle; (c) axial mean strain in each cycle; (d) shear mean strain in each cycle.

2.5 Discussions

Due to the required time for digital image processing, the sampling frequency of the current system is not [illegible] high as that by using the traditional strain gauge or extensometer. Three kinds of delays affect the total delay time of the system, the exposure time of the CCD camera, the time required for transferring the image from CCD to frame grabber and the image processing time. The first two factors depend on the camera itself. In our case, the exposure time and the transfer time is 1/30 seconds or 1/60 seconds depending on the operation mode of the camera. Therefore, the total delay time will be 1/15 seconds or 1/30 seconds plus the image processing time. In our system, the average processing time for two 12×12 pixels subsets is 0.005 seconds as shown in Fig.2.13, which was recorded during a fatigue test. Then the feedback strain signal would be delayed about 0.072 seconds or 0.038 seconds depending on the operation mode of the camera.

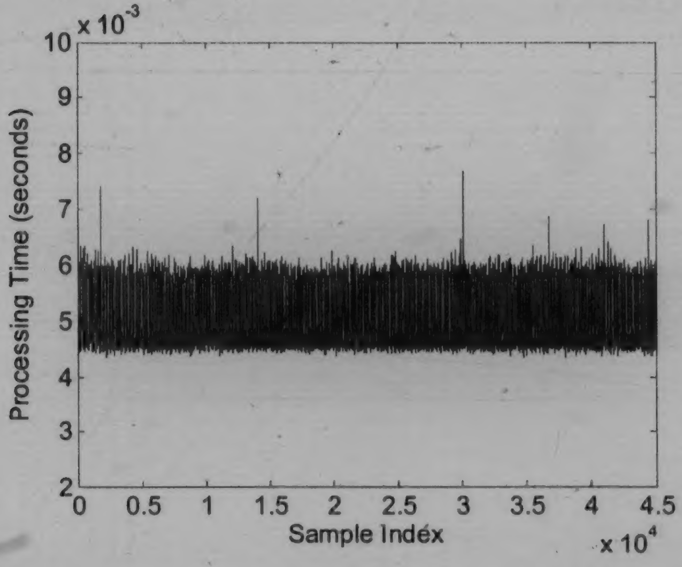

Fig. 2.13 Processing time of the non-contact real-time strain measurement system.

During this period the machine actuator was kept to increase the load until the computer recognized that the strain exceeded the limit and commanded the machine to reverse the load direction. Therefore, the actual strain peak values (maximum and minimum strains) that the specimen was subjected to, would be larger than the predefined limit. Because of the influence of several other factors, such as sampling frequency and the loading rate, the actual strain limit will slightly fluctuate around its mean value from cycle to cycle. The maximum sampling frequency of this system is 60 Hz, which is limited by the camera model. Theoretically, increase of sampling frequency will enhance the precision of capturing the peak strains and, therefore, suppress the fluctuation of the measured strain limit values. The degree of the fluctuation is also determined by the loading rate. Higher loading rate will intensify the fluctuation because the strain increment will be larger than that under lower loading rate within the same data sampling interval. Moreover, the inertia of the actuator will also lead to such fluctuation. Fig.2.14 (a) and (b) show the histogram of the deviation of the maximum and minimum strain of each cycle to their mean value in the 0% – 3.2% strain-range-controlled fatigue test, respectively. The loading rate is 10MPa/s, which was chosen as the unified loading rate for each strain-range-controlled uniaxial fatigue test in the current study. The sampling frequency of this test is 10Hz. The mean value and standard deviation of the maximum strain of all cycles in the test are 3.2% and 0.026%, respectively. The mean value and standard deviation of the minimum strain of all cycles are 0% and 0.014%, respectively. The mean value and standard deviation of minimum strain is slightly lower than that of the maximum strain. This can be explained by this kind of epoxy material having lower stiffness at high stress level. Therefore, the strain rate is higher at higher stress level than that at lower stress level under the same absolute loading rate. According to Fig.2.14 (a), the maximum error in the peak strain is about 0.06%, and then the relative maximum error of the strain range is about 1.9%. Such small error should have very little effect on the fatigue life of the specimen.

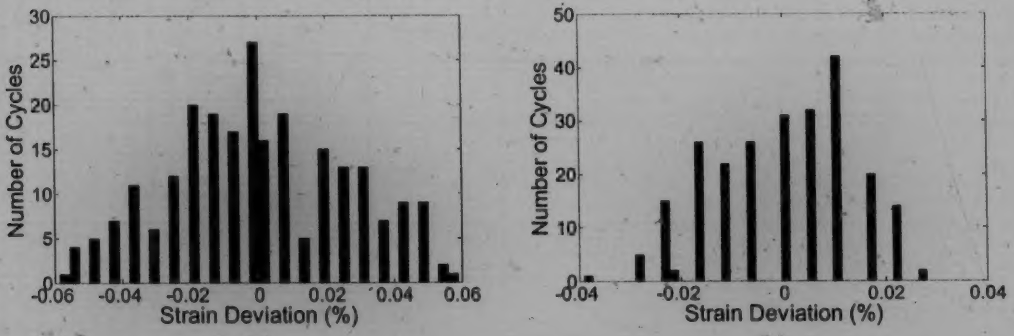

(a) (b)

Fig. 2.14 Histograms of the deviation of the strain range: (a) the deviation of the maximum strain; (b) the deviation of the minimum strain.

2.6 Conclusions

A non-contact real-time strain measurement and control system based on digital image correlation technique has been established. The method is non-destructive and has no upper limitation for the strain measurement. Therefore, it can be used in multiaxial fatigue tests of soft materials such as polymers. Currently the system can measure strains with an accuracy of 0.002% and a maximum frequency of 60 Hz for strain data acquisition. As such, the system even allows running strain-range-controlled fatigue tests with moderate loading rates. The capability of the system has been verified through recording the stress-strain responses of various types of uniaxial and biaxial cyclic/fatigue tests of an epoxy polymer material. The results show that the evolution of stress-strain hysteresis loops during the entire fatigue life of the specimen can be accurately recorded. The different responses in the stress and the strain-range-controlled tests also indicate the significant effect of the loading modes on the fatigue behavior and fatigue life of viscoelastic/viscoplastic and time-dependent materials such as polymers. The success of this method would facilitate performing various types of fatigue tests on polymer materials and would allow us to gain a more insight and understanding of the fatigue and failure behaviors of the polymer materials. This system has potential for further upgrade in the future. Utilization of a higher resolution CCD camera will improve the strain detection precision. It will be possible to further reduce the processing time and to increase the strain data acquisition frequency if the computer and the CCD camera possess higher speeds than the current used ones.

Bibliography

1. Brown RP, Physical Testing of Rubber, 2nd ed. Elsevier Applied Science Publishers, London and New York, 1986.
2. Bruck HA, McNeill SR, Sutton MA, Peters WH. Digital Image Correlation Using Newton-Raphson Method of Partial Differential Correlation. Experimental Mechanics 1989; 29(3):261-7.
3. Chu TC, Ranson WF, Sutton MA, Peters WH. Applications of Digital-Image-Correlation Techniques to Experimental Mechanics. Experimental Mechanics 1985; 25(3):232-44.
4. Ellyin F. Fatigue Damage, Crack Growth, and Life Prediction. Chapman & Hall, London, UK, 1997.
5. Ellyin F, Wolodko JD. Testing Facilities for Multiaxial Loading of Tubular Specimens, Proceedings of the 1995 Symposium on Multiaxial Fatigue and Deformation Testing Techniques, SAE STP 1280, Denver, Colorado, 1997. p. 7-24.
6. Erf RK. Speckle Metrology. Academic Press, New York. 1978.
7. Fiedler B, Hojo M, Ochiai S, Schulte K, Ando M. Failure behavior of an epoxy matrix under different kinds of static loading. Compo Sci Tech 2001; 61(11):1615-24.
8. Han G, Sutton MA, Chao YJ. A study of stationary crack-tip deformation fields in thin sheets by computer vision. Experimental Mechanics 1994; 34(2):125-40.
9. Ives GC, Mead JA, Riley MM, Handbook of Plastics Test Methods, CRC Press, Cleveland, Ohio, 1971.

10. Joenathan C, Franze B, Haible P, Tiziani HJ. Speckle interferometry with temporal phase evaluation for measuring large-object deformation. Applied Optics 1998; 37(13):2608-14.

11. Kanchanomai C, Yamamoto S, Miyashita Y, Mutoh Y, McEvily AJ. Low cycle fatigue test for solders using non-contact digital image measurement system. International Journal of Fatigue 2002; 24(1):57-67.

12. Li X, Tao G. Low-frequency harmonic vibration analysis with temporal speckle pattern interferometry. Optics & Laser Technology 2002; 34(3):259-64.

13. Li X, Tao G, Yang Y. Continual Deformation Measurement with Scanning Phase Method and Time Sequence Phase Method in Temporal Speckle Pattern Interferometry. Optics & Laser Technology 2001b; 33(1):53-9.

14. Li X, Yang Y, Tao G, Li R. Deformation Analysis with Temporal Speckle Pattern Interferometry. Optical Engineering 2001a; 40(2):310-7.

15. Lorenzo L, Hahn HT. Effect of Ductility on the Fatigue Behavior of Epoxy Resins. Polymer Engineering and Science 1986; 26(4):274-84.

16. Luo PF, Chao YJ, Sutton MA, Peters WH. Accurate measurement of three-dimensional deformations in deformable and rigid bodies using computer vision. Experimental Mechanics 1993; 33(2):123-32.

17. McNeill SR, Sutton MA, Miao Z, Ma J. Measurement of Surface Profile Using Digital Image Correlation. Experimental Mechanics 1997; 37(1):13-20.

18. Nagasawa M, Kinuhata H, Koizuka H, Miyamoto K, Tanaka T, Kishimoto H, Koike

H. Mechanical fatigue of epoxy resin. Journal of Materials Science 1995; 30(5):1266-72.

19. Peters WH, Ranson WF. Digital imaging techniques in experimental stress analysis. Optical Engineering 1982; 21(3):427-31.
20. Rae PJ, Palmer S, Goldrein HT, Lewis AL, Field JE. White-light digital image cross-correlation (DICC) analysis of the deformation of composite materials with random microstructure. Optics and Lasers in Engineering 2004; 41(4):635-48.
21. Sauer JA, Richardson GC. Fatigue of polymers. International Journal of Fracture 1980; 16(6):499-532.
22. Shen X, Xia Z, Ellyin F. Cyclic Deformation Behavior of an Epoxy Polymer. Part I: Experimental Investigation. Polymer Engineering and Science 2004; 44(12):2240-6.
23. Sirohi RS, editor. Speckle Metrology. Marcel Decker, New York. 1993.
24. Takemori MT. Polymer Fatigue. Annual Review of Materials Science 1984; 14:171-204.
25. Tao G, Li X, Shi H. Study of Ballistite Material Mechanical Behaviors Using Temporal Speckle Pattern Interferometry. Mechanics of Materials 2004; 36(3):275-83.
26. Trotignon JP, Verdu J, Morel E. Roughness effects on the fatigue behavior of an epoxy matrix. Journal of Materials Science letters 1991; 10(14):844-6.
27. Yamaguchi I. A Laser-Speckle Strain-Gauge. Journal of Physics E: Scientific Instruments 1981; 14(11):1270-3.

Chapter 3

Uniaxial Fatigue Behavior

3.1 Introduction

Epoxy polymer materials have been increasingly utilized in modern industries. They have been applied as alternatives to conventional metal materials in many areas due to their unique properties, such as chemical corrosion resistance and electric insulation. For composite materials with epoxy matrix, high specific strength and stiffness are their superior advantages. Therefore, research on fatigue behavior of epoxy polymer materials is important for understanding damage mechanisms of structures made of epoxies and epoxy matrix composites. In the latter structures fatigue crack usually initiates from the relatively weak epoxy matrix or interface between the matrix and reinforcing phase.

Although there have been numerous works on fatigue behaviors of thermoplastics and polymeric composites, studies on pure epoxy polymers have been relatively few in comparison to the these two types of materials. Some reviews on fatigue behavior of epoxy polymers are presented in Chapter 1. However, some critical issues relating to the fatigue behavior of epoxy materials have not been carefully investigated, for example, the effects of various loading conditions (stress/strain controlled mode, mean stress/mean strain, ratcheting strains/stress relaxation, multiaxial loading paths etc.), the evolutions of various mechanical properties (elastic modulus, stress/strain range, strain energy densities, etc.) during cyclic loading process. This insufficiency may partly be attributed to the unavailability of an effective technique to accurately record stress-strain hysteresis loops during full fatigue life of the specimens. Due to the inapplicability of conventional extensometers in fatigue tests of soft polymers, not surprisingly, almost all the fatigue tests of polymers were conducted under stress-controlled mode or displacement-controlled mode. The actual strains in the gauge area were unable to be carefully monitored for the entire fatigue test process. Thus, it was difficult to make an accurate assessment on the change of mechanical properties during the cyclic fatigue process. And various loading effects on fatigue life of polymers are also difficult to be characterized.

A non-contact real-time strain measurement and control system described in Chapter 2 provides a platform to implement the strain-range-controlled fatigue tests and has ensured the acquisition of accurate stress-strain data during the entire fatigue test. In this chapter, results of various uniaxial fatigue tests under strain-range-controlled mode and stress-controlled mode are presented. The stress-strain hysteresis loops, recorded during the entire fatigue life of each specimen, are utilized to identify the evolutions of various mechanical properties of the epoxy polymer material. Series of fatigue tests with mean strains were conducted and the mean stress/strain effect on fatigue life is identified. Effect of ratcheting strain on fatigue life is also investigated and the results are presented.

Fractographic analysis was performed based on photographs from both an optical microscope and Scanning Electronic Microscope (SEM). And the fatigue mechanism is discussed.

3.2 Fatigue behavior under fully-reversed loading

In total, 13 fully-reversed fatigue tests at 10 different strain amplitude levels were carried out. All the tests were conducted at room temperature and under the laboratory environment. Among these, 3 were repeated at low, medium and high strain amplitude levels for consistency verification, respectively. All the tests were performed under strain-range-controlled mode with loading rate of 10MPa/s (absolute value) except those two tests with longest lives, which were conducted under stress-controlled mode with loading rate of 100MPa/s for the sake of reducing test time. At low strain level, stress-controlled mode and strain-controlled mode are equivalent since the material response is dominantly elastic and there is neither distinct plasticity nor time-dependent viscoelasticity. The corresponding loading frequencies of all tests were from 0.03Hz to 0.7 Hz. Therefore it guaranteed that no considerable temperature raise could occur during the tests. A non-contact infrared thermometer was used to monitor the surface temperature during the test of the specimen under the highest loading rate. No detectable temperature raise was observed. To confirm the equivalence of strain-range-controlled and stress-controlled mode at low strain amplitude level, another cyclic test was performed under strain-range-controlled mode at a loading rate of 10MPa/s with a strain range of ±1.39%. This was comparable to the test with the second longest life which was under the stress-controlled mode. For the two tests, almost no change was observed for the stress-strain relationship which was kept linear during the entire test period. The test with the longest life was stopped at 1,000,000th cycle and the corresponding strain amplitude of 1.3% was considered as the fatigue limit ($N_f > 10^6$).

3.2.1 Strain Range – Fatigue Life relation

The phenomenological approach to predict fatigue life can be generally divided into three categories: stress-based, strain-based and energy-based approaches. In the case of the strain-range-controlled fatigue test, a strain-based approach can be adopted. The relation between the strain amplitude $\Delta\varepsilon/2$ and the fatigue life N_f (cycles to failure) can be described by the Wöhler's equation (1871):

$$\frac{\Delta\varepsilon}{2} = \kappa \cdot N_f^{\gamma} + \frac{\Delta\varepsilon_{FL}}{2} \tag{3.1}$$

where κ and γ are material constants and $\frac{\Delta\varepsilon_{FL}}{2}$ corresponds to the fatigue limit. From Fig.3.1 it can be seen that the data can be well fitted with $\gamma = -0.347$, $\kappa = 0.10$ and $\frac{\Delta\varepsilon_{FL}}{2} = 1.3\%$.

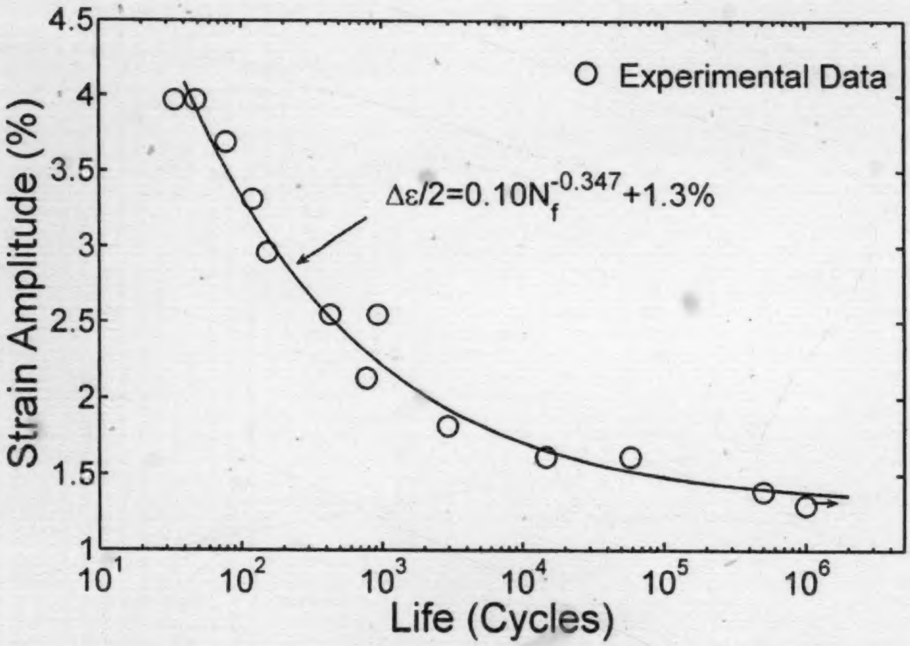

Fig. 3.1 Strain amplitude vs. fatigue life curve from strain-range-controlled fully-reversed uniaxial fatigue tests.

3.2.2 Evolution of mechanical properties

Hysteresis loops were obtained from the strain-range-controlled tests at 8 different strain amplitude levels. Fig.3.2(a) shows the hysteresis loops at the first cycle, the mid-life cycle and the last cycle of a fully-reversed uniaxial fatigue test at the highest strain amplitude level. The material shows a remarkable nonlinear stress-strain relationship at high strain level. Distinct differences can be seen on the shape of the hysteresis loops at 3 different stages. This can be attributed to the changes of various mechanical properties, which will be evaluated in more detail in the following sub-sections. Fig.3.2(b) shows the hysteresis loops at the first cycle, the mid-life cycle and the last cycle of a fully-reversed uniaxial fatigue test at the lowest strain amplitude level. Stress-strain exhibits a dominantly linear relationship at such low strain level and only a very small change in the shape of the stress-strain hysteresis loops can be detected.

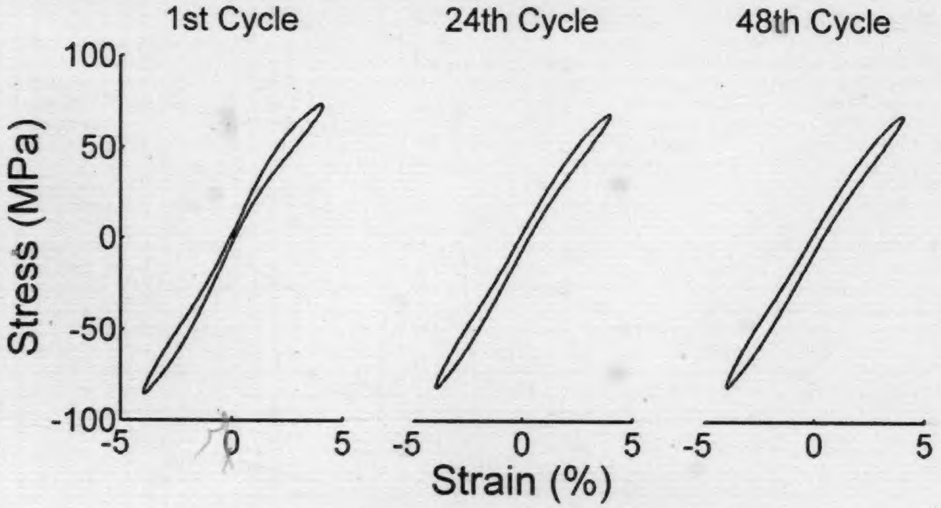

(a) The test with the highest strain range level;

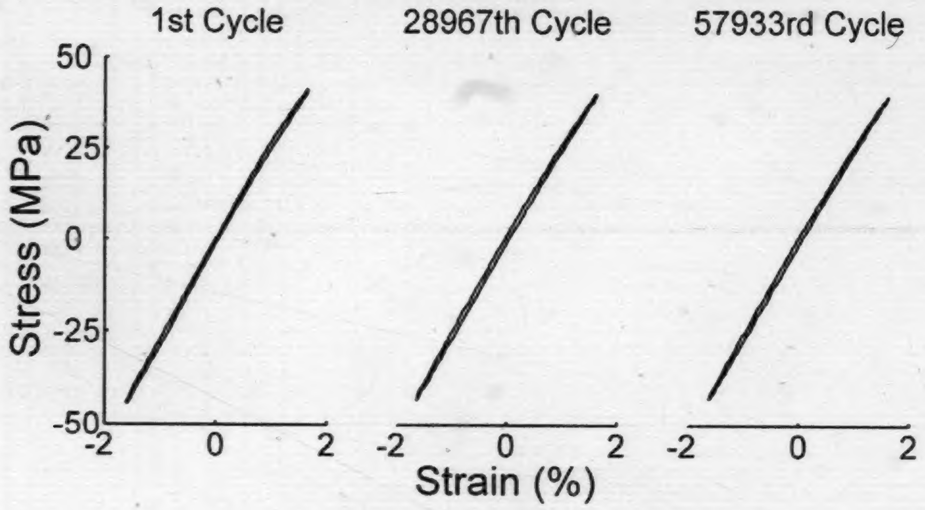

(b) The test with the lowest strain range level;

Fig. 3.2 Hysteresis loops of strain-range-controlled fully-reversed uniaxial fatigue tests

- **Stress range drop**

The evolution of stress ranges with respect to the cycles under different strain ranges is shown in Fig.3.3. For this epoxy polymer material, cyclic softening was observed in all fully-reversed uniaxial cyclic tests. An approximate linear relation of stress range with respect to cycles can be seen in the semi-log scale. The slope tends to decrease with the decreasing strain range. The following function relation seems to fit the data quite well:

$$\Delta\sigma = \Delta\sigma_o + \alpha \cdot \log N \tag{3.2}$$

where N is the number of cycle, $\Delta\sigma_o$ is the initial stress range in the first cycle and α can be understood as a evolution coefficient. The α and $\Delta\sigma_o$ are both functions of the strain range. Based on the individual experimental curve in Fig.3.3, the $\Delta\sigma_o - \Delta\varepsilon$ relation can be fitted by a Ramberg-Osgood equation:

$$\Delta\varepsilon = \frac{\Delta\sigma_o}{2900} + \left(\frac{\Delta\sigma_o}{460}\right)^{\frac{1}{0.28}} \tag{3.3}$$

Note that $\alpha = 0$ and $\Delta\sigma_o = 0$ when $\Delta\varepsilon = 0$. An exponential function expressed in Eq.(3.4) can be used to fit the $\alpha - \Delta\varepsilon$ relation,

$$\alpha = 0.094(1 - e^{52.7 \cdot \Delta\varepsilon}) \tag{3.4}$$

The simulation of evolutions of stress range at different stain range levels by the Eq.(3.2)-(3.4) are plotted against the experimental data in Fig.3.3.

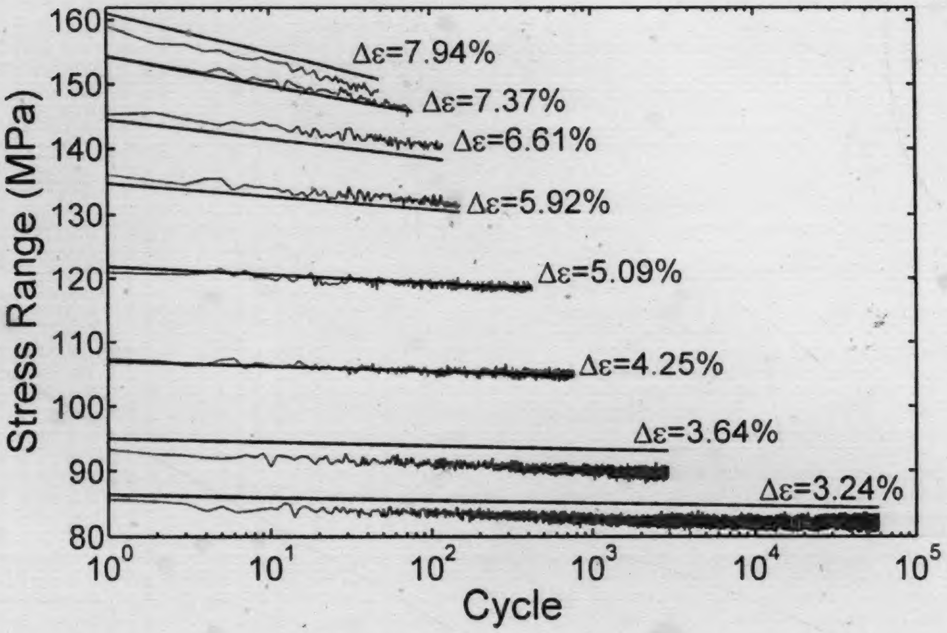

Fig. 3.3 Evolutions of stress range during the entire fatigue life period of the strain-range-controlled fully-reversed uniaxial fatigue tests. The lines with fluctuations are from experiments and the smooth lines are simulations.

- **Modulus drop**

The modulus can be calculated from the stress-strain curve at the initial part of the loading stage in each cycle. Modulus drop was observed for this epoxy polymer during the cyclic loading. Further investigation under various loading conditions revealed that the modulus drop is independent of the loading strategy, such as the control mode (stress-control or strain-range-control) and the value of mean stress/strain. The modulus drop under the strain-range-controlled fatigue test during the entire life is plotted in

Fig.3.4. It can be seen that the overall drop of the modulus decreases with the decreasing strain amplitude. For the cycling under smaller strain amplitude, the modulus drops mainly during the early stage of cycles and a stable modulus value remains until the final failure. For the tests with larger strain amplitude the modulus drop covers the entire fatigue life. The following equation is used to fit the modulus drop data:

$$E = E_0 - E_d(1 - N^{\beta}) \tag{3.5}$$

where N is the number of cycles, β is the modulus drop coefficient, $E_0 = 2900\,\text{MPa}$, which is the modulus of the specimen at the virgin stage (first cycle). Its value was determined by the average value of the initial modulus of all the 13 tests. E_d is a function of strain range $\Delta\varepsilon$. Since the modulus was obtained by fitting several data points in the initial part of loading stage, there was high noise level in the original modulus value. Thus, the modulus data were smoothed first by a moving average filter. Then the smoothed data were fitted with Eq.(3.5) by least square algorithm for each individual strain level. β is not sensitive to the change of the strain range $\Delta\varepsilon$, so β is unified as the average value of all the 13 tests as -0.466. The relation of E_d with respect to $\Delta\varepsilon$ is fitted with the following equation,

$$E_d = 532(e^{13.2\Delta\varepsilon} - 1) \tag{3.6}$$

Substitute Eq.(3.6) into Eq.(3.5), an evolution function $E(\Delta\varepsilon, N)$ is obtained. For different strain range level, function $E(\Delta\varepsilon, N)$ is plotted against the experimental data in Fig.3.4, where good agreement can be seen.

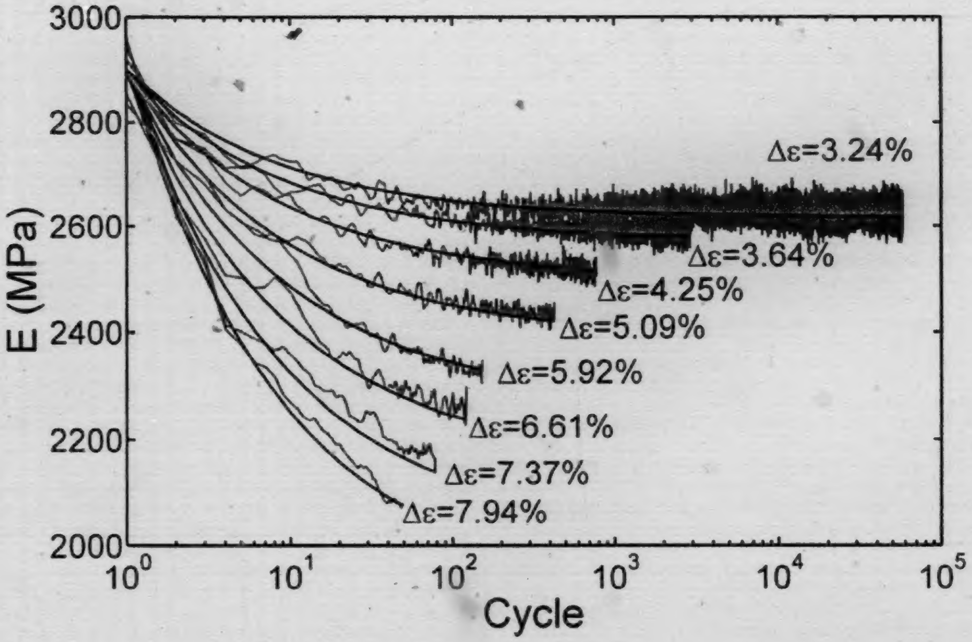

Fig. 3.4 Evolutions of modulus during the entire fatigue life period of the strain-range-controlled fully-reversed uniaxial fatigue tests. The lines with fluctuations are from experiments and the smooth lines are simulations.

- **Decrease of nonlinear effect in stress-strain relation**

By observing the evolution of the hysteresis loops, one can find that the nonlinear effect of stress-strain relationship tends to decrease with increasing cycles. Here, the nonlinear strain range, $\Delta\varepsilon^{nl}$ is defined as

$$\Delta\varepsilon^{nl} = \Delta\varepsilon^{t} - \frac{\Delta\sigma}{E} \tag{3.7}$$

where $\Delta\varepsilon^{t}$ is the total strain range, $\Delta\sigma$ and E are the stress range and elastic modulus of each cycle. The evolution of the nonlinear strain range with respect to the number of cycles is plotted in Fig.3.5. For the tests with larger strain amplitude, $\Delta\varepsilon^{nl}$ drops continuously until the failure and there is no stable stage. While in the tests with lower strain amplitude levels, $\Delta\varepsilon^{nl}$ drops only slightly within the initial several cycles and a saturated stable value is kept during the rest of fatigue life.

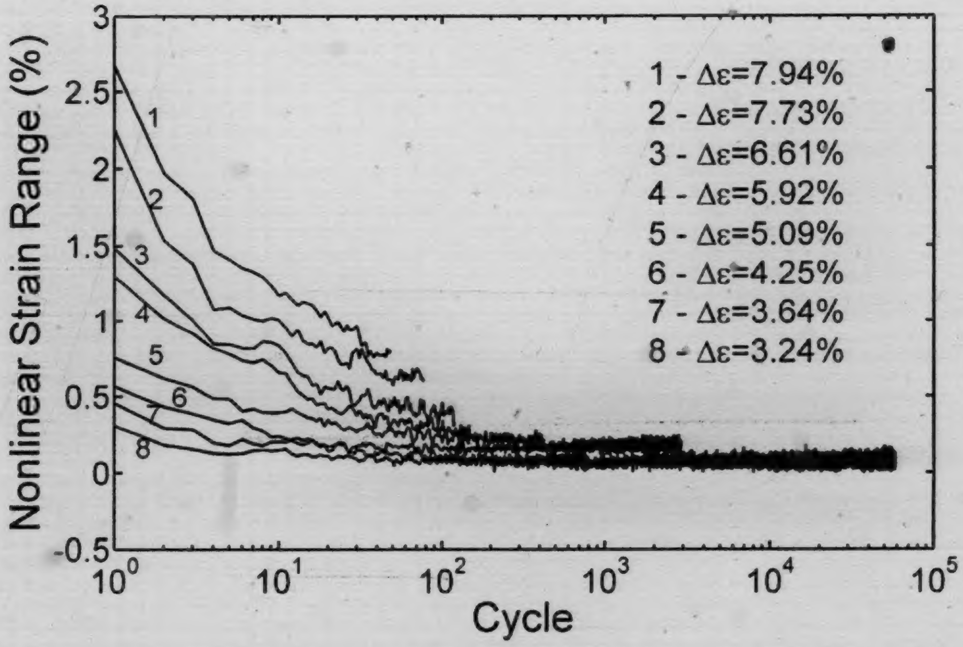

Fig. 3.5 Evolutions of nonlinear strain range during the entire fatigue life period of strain-range-controlled fully-reversed uniaxial fatigue tests.

- **Increase of dissipated strain energy density per cycle**

The dissipated strain energy density per cycle was calculated from the area of the hysteresis loop and its evolution with the number of cycles is shown in Fig.3.6. The dissipated strain energy density per cycle increases with the increase of the number of cycles for the tests with larger strain amplitude, whereas at lower strain amplitude it keeps nearly constant during the entire fatigue life.

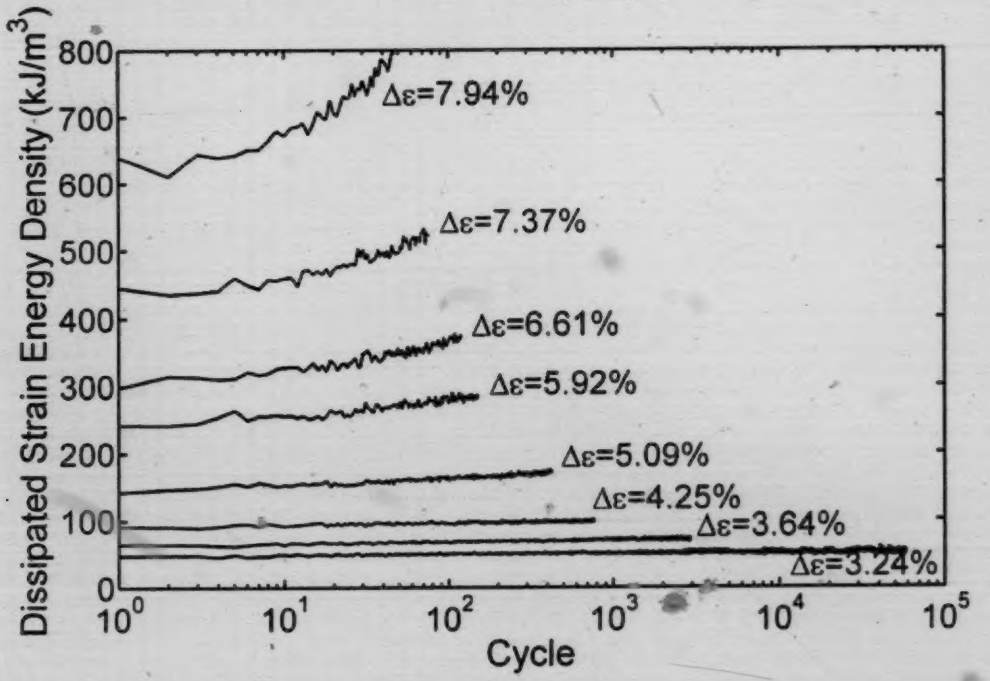

Fig. 3.6 Evolutions of dissipated strain energy density per cycle during the entire fatigue life period of strain-range-controlled fully-reversed uniaxial fatigue tests.

3.2.3 Preliminary tests on mean strain effect

To investigate the effect of mean strain on the mechanical response and fatigue life, three extra strain-range-controlled tests were conducted with approximately the same strain amplitude of 1.82% but with different mean strain values. Mean strain ratio is defined as:

$$R_m = \frac{\varepsilon_m}{\varepsilon_a} \tag{3.8}$$

where ε_m is the mean strain and ε_a is the strain amplitude. Values of R_m of these tests were -0.33, 0.33 and 1, respectively. These test results are compared to the one with the same strain amplitude under fully-reversed loading condition, i.e. $R_m = 0$. The test conditions and resulting fatigue lives are listed in Table 3.1.

Table 3.1 Test conditions and fatigue lives of strain-range-controlled uniaxial fatigue tests with same strain amplitude but different mean strain ratios

Strain Range	R_m	**Fatigue Life (Cycles)**
-2.43% - 1.21%	-0.33	22370
-1.81% - 1.83%	0	2910
-1.18% - 2.44%	0.33	787
0.02% - 3.68%	1	318

It is obvious that for the same strain amplitude, the fatigue life decreases with increasing value of R_m. The evolutions of stress range of the four tests are shown in Fig.3.7. It is interesting to note that for larger R_m, the material response can switch from cyclic softening to cyclic hardening. From Fig.3.7 one can also see that under the same strain range, the stress range decreases with the increasing R_m. This can be attributed to the fact that the proportion of viscous strain increment in the total strain increment becomes larger at the higher stress level.

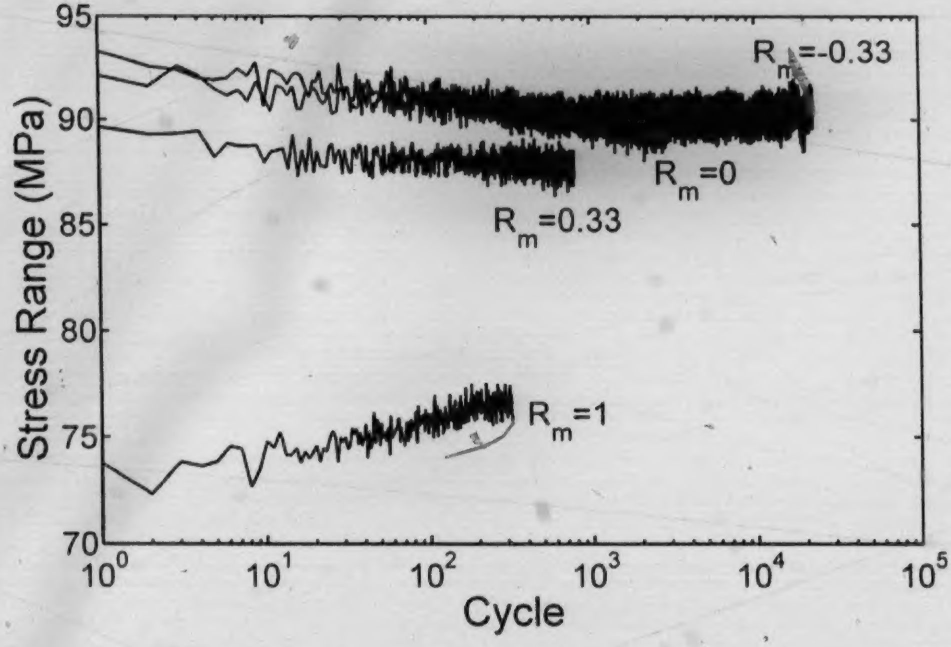

Fig. 3.7 Evolutions of stress ranges during the entire fatigue life period under the same strain amplitude but with different mean strain ratios.

The evolutions of the modulus for the four tests are plotted in Fig.3.8. No evident difference can be seen for the effect of R_m on the modulus drop. The evolutions of nonlinear strain range $\Delta\varepsilon^{nl}$ of each test are plotted in Fig.3.9. All four tests show a decreasing trend of the nonlinear strain range; however, the change is more drastic with the higher values of R_m. This can again be explained by the fact that the nonlinear stress-strain relationship becomes more dominant at higher strain level for the test with larger R_m. A systematic investigation of mean strain effect on fatigue life of this epoxy material will be presented in the next section. The above observed phenomena related to the mean strain effect have been confirmed.

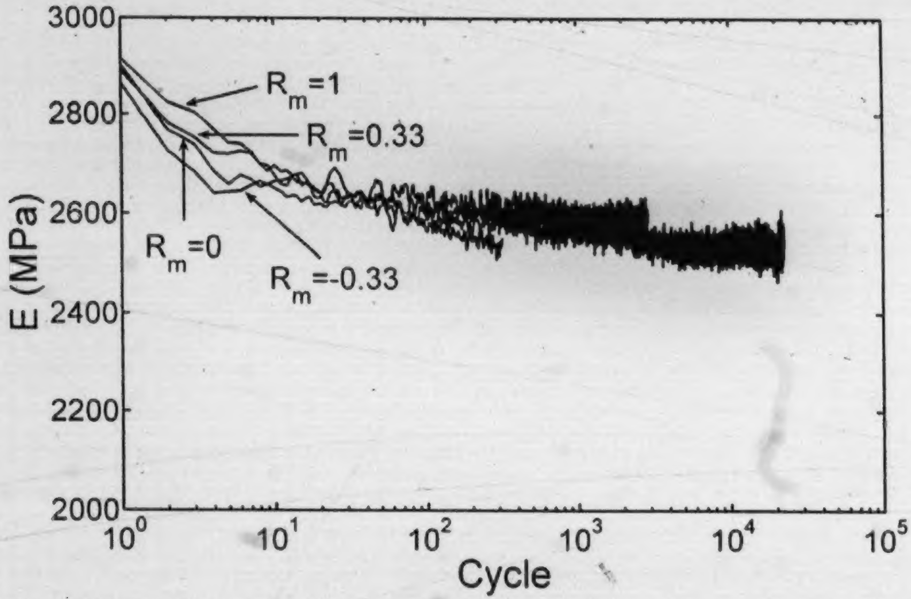

Fig. 3.8 Evolutions of modulus during the entire fatigue life period under the same strain amplitude but with different mean strain ratios.

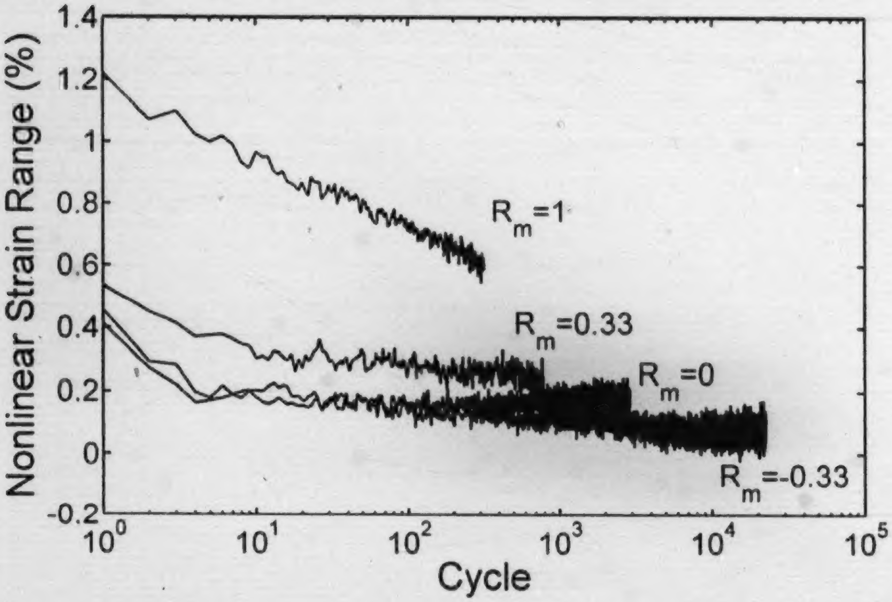

Fig. 3.9 Evolutions of nonlinear strain ranges during the entire fatigue life period under the same strain amplitude but with different mean strain ratios.

3.2.4 Fatigue mechanism of the epoxy polymer

The above observed evolution rules of the macro-mechanical parameters during the fatigue process might be related to the following micro-mechanisms: the epoxy polymer molecules in its cross-link structure might become more and more ordered and aligned along the direction of tensile stress under uniaxial cyclic loading as schematically shown in Fig.3.10. Some molecule chains may fracture during the alignment procedure and such degradation will directly be reflected in the modulus drop. Such alignment will also reduce the sliding movement between molecules and lead to the decrease of viscous flow. This will result in a decrease of nonlinear strain range.

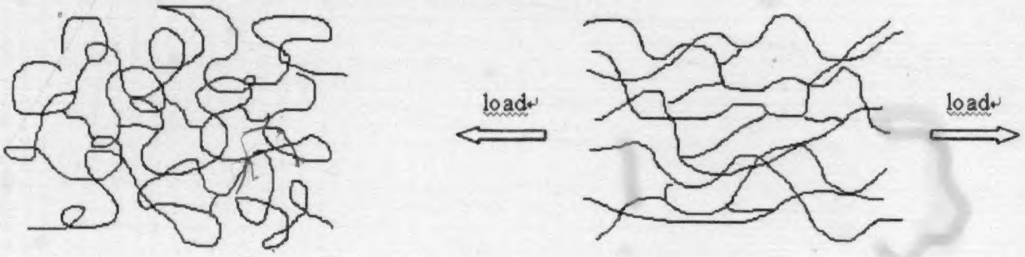

(a) (b)

Fig. 3.10 A schematic model of epoxy molecules

(a) before cyclic loading; (b) after cycle loading.

Modulus drop can lead to a decrease of stress range, i.e. cyclic softening, while decrease of nonlinearity of stress-strain relation can result in an increase of stress range, i.e. cyclic hardening. The observed behaviors of the specimens depend on a combined effect of these two factors. From the former results, at $R_m = 1$, the decrease in nonlinearity was more dominant than the modulus drop, so the cyclic hardening phenomenon was observed. Whereas for $R_m = 0$ and ± 0.33, the modulus drop was more severe than the decrease in nonlinearity and thus resulted in the cyclic softening. The above deliberations on the possible micro-mechanisms for the observed evolutions of macro-mechanical properties of the epoxy polymer need to be verified by more delicately designed experiments and observations.

3.2.5 Fractographic analysis

Fracture surface of each specimen was observed under the microscope. Fig.3.11 clearly shows that three zones exist within the fracture surface: crack initiation, stable crack propagation and final failure with most cracks initiating from the surface of the specimen. This might be attributed to less constraint near the surface of the specimen and therefore the crack may initiate more easily there. However, for two specimens with relatively small strain amplitude $\varepsilon_a = 1.64\%$ and $R_m = 0$, $\varepsilon_a = 1.82\%$ and $R_m = -0.33$, the cracks initiated from inside. Fig.3.12 clearly shows a circular shaped inner stable fatigue crack propagation zone. It might be explained that with decreasing strain amplitude the factor of less constraint at the surface becomes less critical than the factor of inherent inside defect. Hence the crack may initiate from the inside of the specimen. The comparable probability of initiation of crack from inside and outside at low level of strain amplitude also indicates that the specimen surface roughness condition with the current polishing procedure is suitable for the fatigue tests.

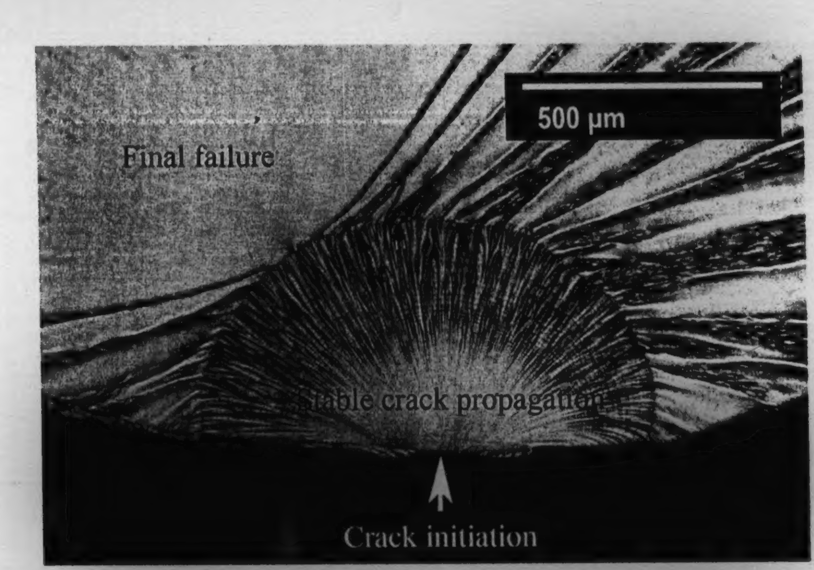
500 µm
Final failure
Stable crack propagation
Crack initiation

Fig. 3.11 Fracture surface of the fatigue crack initiated from the specimen surface.

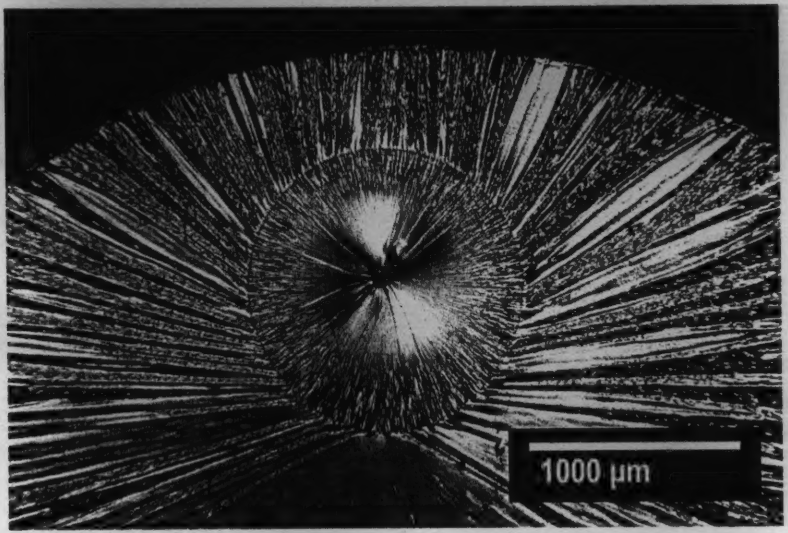

Fig. 3.12 Fracture surface of the fatigue crack initiated from the inside of the specimen.

Striations perpendicular to the crack propagation direction can be clearly observed in the stable crack propagation zone as shown in Fig.3.11 and Fig.3.12. Such striations were observed on fatigue fracture surface of other polymers and regarded as marks of crack opening and closure during each cycle. Ishiyama et al. (2001) conducted an in-situ observation of the fatigue crack propagation in PMMA. They concluded that successive ridges and valleys were formed from fractured fibrils during loading and unloading procedures, respectively. The valleys between successive ridges corresponded to the striations. Fig.3.13 shows the surface at fatigue crack propagation zone of the current epoxy polymer specimen. It also displays a similar profile to the one described in Ishiyama et al.'s work, although they are two different types of polymers. With the increase of R_m, crack closure effect is reduced and the height difference between ridges and valleys becomes smaller. Thus the striations are less visible, as shown in Fig.3.14. This picture was taken from the fractured specimen under test condition of $\Delta\varepsilon_a = 1.11\%$ and $R_m = 2$.

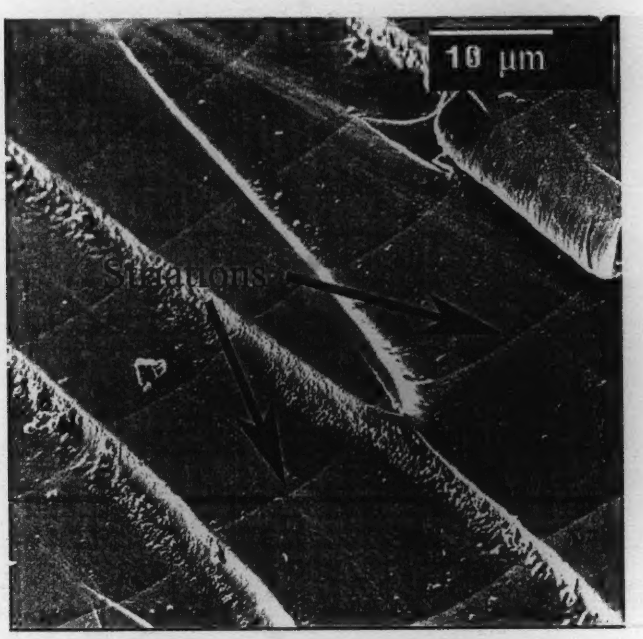

Fig. 3.13 Striations in the stable fatigue crack propagation zone taken by SEM.

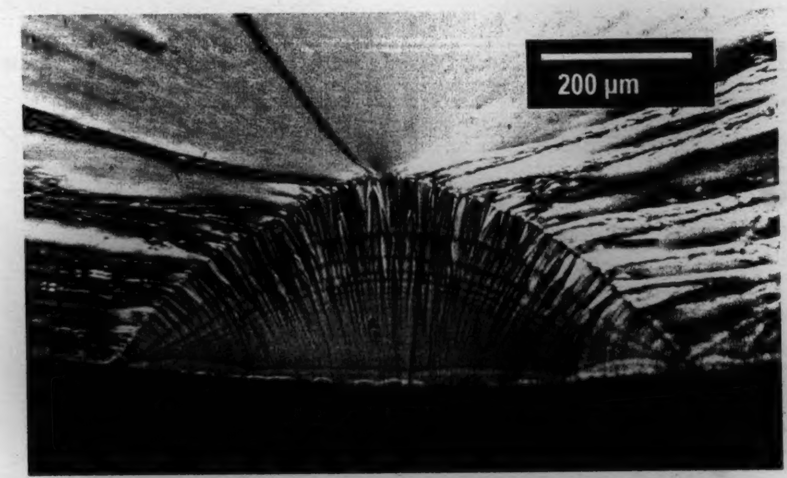

Fig. 3.14 Fracture surface of the fatigue crack under tension-tension cyclic loading condition.

3.3 Mean stress/strain effect

3.3.1 Overview of mean stress/strain effect

Mean stress effect on fatigue life of metal materials has been extensively investigated and reported (Fang et al., 1994, Koh et al., 1999, Strizak et al., 2003, McClaflin et al., 2004). However, for polymer materials, studies on mean stress/strain effect on their fatigue lives are much less. J. A. Sauer et al. (1976) performed fatigue tests with mean stress on polystyrene, and a modified Goodman relation with consideration of rupture strength was proposed. T. R. Clark et al. (1993) conducted series of experiments and analyses to illustrate the effect of molecular weight and mean stress on the fatigue mechanisms of PMMA. As presented in previous section (Table 3.1), the mean stress would significantly influence the fatigue life of the epoxy polymer. Therefore, further investigations are necessary in order to develop or improve fatigue theory of polymer materials with consideration of mean stress/strain effect.

For metals and alloys, various criteria have been proposed to deal with the mean stress effect on fatigue life, such as well-known Soderberg's diagram (1930), Goodman's diagram (1899), Gerber's diagram (1874), Morrow's diagram (1965) and Smith-Watson-Topper (SWT) parameter (Smith et al., 1970). Further investigation of these criteria was conducted by Kujawski et al. (1995), where mean stress function in a power law form was proposed and it was demonstrated to unify the above various criteria. An exponential mean stress function was suggested by S. Kwofie (2001) to relate the mean stress effect to the fatigue strength and life. He also showed that some previous criteria can be seen as particular cases of this mean stress function. In this section, the power law mean stress function in (Kujawski et al., 1995) has been adopted and extended to low cycle fatigue life prediction for epoxy polymer material.

Previous studies (Shen et al., 2004, Xia et al., 2005) have shown that due to the viscoelastic behavior of polymer materials, considerable ratcheting strain could be accumulated in stress-controlled fatigue/cyclic tests. Such ratcheting strain is expected to be detrimental to the fatigue life according to former investigation on metal materials, especially at high mean stress levels and low cycle fatigue regime (Xia et al., 1996). To eliminate the ratcheting strain effect strain-controlled fatigue test would be appropriate.

Although distinct mean stress relaxation would occur in strain-controlled fatigue tests, it was found that the mean stress would reach a saturated level in relatively short period and hold stable during the most of remaining life. However, strain-controlled fatigue tests for polymer materials used to be difficult since most contact strain measurement methods are not suitable for fatigue tests of such soft materials. The non-contact strain measurement system was then employed to perform all the strain-range-controlled fatigue tests. Mean stress/strain effect on the fatigue life was characterized by calibrating the mean stress/strain function in either stress, strain or energy approach, respectively. Good agreements between experimental data and predictions can be seen in either the strain, stress or energy approaches.

3.3.2 Experimental procedure

All the fatigue tests were performed under strain-range-controlled mode with 4 different mean strain ratios R_m, Eq.(3.8). The test parameters and resulted fatigue lives of all tests are summarized in Table 3.2. The loading rate was kept 10MPa/s for each test and all the tests were carried out under room temperature and laboratory environment. Among these, the fully-reversed tests results were taken from Section 3.2 for a comparison. It is worth to be mentioned that even though $\varepsilon_m = 0$ in the fully-reversed strain-range-controlled fatigue tests, $\sigma_m \neq 0$ because of the anisotropic behavior of this material in tension and compression. However, such small mean stress ratio (σ_m/σ_a) is not expected to significantly affect the fatigue life. Thus, in this paper, it is assumed that $\sigma_m/\sigma_a = 0$ for all the fully-reversed tests. One may also notice that the mean strain ratio in the same group may not be exactly identical. This is due to the overshooting of the test machine which will lead to small fluctuation of strain range resulted from short delay time of image processing as describe in Chapter 2. Strain amplitude vs. fatigue life data of all the tests with 4 levels of mean strain ratios were plotted in Fig.3.15. Typical stress-strain loops of the first 5 cycles, the mid-life cycle and the last cycle of two tests, S20 and S30, are shown in Fig.3.16, where the evolution of mean stress relaxation, shape change of hysteresis loops etc. can be observed.

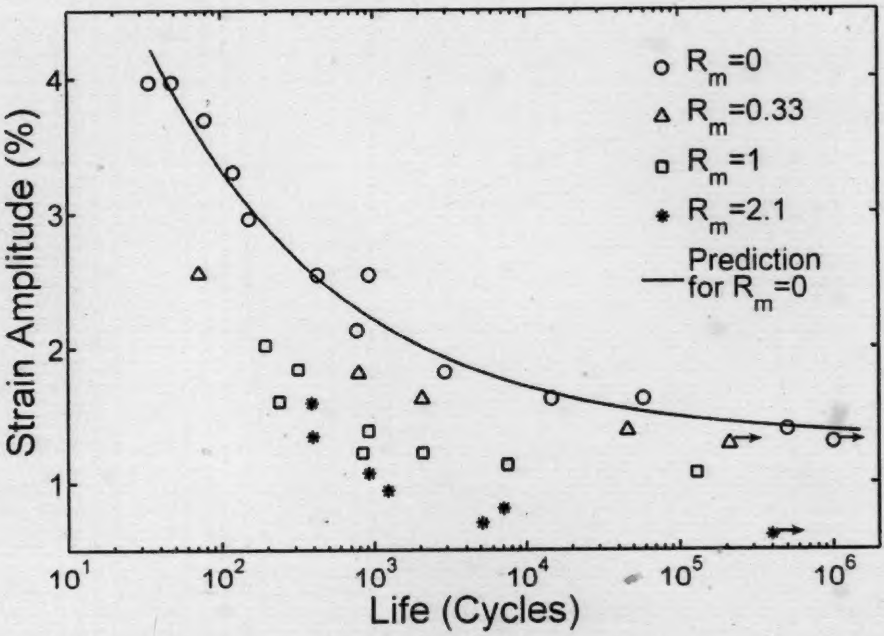

Fig. 3.15 Strain amplitude vs. fatigue life of uniaxial fatigue tests with 4 different mean strain ratios.

Table 3.2 Parameters and results of uniaxial fatigue tests with mean strains

No.	Group No.	ε_a (%)	ε_m (%)	σ_a (MPa)	σ_m (MPa)	R_m	ΔW^d_{avg} (kJ/ m^3)	ΔW^e_{avg} (kJ/ m^3)	*N (cycles)*
S1	1	3.97	0	76.11	-6.22	0	692.01	1602.1	34
S2	1	3.97	0	75.74	-6.04	0	720.67	1566.3	48
S3	1	3.69	0	74.10	-5.40	0	490.33	1443.9	78
S4	1	3.31	0	70.76	-5.22	0	349.79	1243.8	120
S5	1	2.96	0	66.22	-4.08	0	273.40	1038.2	152
S6	1	2.55	0	59.45	-3.41	0	165.40	792.9	424
S7	1	2.55	0	57.77	-3.38	0	170.39	769.8	925
S8	1	2.13	0	52.59	-2.42	0	97.71	581.7	769
S9	1	1.82	0	45.00	-2.24	0	70.96	424.7	2910
S10	1	1.62	0	41.06	-1.53	0	51.46	342.7	14618
S11	1	1.62	0	41.06	-1.53	0	51.46	342.7	57933
S12	1	1.39	0	36.00	0	0	34.58	266.5	500000
S13	1	1.30	0	35.00	0	0	30.00	255.0	>1000000
S14	2	2.56	0.89	55.71	10.98	0.35	198.97	799.4	71
S15	2	1.81	0.63	43.93	10.58	0.35	71.68	429.5	787
S16	2	1.62	0.54	40.76	8.94	0.33	50.99	353.7	2057
S17	2	1.38	0.44	35.56	7.31	0.32	33.10	254.4	45713
S18	2	1.28	0.43	33.47	7.00	0.34	25.81	221.3	>210000
S19	3	2.02	2.01	39.67	30.86	1.00	174.35	423.3	193
S20	3	1.84	1.83	37.98	29.46	1.00	128.99	370.0	318
S21	3	1.60	1.60	35.10	28.60	1.00	70.14	304.5	239
S22	3	1.38	1.38	31.59	25.10	1.00	52.44	229.4	913
S23	3	1.22	1.22	28.91	22.91	1.00	35.71	185.2	2080
S24	3	1.22	1.20	28.84	24.02	0.98	34.61	182.0	838
S25	3	1.13	1.12	27.68	22.00	0.99	24.81	163.5	7515
S26	3	1.07	1.07	26.75	19.70	1.00	18.67	143.1	129060
S27	4	1.59	3.56	31.36	39.32	2.24	116.98	245.8	388
S28	4	1.34	2.84	27.20	43.43	2.12	72.05	184.2	395
S29	4	1.07	2.22	23.64	39.52	2.07	35.87	129.4	921
S30	4	0.94	1.97	21.41	37.64	2.10	23.72	102.7	1229
S31	4	0.81	1.74	19.61	34.07	2.15	14.81	81.4	7079
S32	4	0.70	1.43	17.38	30.23	2.04	10.32	61.2	5115
S33	4	0.61	1.25	16.11	24.50	2.05	6.55	49.0	>400000

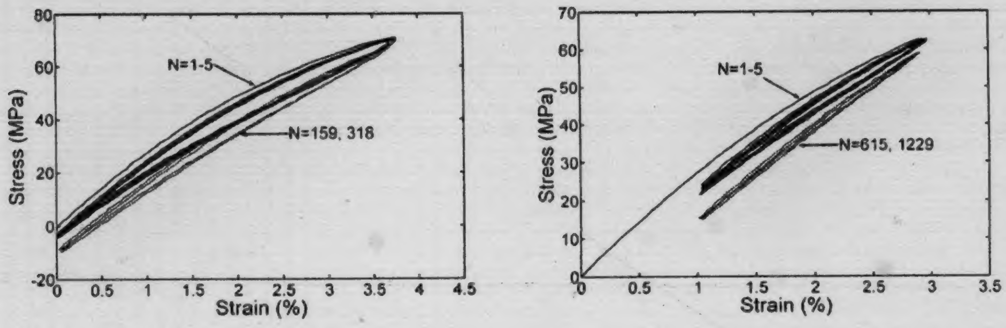

(a) (b)

Fig. 3.16 Evolution of stress-strain loops of fatigue tests: (a). Test S20; (b) Test S30.

3.3.3 Evolution of mechanical properties

Quantitative analysis of the mechanical parameters, such as stress range, mean stress and strain energy density, was carried out based on the stress-strain data.

- **Stress range evolution**

Figure 3.17 shows the evolution of the stress range of all tests with different mean strain ratios.

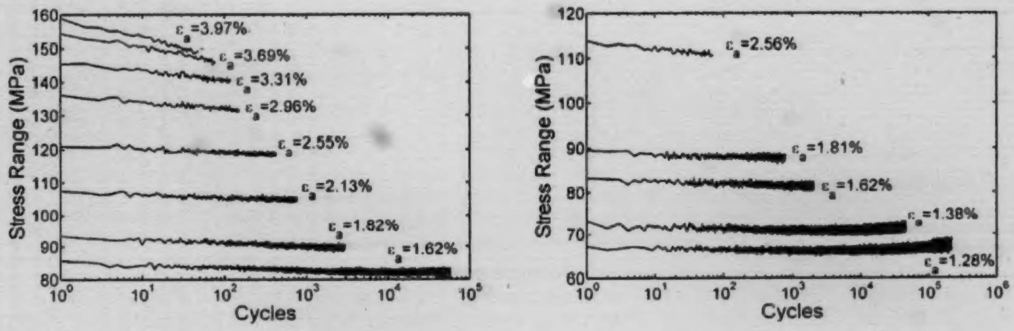

(a) (b)

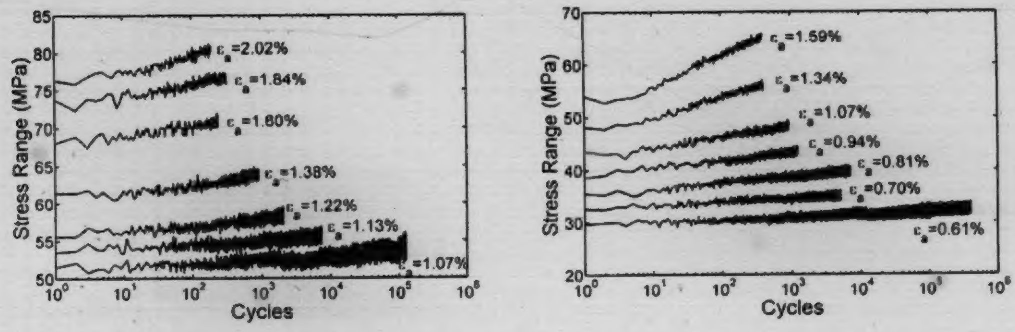

(c) (d)

Fig. 3.17 Stress range evolution of all strain-range-controlled uniaxial fatigue tests with 4 different mean strain ratios: (a) $R_m = 0$; (b) $R_m = 0.33$; (c) $R_m = 1$; (d) $R_m = 2.1$.

Equation (3.2) was chosen to fit the stress range data. As discussed in previous section, due to the modulus degradation and decrease of nonlinearity in stress-strain relationship of the specimen during cyclic loading process, either cyclic softening or cyclic hardening could occur at different mean strain ratios. It depends on the competition of the above two factors, where modulus degradation would lead to cyclic softening while decrease of nonlinearity of stress-strain relationship could cause cyclic hardening. Evolution coefficients of all the tests are plotted in Fig.3.18, where cyclic softening can be observed at $R_m = 0$ and $R_m = 0.33$ (α <0), while cyclic hardening occurred at $R_m = 1$ and $R_m = 2.1$(α >0). Moreover, at the same strain ratio, absolute value of α increases with increase of strain amplitude, which means the increase of strain softening or hardening rate.

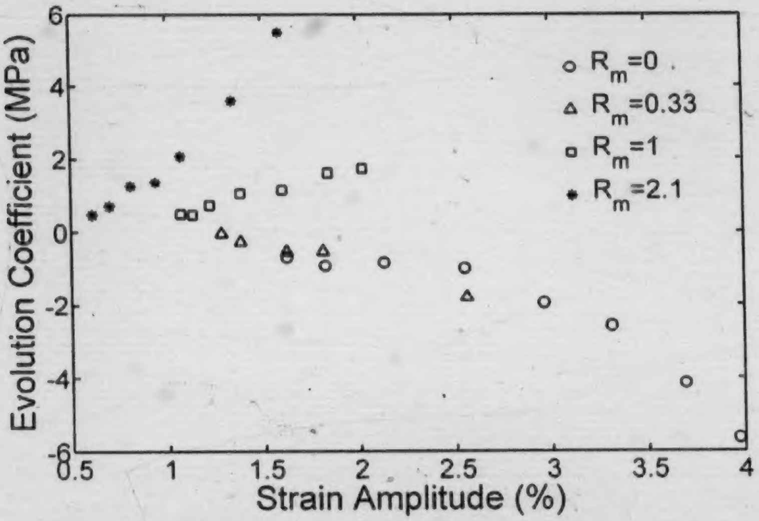

Fig. 3.18 Evolution coefficient, α, vs. strain amplitude of all the strain-range-controlled uniaxial fatigue tests with 4 different mean strain ratios.

- **Mean stress relaxation**

In the strain-range-controlled fatigue tests with mean strain, mean stress relaxation could occur during the cyclic loading process. Its value decreased quickly in the initial several cycles and then reached a relatively stable stage which occupied most time of the fatigue period. The evolutions of the mean stress of all the tests are shown in Fig.3.19.

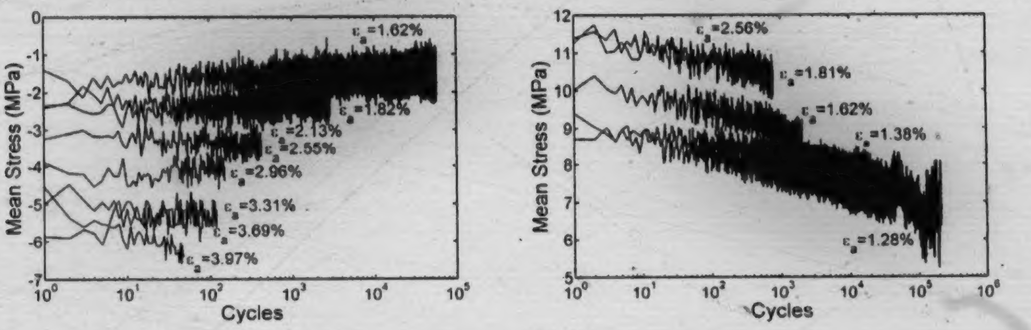

(a) (b)

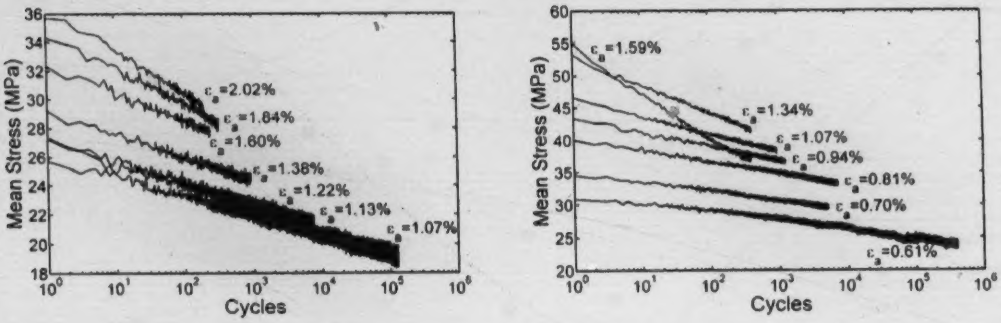

(c) (d)

Fig. 3.19 Mean stress relaxation of all the strain-range-controlled uniaxial fatigue tests with 4 different mean strain ratios: (a) $R_m = 0$; (b) $R_m = 0.33$; (c) $R_m = 1$; (d) $R_m = 2.1$.

It seems that a linear relationship can be fit in the semi-log scale with respect to fatigue life. It is noted that although a linear decreasing trend is noticed in the semi-log scale, the actual mean stress relaxation rate during the later stage of fatigue life is much slower than the initial stage, which can also be observed from Fig.3.16. Therefore, the mean stress level can be approximately considered as stable during the later stage of fatigue life. Similar to stress range evolution Eq.(3.2), a logarithm function was chosen to fit the mean stress data.

$$\sigma_m = \sigma_{mo} + \beta \cdot \log N \qquad (3.9)$$

where β is defined as the relaxation coefficient, σ_{mo} is the mean stress in the first cycle and N is the number of cycles. Also to be noted that σ_{mo} and β are dependent on strain range. Relaxation coefficients of all the tests are plotted in Fig.3.20, where one can see the increase of relaxation rate with increase of R_m or strain amplitude. The mean stress relaxation rate is much faster at $R_m = 1$ and $R_m = 2.1$ than at $R_m = 0.33$. However, no mean stress relaxation can be observed at $R_m = 0$.

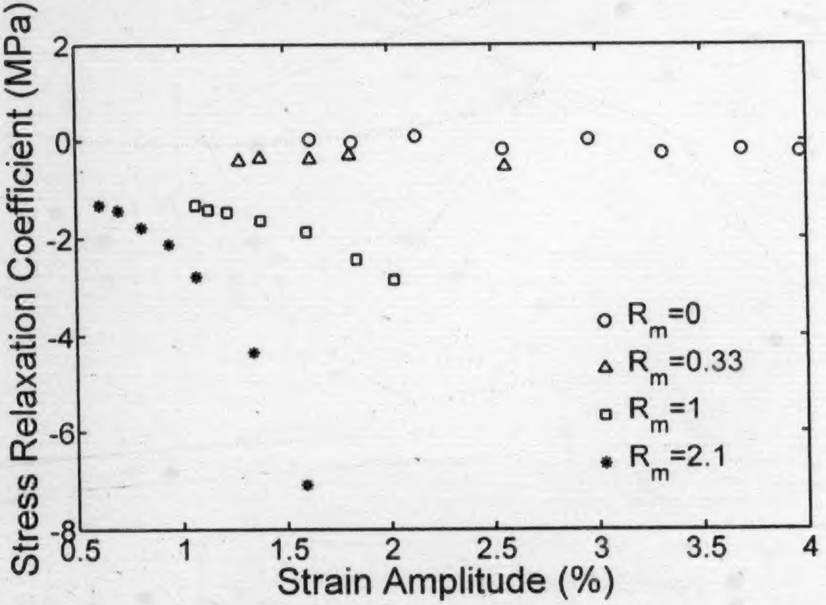

Fig. 3.20 Stress relaxation coefficient, β, vs. strain amplitude of all the strain-range-controlled uniaxial fatigue tests with 4 different mean strain ratios.

- **Dissipated Strain Energy Density (DSED) and Elastic Strain Energy Density Amplitude (ESEDA)**

Due to viscoelastic nature of the epoxy polymer materials, certain amount of irreversible strain energy was dissipated during the cyclic loading process, which was converted to heat dissipation or to cause damage. Therefore, precise measurement of the dissipated strain energy density (DSED) is important for evaluating the degree of damage during the cyclic loading in the fatigue process. Based on the recorded stress-strain data of the tests, DSED can be calculated by integrating the area of the hysteresis loop of each cycle, shown as ΔW^d in Fig.1.16. The evolution of ΔW^d of each test was plotted in Fig.3.21. An decreasing trend can be observed at $R_m = 1$ and $R_m = 2.1$, and a increasing trend can be seen at $R_m = 0$. While at $R_m = 0.33$, ΔW^d keeps almost constant during the entire test period. Moreover, the decreasing or increasing rate of ΔW^d increases with increase of strain amplitude. Number average value of ΔW^d for all the cycles in each test, denoted by ΔW^d_{avg}, was chosen as the representative parameter of DSED in this study. The ΔW^d_{avg} vs. strain amplitude for all the tests with different strain ratios are shown in Fig.3.22, where it can be noticed that at the same mean strain ratio, ΔW^d_{avg} increases rapidly with the increase of strain amplitude. One can also see that for the same strain amplitude, ΔW^d_{avg} increases with increase of mean strain ratio. These could be attributed to the nonlinear stress-strain effect of such epoxy polymer material at higher strain level. It was found that ΔW^d_{avg} is generally fairly close to ΔW^d at the mid-life cycle, which was commonly used in fatigue theories for metals and alloys.

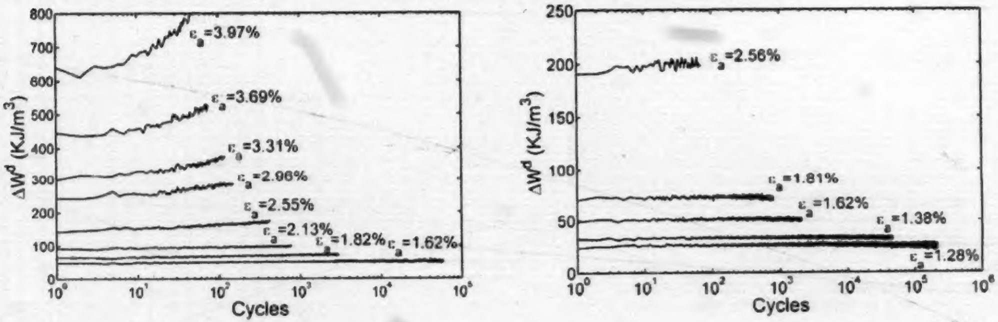

(a) (b)

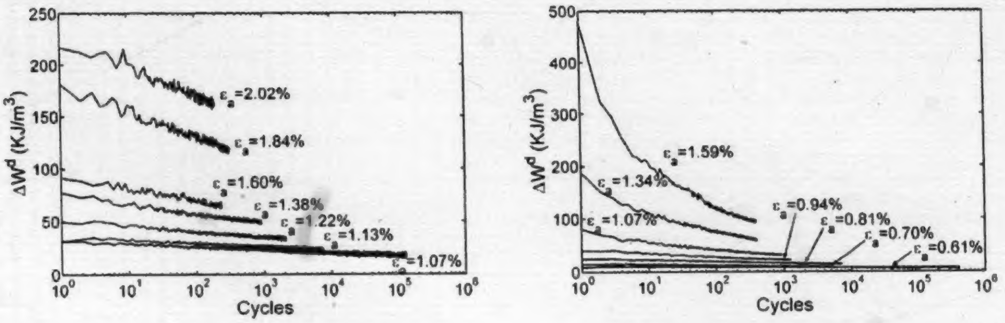

(c) (d)

Fig. 3.21 Evolution of dissipated strain energy density of all the strain-range-controlled uniaxial fatigue tests with 4 different mean strain ratios: (a) $R_m = 0$; (b) $R_m = 0.33$; (c) $R_m = 1$; (d) $R_m = 2.1$.

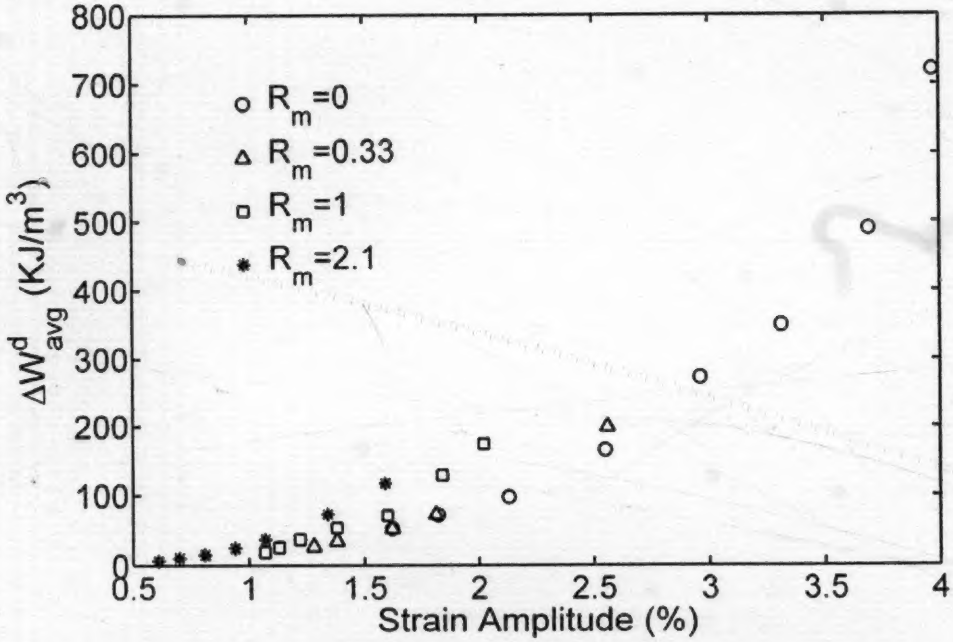

Fig. 3.22 Dissipated strain energy density vs. strain amplitude of all the strain-range-controlled uniaxial fatigue tests with 4 different mean strain ratios.

In addition to ΔW^d, elastic strain energy density amplitude (ESEDA) ΔW^e, defined as the area under the hysteresis loop and above the mean stress level as illustrated in Fig.1.16, is also considered to contribute to the fatigue damage in each cycle. The calculated ΔW^e of each cycle for all the tests is plotted in Fig.3.23.

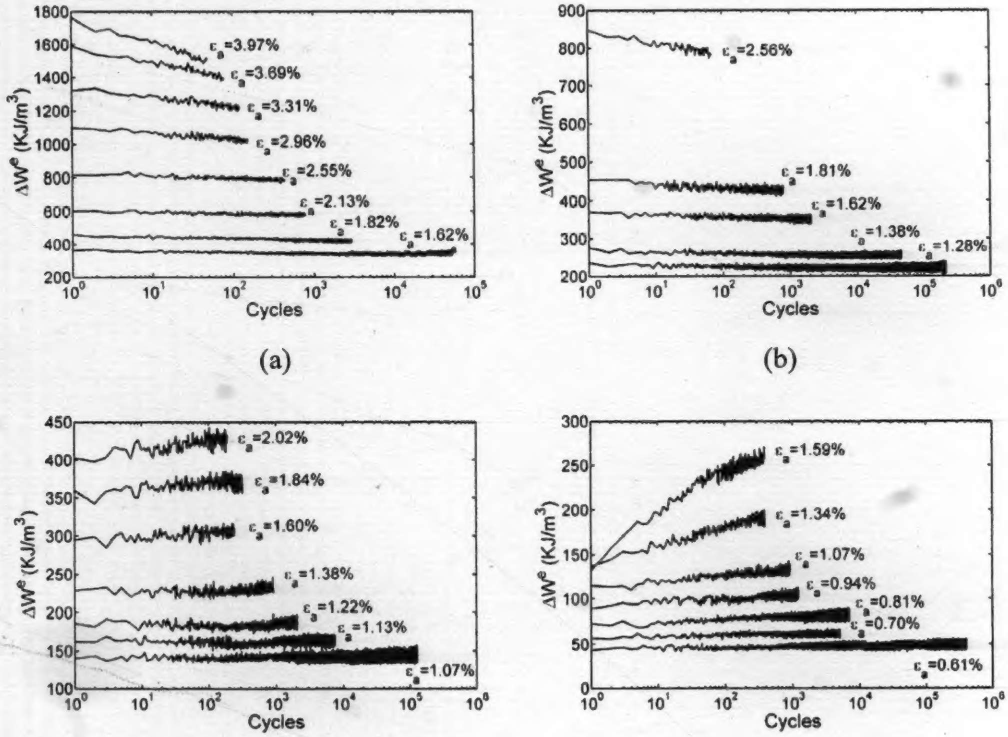

(a) (b)

(c) (d)

Fig. 3.23 Evolution of elastic strain energy density amplitude of all the strain-range-controlled uniaxial fatigue tests with 4 different mean strain ratios: (a) $R_m = 0$; (b) $R_m = 0.33$; (c) $R_m = 1$; (d) $R_m = 2.1$.

At lower mean strain ratios, e.g. $R_m = 0$ and $R_m = 0.33$, ΔW^e keeps almost constant during the test period. While at higher mean strain ratios, e.g. $R_m = 1$ and $R_m = 2.1$, an increasing trend of ΔW^e can be observed and the increasing rate is higher at higher strain amplitude. Similar to ΔW^d_{avg}, averaged value ΔW^e_{avg} is also considered as the measure of ΔW^e for each test. The ΔW^e_{avg} vs. strain amplitude for each test is plotted in Fig.3.24. It can be seen that the values of ΔW^e_{avg} at high R_m are slightly lower than those at low R_m. This could be due to the nonlinearity of stress-strain relationship at higher strain level.

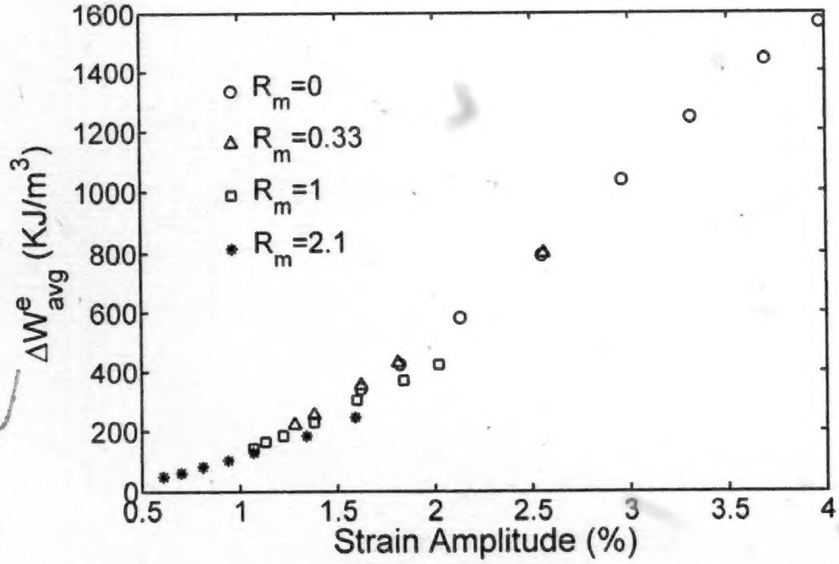

Fig. 3.24 Elastic strain energy density amplitude vs. strain amplitude of all the strain-range-controlled uniaxial fatigue tests with 4 different mean strain ratios.

3.3.4 Mean stress/strain functions

In phenomenological approach of fatigue life prediction, most efforts have been focused on searching an appropriate damage parameter where best correlation can be obtained with respect to fatigue lives. The relationship between damage parameter and fatigue life can be commonly expressed as:

$$\psi = \kappa \cdot (N_f)^{\gamma} + \psi_0 \tag{3.10}$$

where ψ is the damage parameter, N_f is the fatigue life represented by total number of cycles to failure, κ and γ are material constants, ψ_0 is the fatigue limit. Generally, the phenomenological fatigue theories can be classified into three categories, stress-based, strain-based and energy-based approaches, depending on the kind of chosen damage parameter which can be the function of stress, strain or strain energy density. To consider the mean stress/strain effect, it is common that an additional mean stress/strain function is introduced and embedded into the damage parameters in these three approaches.

A simple power law form of mean stress function proposed in (Kujawski et al., 1995) is defined as:

$$f\left(\frac{\sigma_m}{\sigma_a}\right) = \left(1 + \eta \frac{\sigma_m}{\sigma_a}\right)^n \tag{3.11}$$

Similarly, the mean strain function can be defined as:

$$f\left(\frac{\varepsilon_m}{\varepsilon_a}\right) = \left(1 + \eta \frac{\varepsilon_m}{\varepsilon_a}\right)^n \tag{3.12}$$

where η and n are material constants. Incorporating the mean stress function, equivalent damage parameters ψ are defined as:

strain approach $$\varepsilon_{eq} = \left(1 + \eta \frac{\varepsilon_m}{\varepsilon_a}\right)^n \varepsilon_a \tag{3.13}$$

stress approach $$\sigma_{eq} = \left(1 + \eta \frac{\sigma_m}{\sigma_a}\right)^n \sigma_a \tag{3.14}$$

energy approach $$\Delta W_{eq} = \Delta W^{d}_{avg} + \left(1+\eta\frac{\sigma_m}{\sigma_a}\right)^{n}\Delta W^{e}_{avg} \qquad (3.15)$$

Note in strain approach, a mean strain function $f\left(\frac{\varepsilon_m}{\varepsilon_a}\right)$ is appropriate. For fully-reversed fatigue tests, $\varepsilon_m = 0$ and $\sigma_m = 0$. Thus, Eqs.(3.13)-(3.15) will be $\varepsilon_{eq} = \varepsilon_{-1}$, $\sigma_{eq} = \sigma_{-1}$ and $\Delta W_{eq} = \Delta W^{d}_{-1avg} + \Delta W^{e}_{-1avg}$, respectively, where subscript -1 represents fully-reversed tests. Therefore, in the case of strain approach or stress approach, the equivalent damage parameter can be understood as the strain amplitude or stress amplitude in a fully-reversed fatigue test, which has the same fatigue life as the test with the mean strain or mean stress. We replace ε_{eq} and σ_{eq} with ε_{-1} and σ_{-1}, respectively, as these notations were commonly used in the previous references (Soderberg, 1930, Goodman, 1899, Gerber, 1874, Morrow, 1965). Then Eq.(3.14) can be written as

$$\left(1+\eta\frac{(\sigma_m/\sigma_{-1})}{(\sigma_a/\sigma_{-1})}\right)^{n}\frac{\sigma_a}{\sigma_{-1}} = 1 \qquad (3.16)$$

The relation of $\frac{\sigma_a}{\sigma_{-1}}$ and $\frac{\sigma_m}{\sigma_{-1}}$ was plotted with different material constants, n and η in Fig.3.25. For the limiting case of $\frac{\sigma_a}{\sigma_{-1}} \to 0$, one can see that $\frac{\sigma_m}{\sigma_{-1}} \to 0$ for $n > 1$ and $\frac{\sigma_m}{\sigma_{-1}} \to \infty$ for $0 < n < 1$. Neither of these two trends seems physically meaningful. When the stress amplitude, σ_a, approaches zero, which means a nearly static loading condition, the σ_m should be related to certain static strength of materials, i.e. $\frac{\sigma_m}{\sigma_{-1}}$ should approach a finite value. Therefore, in the current study, only value $n = 1$ is adopted.

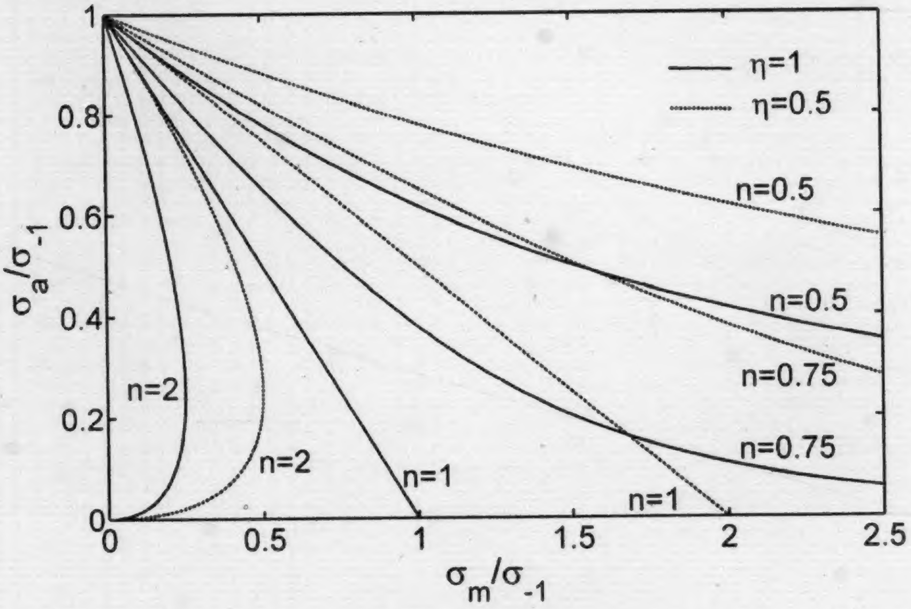

Fig. 3.25 Mean stress function with different values of material constants

Further calculations have also confirmed that no improvement in fitting could be seen while the values $n \neq 1$ were considered for the current experimental data. Thus, Eq. (3.16) can be written as:

$$\frac{\sigma_a}{\sigma_{-1}} + \eta \frac{\sigma_m}{\sigma_{-1}} = 1 \tag{3.17}$$

Eq. (3.17) can be further written in a unified expression:

$$\frac{\sigma_a}{\sigma_{-1}} + \frac{\sigma_m}{\sigma_r} = 1 \tag{3.18}$$

where $\sigma_r = \frac{\sigma_{-1}}{\eta}$ is the reference stress. In Soderberg, Goodman or Morrow's relations, σ_r is taken as σ_y, σ_u and $\sigma_f^{'}$, which is yield stress, ultimate strength and fatigue strength coefficient, respectively. However, to extend Eq.(3.18) to intermediate and low cycle fatigue of polymer materials, σ_r should be a function of σ_{-1} as observed in our experiments. This is coincident with suggestion by Sauer et al. (1976) that time-dependent creep rupture strength should be utilized as the reference stress parameter. Mallick (2004) also proposed a creep rupture strength as the reference stress for the mean stress effect on the fatigue behavior of a fiber reinforced polymeric composite material. In our case, η is taken to be a constant. Thus it is implicitly assumed that σ_r is a linear function of σ_{-1}.

Material constants in Eq.(3.10) can be obtained from fully-reversed fatigue tests. Afterward, mean stress/strain function is able to be calibrated by fatigue tests results with different mean stress/strain ratios.

3.3.5 Fatigue life prediction with three approaches

- **Strain Amplitude Approach**

No mean strain effect exists in the fully-reversed fatigue tests, where the master strain amplitude vs. fatigue life curve can be obtained from Eq.(3.1):

$$\varepsilon_{eq} = \varepsilon_{-1} = 0.1 \cdot N_f^{-0.347} + 1.3\% \tag{3.19}$$

For the tests with mean strain, substitute fatigue life into right hand side of Eq.(3.19) and the equivalent strain amplitude ε_{eq} can be obtained. Thus, from Eq.(3.13), one can obtain:

$$\frac{\varepsilon_a}{\varepsilon_{eq}} = \frac{1}{f\left(\frac{\varepsilon_m}{\varepsilon_a}\right)} \tag{3.20}$$

For all the fatigue tests, $\varepsilon_a/\varepsilon_{eq}$ vs. $\varepsilon_m/\varepsilon_a$ were obtained and plotted in Fig.3.26. The ratio between ε_a and ε_{eq} reflects the severity of R_m on the fatigue life. It can be observed that with the increase of R_m, ε_a decreases in order to reach the same fatigue life as fully-reversed test with strain amplitude of ε_{eq}. The mean strain function was then calibrated by best fit technique:

$$f\left(\frac{\varepsilon_m}{\varepsilon_a}\right) = 1 + 0.55\frac{\varepsilon_m}{\varepsilon_a} \tag{3.21}$$

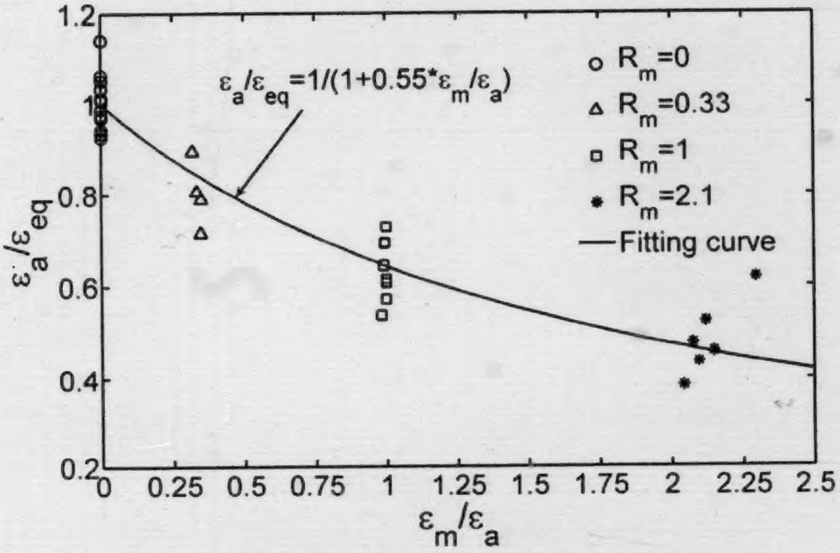

Fig. 3.26 Mean strain function for strain approach

Thus, fatigue life prediction with mean strain effect in strain approach for this epoxy material can be obtained as:

$$\left(1+0.55\frac{\varepsilon_m}{\varepsilon_a}\right)\varepsilon_a = 0.1\cdot N_f^{-0.347} + 1.3\% \tag{3.22}$$

The experimental data of equivalent strain amplitude vs. fatigue life and prediction curve are plotted in Fig.3.27, where good agreement can be seen.

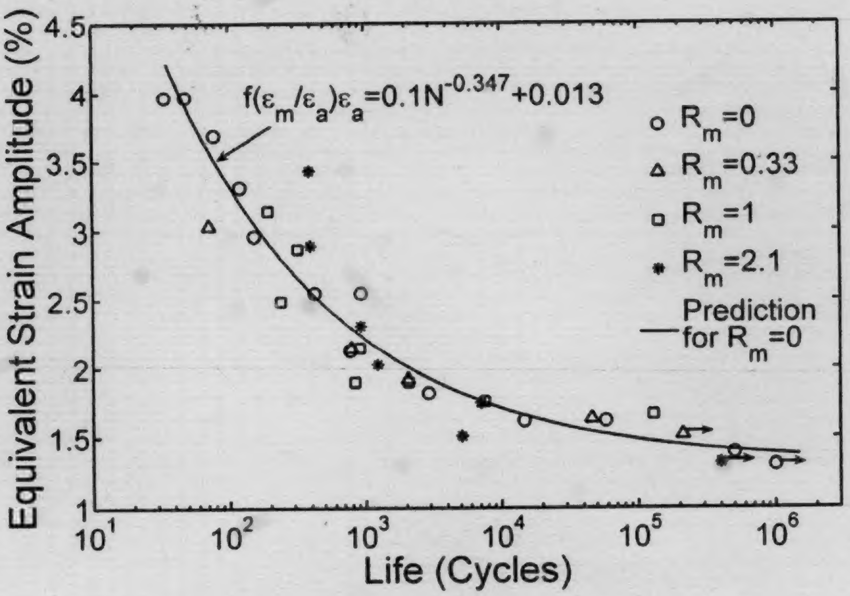

Fig. 3.27 Equivalent strain amplitude vs. fatigue life

The following cross correlation coefficient can be used to quantitatively evaluate the performance of prediction:

$$C=\frac{\sum_i\left(A_i-\overline{A}\right)\left(B_i-\overline{B}\right)}{\sqrt{\left(\sum_i\left(A_i-\overline{A}\right)^2\right)\left(\sum_i\left(B_i-\overline{B}\right)^2\right)}} \tag{3.23}$$

where A and B are two arrays with the same length, $\overline{A}$ and $\overline{B}$ are mean values of these two arrays, respectively. Taking array A as the experimental values of the equivalent damage parameter (individual points in Fig.3.27) and array B as the corresponding values on the predictive curve which has the same N_f, the cross correlation coefficient was calculated to be 0.9443.

- **Stress Amplitude Approach**

It has been found that in the low cycle fatigue regime of ductile metal materials, introducion of mean strain usually does not appreciably affect the fatigue life because of the mean stress relaxation caused by plastic deformation during the early life. However, in the strain-range-controlled fatigue tests of this epoxy polymer material, although mean stress relaxation occurred, it reached a stable stage which kept a certain level during the rest of fatigue life period in both low cycle and high cycle regimes. Such mean stress is expected to have considerable effect on the fatigue life. Therefore, mean stress effect should be included into fatigue life prediction and stress approach seems to be more appropriate than the strain approach where mean stress relaxation has been omitted.

Usually stress amplitude and mean stress are not constant in strain-controlled or strain-range-controlled fatigue tests. Traditionally, in fatigue theories of metals, the values of these parameters at mid-life cycle are considered as an appropriate measure. In this paper, average values of the evolution parameters, which are comparable to the values at mid-life cycle, were considered as the measure of these parameters. All the values of these components are listed in Table 3.2. As the same manner of strain approach, master stress amplitude vs. fatigue life curve was obtained from the results of fully-reversed fatigue tests by best fit technique:

$$\sigma_{eq} = \sigma_{-1} = 192.6 \cdot N_f^{-0.362} + 35 \tag{3.24}$$

Following the same procedure in strain approach, the equivalent stress amplitude σ_{eq} can be obtained by substituting fatigue life into right hand side of Eq.(3.24). And then the ratio between σ_a and σ_{eq} can be obtained by substituting σ_{eq} into Eq.(3.14). For all the tests, σ_a/σ_{eq} vs. σ_m/σ_a were obtained and plotted in Fig.3.28. Then the mean stress function was calibrated by the best fit technique:

$$f\left(\frac{\sigma_m}{\sigma_a}\right) = 1 + 0.76\frac{\sigma_m}{\sigma_a} \tag{3.25}$$

Thus, the fatigue life prediction with mean stress effect can be expressed as:

$$\left(1 + 0.76\frac{\sigma_m}{\sigma_a}\right)\sigma_a = 192.6 \cdot N_f^{-0.362} + 35 \tag{3.26}$$

The equivalent stress amplitude vs. fatigue life data were plotted in Fig.3.29 against the prediction curve. The cross correlation coefficient between the experimental data and the prediction is 0.9526, which is a little better than the strain approach. Moreover, better prediction may be seen than the strain approach in low cycle regime. This might be due to the mean stress relaxation, which could lead to extended fatigue life.

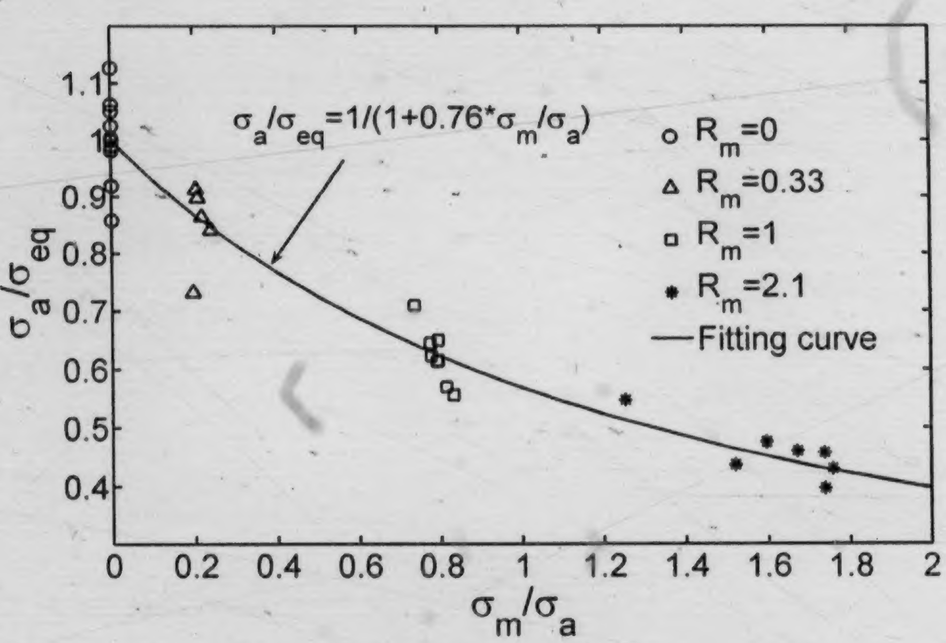

Fig. 3.28 Mean stress function for stress approach

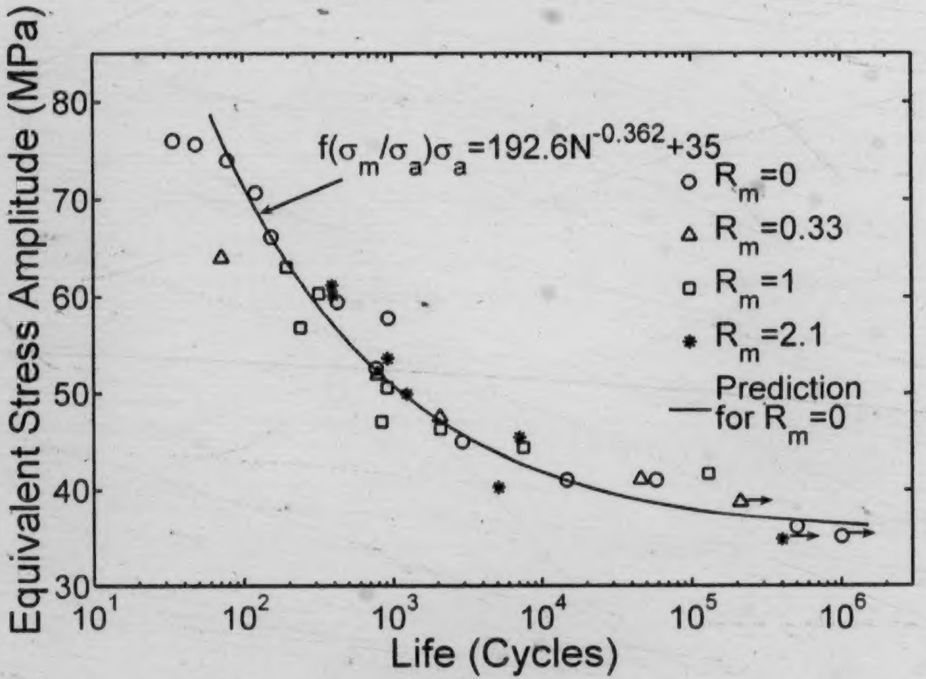

Fig. 3.29 Equivalent stress amplitude vs. fatigue life

- **Strain Energy Density Approach**

Energy approach for fatigue life prediction has been demonstrated to be appropriate to characterize the damage in each cycle of fatigue test (Ellyin, 1997). The nature of fatigue process in both macroscopic and microscopic aspect has been unified in energy approach. Moreover, the stress-strain relationship is also inherently included in energy parameters. Both ΔW^d and ΔW^e were considered to contribute to the fatigue damage in each cycle, while ΔW^e is directly related to the mean stress effect through the factor of mean stress function as shown in Eq.(3.15). For the fully-reversed fatigue tests, the master total strain energy density vs. fatigue life curved can be obtained by best fit technique:

$$\Delta W_{eq} = \Delta W^d_{avg} + \Delta W^e_{avg} = 12557 \cdot N_f^{-0.484} + 285 \tag{3.27}$$

For the tests with mean stress, substituting the fatigue life into right hand side of Eq.(3.27), ΔW_{eq} can be obtained. Then substituting ΔW_{eq} into Eq.(3.15), $\Delta W^e_{avg} / \left(\Delta W_{eq} - \Delta W^d_{avg}\right)$ vs. σ_m / σ_a of all the tests were obtained and plotted in Fig.3.30. The mean stress function was then calibrated by the best fit procedure:

$$f\left(\frac{\sigma_m}{\sigma_a}\right) = 1 + 2.35\frac{\sigma_m}{\sigma_a} \tag{3.28}$$

Then the energy approach for fatigue life prediction with mean stress effect can be expressed as:

$$\Delta W^d_{avg} + \left(1 + 2.35\frac{\sigma_m}{\sigma_a}\right)\Delta W^e_{avg} = 12557 \cdot N_f^{-0.484} + 285 \tag{3.29}$$

The total strain energy density vs. experimental fatigue life data and prediction curve are plotted in Fig.3.31, where the cross correlation coefficient is 0.9716.

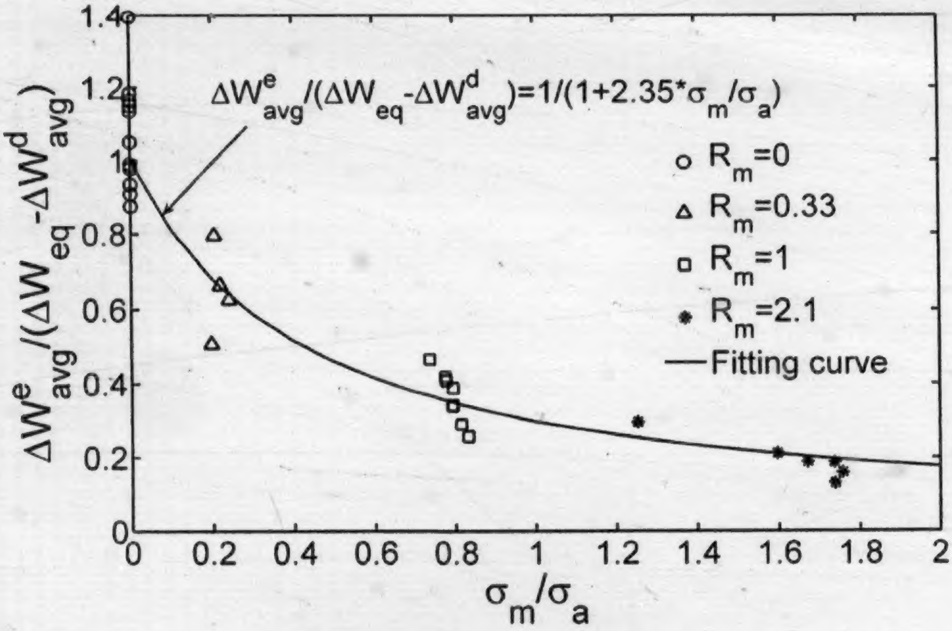

Fig. 3.30 Mean stress function for energy approach

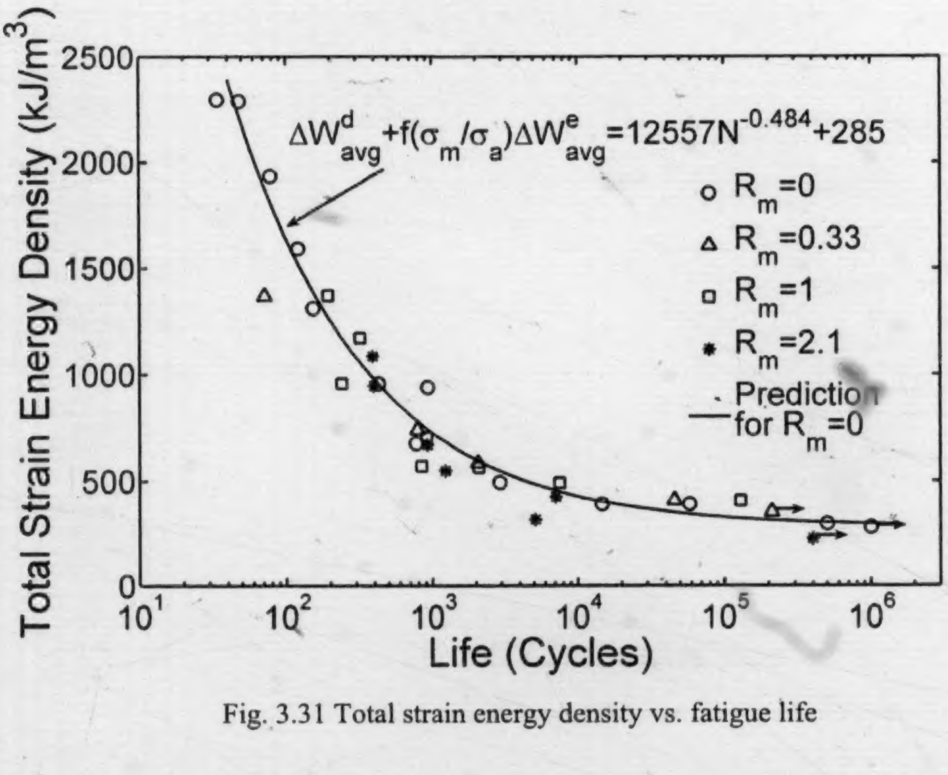

Fig. 3.31 Total strain energy density vs. fatigue life

Compared to Fig.3.27 and Fig.3.29, better prediction can be seen in energy approach than in either strain or stress approach, especially in high cycle regime. This is because at low strain amplitude level a certain variation in stress amplitude will not cause too much difference in the total strain energy density. Thus strain or stress approach may overestimate the damage at low strain amplitude level.

3.4 Ratcheting behavior and its effect on fatigue life

3.4.1 Introduction

Ratcheting is a phenomenon of progressive accumulation of deformation while materials are subjected to cyclic loading, especially under stress-controlled mode with mean stress. For metal materials, ratcheting occurs when prescribed stress exceeds the yield limit and induces plastic deformation. During past decades, many efforts have been addressed to the ratcheting behavior of metal materials in both experimental and analytical aspects (Hassan et al., 1994a, 1994b, Xia et al., 1997, Kang et al., 2002, Chen et al., 2003). In addition to cyclic fatigue damage, ratcheting deformation usually leads to extra material damage and could result in reduced fatigue life (Rider et al., 1995, Xia et al., 1996).

Ratcheting behavior has also been observed in polymer materials, such as epoxy resin (Shen et al., 2004, Xia et al., 2005). Chen et al. (2005) conducted series tests to study the ratcheting behavior of PTFE under cyclic compression load, where the effects of loading rate, mean stress and stress amplitude on the ratcheting behavior were discussed.

However, research publications on ratcheting behavior of polymer materials are still relatively few. More investigations are necessary for in-depth understanding of the ratcheting phenomenon of these materials. In addition, the influence of ratcheting strain on fatigue life of polymer materials, to the best of our knowledge, has not been reported in open publications. This might be attributed to the following two factors: Firstly, again, unavailability of reliable strain measurement devices for long term fatigue test of soft polymers limited such experiments where strain needs to be precisely measured; Secondly, ratcheting strain effect is usually coupled with a mean stress effect, which makes it more difficult to design an experimental strategy to decouple these two effects. In Section 3.3, strain-range-controlled fatigue tests of an epoxy resin with various mean strain levels were carried out. In these tests, the accumulation of ratcheting strain was restrained since the maximum and minimum strains were controlled in each cycle. Therefore, a "pure" mean stress effect on fatigue life of the epoxy polymer could be investigated. In this section, results of a series of stress-controlled uniaxial fatigue tests with various combinations of stress amplitude and mean stress are presented. In these tests, ratcheting strains were accumulated as soon as the mean stresses were not zero. As such, a synergic effect of the mean stress and ratcheting strain would be applied to the specimens. By comparing results of these two types of fatigue tests, a "pure" ratcheting strain effect on fatigue life of the epoxy polymer may be sorted out. The stress-strain data were recorded during the entire test periods. Evolutions of mechanical parameters, such as ratcheting strain, strain range and strain energy density, have been retrieved from the stress-strain data. It was found that the accumulation of ratcheting strain had little detrimental effect on fatigue life of the epoxy polymer studied. Additional tests with several resting periods during the fatigue processes were carried out and the mechanism of the ratcheting strain of the epoxy polymer was investigated.

3.4.2 Experimental procedure

All the cyclic fatigue tests were carried out under stress-controlled mode with a loading rate of 10 MPa/s and under laboratory ambient temperature. The stress amplitude σ_a and mean stress σ_m of each test are listed in Table 3.3. To investigate influence of different loading parameters, the tests can be classified into 3 categories: same ratio of mean stress to stress amplitude σ_m / σ_a with different amplitudes (S1-S4), same stress amplitude with different mean stresses (S4-S7) and same mean stress with different amplitudes (S1, S5, S8-S10), respectively.

Stress-strain data were collected during the entire fatigue test period. Stress-strain loops of the first 5 cycles, the mid-life cycle and the last cycle of test S1 and S7 are shown in Fig.3.32, where accumulation of ratcheting strain and evolution of stress-strain hysteresis loops can be observed. Quantitative analysis of evolutions of mechanical parameters, such as ratcheting strain, strain range and strain energy densities, were carried out based on the recorded stress-strain data.

Table 3.3 Parameters and results of uniaxial fatigue tests under stress-controlled mode with mean stresses

No.	σ_a *(MPa)*	σ_m *(MPa)*	ΔW^d_{avg} *(kJ/ m^3)*	ΔW^e_{avg} *(kJ/ m^3)*	N_f *(cycles)*
S1	36.73	36.73	220.8	364.6	74
S2	31.42	31.42	70.7	239.3	667
S3	28.86	28.86	41.2	192.3	1550
S4	23.60	23.60	21.5	120.9	4547
S5	23.60	36.20	27.4	123.6	2694
S6	23.60	44.50	43.6	137.5	751
S7	23.60	49.80	64.8	138.1	253
S8	31.55	36.68	85.2	245.1	502
S9	19.92	36.70	17.4	86.6	4076
S10	15.70	36.70	7.7	50.4	96513
S11	28.86	28.86			1186
S12	28.86	28.86			1606

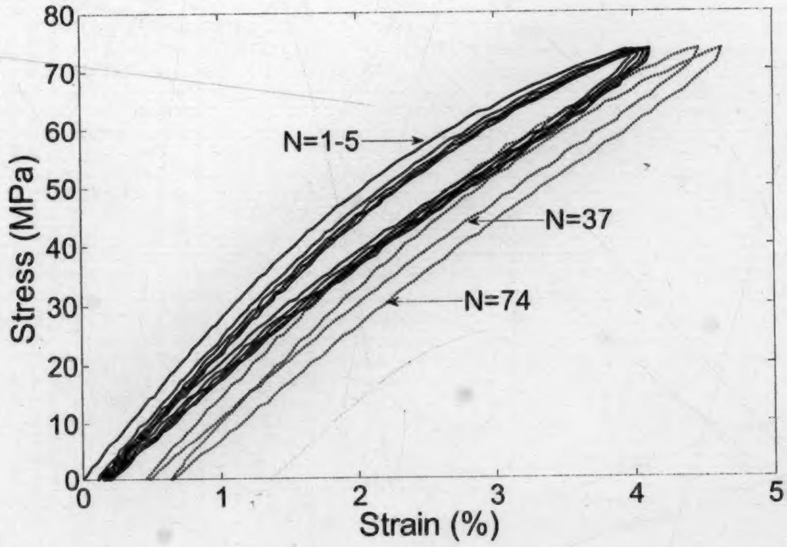

(a)

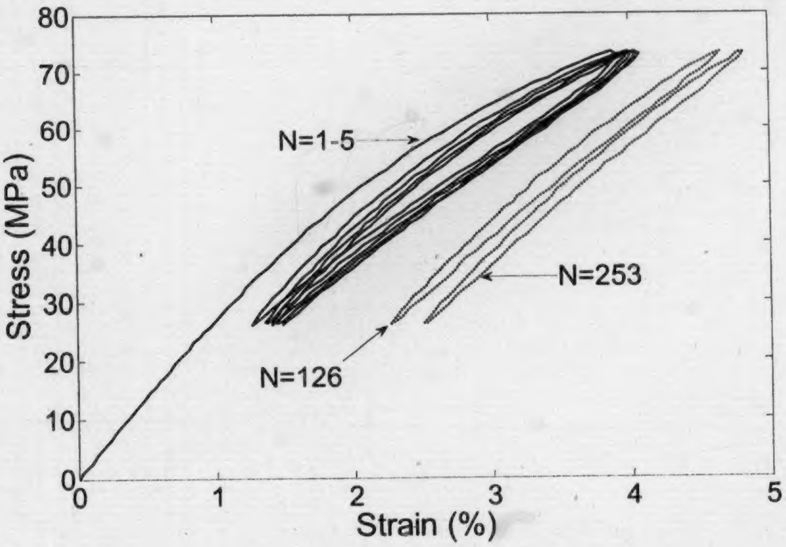

(b)

Fig. 3.32 Stress-strain loops of the first 5 cycles, the mid-life cycle and the last cycle of two tests. (a). Test S1; (b) Test S7.

3.4.3 Evolution of mechanical properties

- **Ratcheting Strain**

The accumulated ratcheting strain until *i*-th cycle is defined as the increment of mean strain until *i*-th cycle:

$$\varepsilon_{i,r} = (\frac{\varepsilon_{i,\max} + \varepsilon_{i,\min}}{2}) - (\frac{\varepsilon_{1,\max} + \varepsilon_{1,\min}}{2}) \qquad (3.30)$$

Figure 3.33(a) shows the accumulated ratcheting strain in the tests with different stress amplitudes but same mean stress ratio, where it can be seen that the ratcheting strain rate increases with increase of σ_a. The mean stress ratio is defined as:

$$R_{m,stress} = \frac{\sigma_m}{\sigma_a} \tag{3.31}$$

Note that the conventionally adopted stress ratio is defined as:

$$R_{stress} = \frac{\sigma_{\min}}{\sigma_{\max}} \tag{3.32}$$

Therefore, the relation between $R_{m,stress}$ and R_{stress} can be derived as:

$$R_{m,stress} = \frac{\sigma_m}{\sigma_a} = \frac{\dfrac{\sigma_{\max}+\sigma_{\min}}{2}}{\dfrac{\sigma_{\max}-\sigma_{\min}}{2}} = \frac{1+\dfrac{\sigma_{\min}}{\sigma_{\max}}}{1-\dfrac{\sigma_{\min}}{\sigma_{\max}}} = \frac{1+R_{stress}}{1-R_{stress}} \tag{3.33}$$

Accumulated ratcheting strains of the tests with the same stress amplitude but different mean stresses are plotted in Fig.3.33(b), where an increase of ratcheting strain rate with increase of mean stress can be observed. Figure 3.33(c) shows the accumulated ratcheting strains in the tests with the same mean stress but with different stress amplitudes. An increase of ratcheting strain rate with increase of stress amplitude can be observed.

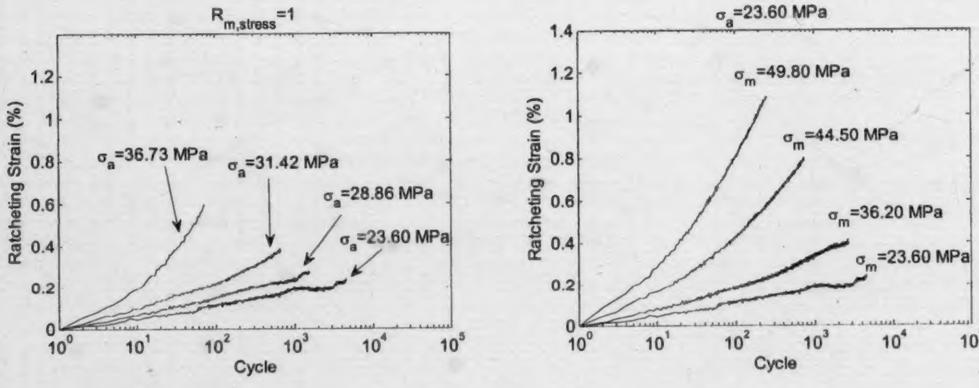

(a) (b)

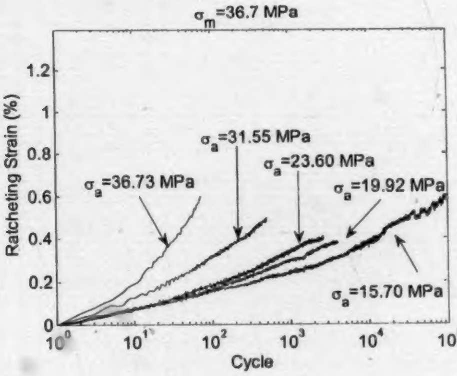

(c)

Fig. 3.33 Ratcheting strain of fatigue tests under stress-controlled mode. (a) same mean stress ratio; (b) same stress amplitude; (c) same mean stress.

It is worth to mention that slopes of the ratcheting strain curves in the semi-log scale do not represent the actual ratcheting strain rate per cycle. It actually decreases with increase of number of cycles as shown in Fig.3.34, where ratcheting strain and ratcheting strain rate of test S7 are plotted on a linear scale.

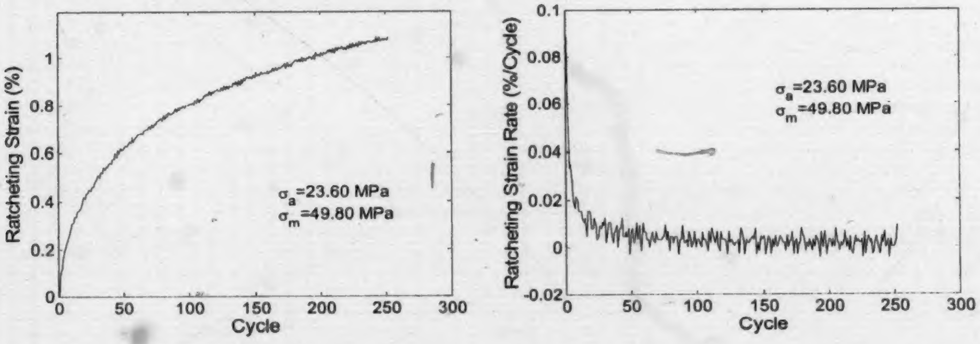

(a) (b)

Fig. 3.34 Ratcheting strain and ratcheting strain rate of test S7. (a) ratcheting strain; (b) ratcheting strain rate.

From Fig.3.33 one can see that no stable level of ratcheting strain was achieved up to the failure of the specimens in all the tests, although the ratcheting rate became very small in the high cycle region.

- **Strain Range**

Strain range evolves while the specimen is cyclically loaded under stress-controlled mode. Figure 3.35(a) shows the strain range evolution of the tests with different stress amplitudes but the same mean stress ratio. It can be seen that at the highest stress amplitude, $\sigma_a = 36.73\,\text{MPa}$ (test S1), strain range experiences first a little drop and then recovered with small variation. At lower stress amplitudes, decrease of strain range can be noticed with increase of cycles but the changes are not significant. For tests with the same stress amplitude but different mean stresses, strain range evolutions are shown in Fig.3.35(b), where strain range decrease can be observed. The decrease of strain range is more obvious for higher mean stress tests. One may also notice that for the same stress amplitude the initial strain range is larger for tests with higher mean stresses. This is due to the nonlinear stress-strain effect of the epoxy polymer at high stress level. However, the difference of strain ranges between the tests in Fig.3.35(b) diminishes with increase of number of cycles. Strain ranges of tests with the same mean stress but different stress amplitudes are shown in Fig.3.35(c). Strain range decrease can be observed for all the tests except that with the highest stress amplitude (test S1). Strain range evolution of this epoxy polymer can be attributed to combined effects of decrease of modulus and decrease of nonlinear strain during the fatigue process. The former would cause increase of the strain range whereas the latter could result in decrease of strain range under stress-controlled mode. This is essentially the same mechanism as that of cyclic softening and hardening of this epoxy polymer under strain-range-controlled cyclic loading as described in the previous sections 3.2.4.

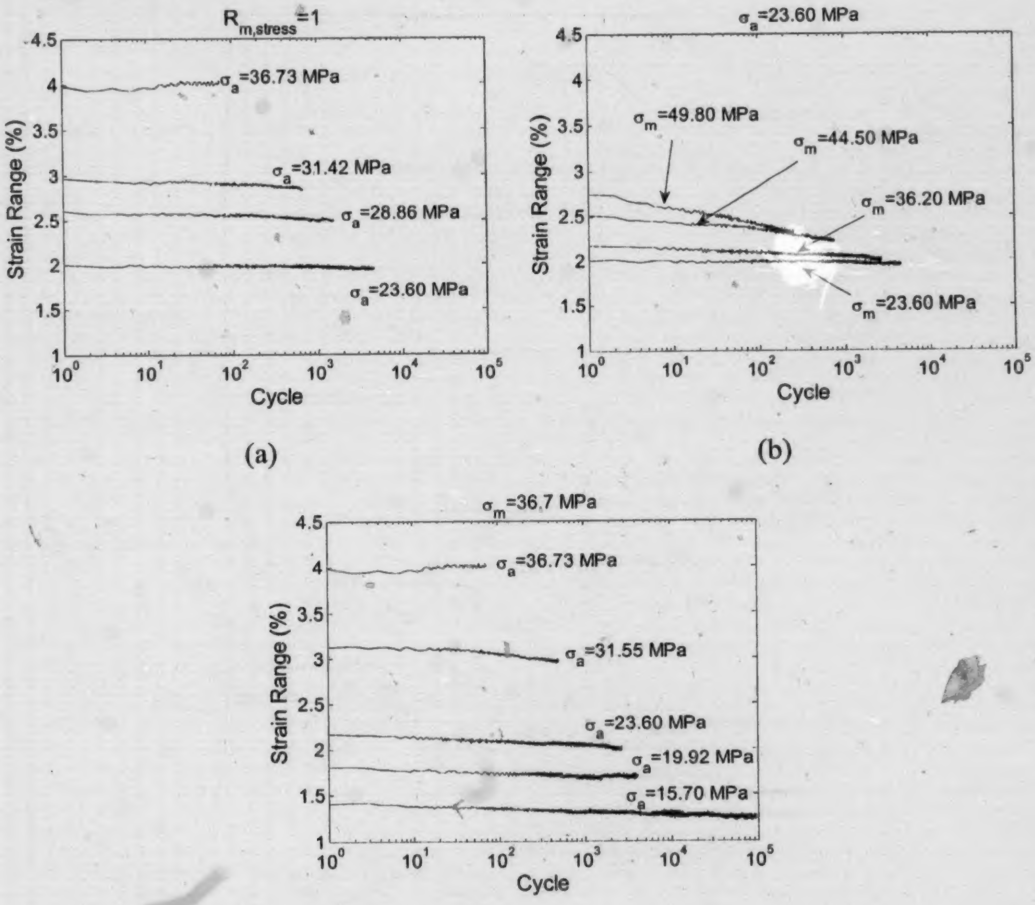

(a) (b)

(c)

Fig. 3.35 Strain range of fatigue tests under stress-controlled mode. (a) same mean stress ratio; (b) same stress amplitude; (c) same mean stress.

- **Strain Energy Density**

Both dissipated strain energy density ΔW^d and elastic strain energy density amplitude ΔW^e, are considered to contribute to the damage in this epoxy polymer during the fatigue process. Based on the recorded stress-strain data, ΔW^d and ΔW^e can be calculated by integrating the corresponding areas shown in Fig.1.16. Figure 3.36(a) and Fig.3.37(a) show the evolutions of ΔW^d and ΔW^e of those tests with different stress amplitudes but same mean stress ratio, respectively. The dissipated strain energy density ΔW^d stays nearly stable for the highest stress amplitude and lowest stress amplitude tests, while for the two tests with middle range stress amplitudes, decreasing trends can be observed. However, the elastic strain energy density amplitude ΔW^e stays stable for all these tests.

Evolutions of ΔW^d and ΔW^e of tests with the same stress amplitude but different mean stresses are shown in Fig.3.36(b) and Fig.3.37(b), respectively. It can be seen that with the increase of mean stress, initial value of ΔW^d increases because of the high nonlinearity of stress-strain relationship at high stress level. However, ΔW^d decreases with the increase of cycles and higher mean stress leads to higher decrease rate. It also can be observed that for different tests ΔW^d tends to converge with the increase of cycles. This could be attributed to the decrease of nonlinearity of stress-strain relationship during the fatigue process. ΔW^e of all tests with the same amplitude are almost the same and their values stay stable during the fatigue test periods.

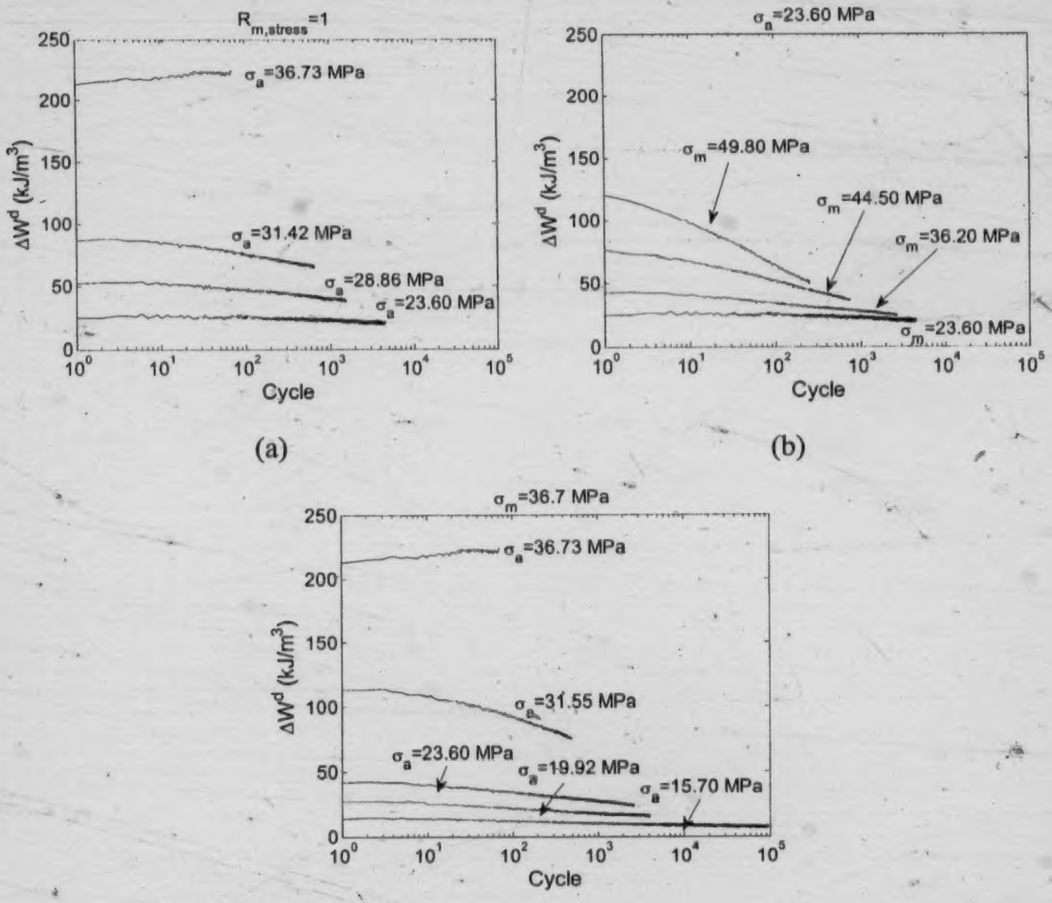

(a) (b)

(c)

Fig. 3.36 Dissipated strain energy density of fatigue tests under stress-controlled mode. (a) same mean stress ratio; (b) same stress amplitude; (c) same mean stress.

For tests with the same mean stress but different stress amplitudes, evolutions of ΔW^d and ΔW^e are plotted in Fig.3.36(c) and Fig.3.37(c), respectively. ΔW^d decreases with increase of cycles for all these tests except the one with the highest stress amplitude, but ΔW^e all stays stable during the entire fatigue life period.

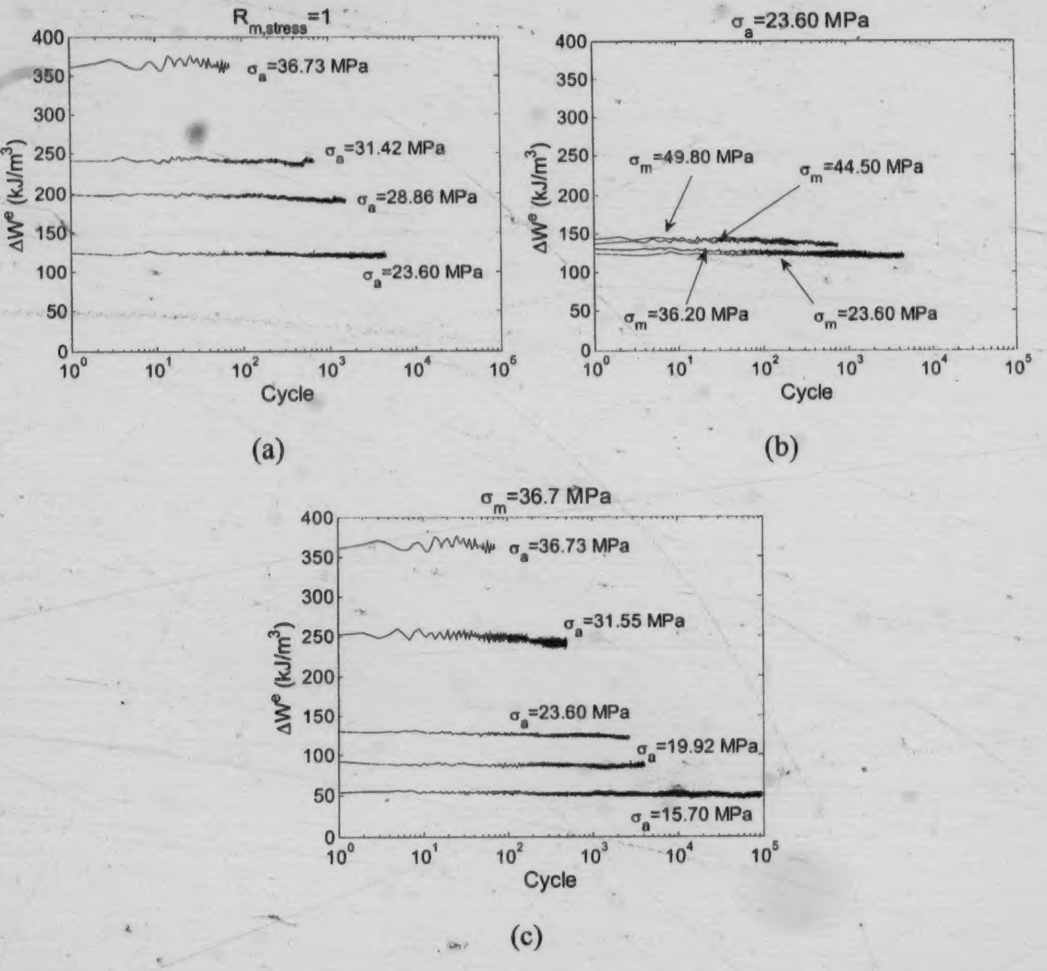

(a) (b)

(c)

Fig. 3.37 Elastic strain energy density amplitude of fatigue tests under stress-controlled mode. (a) same mean stress ratio; (b) same stress amplitude; (c) same mean stress.

3.4.4 Ratcheting effect on fatigue life

As discussed in Section 3.3, mean stress would have distinctive effect on fatigue life of materials. Two types of tests were generally used to study the mean stress effect: stress-controlled fatigue test and strain-controlled fatigue test. If the material response is mainly within the elastic region, the above two test modes will be equivalent. However, if the material response is elastic-plastic, these two test modes may produce quite different results. In the stress-controlled test, the existence of mean stress would lead to plastic strain accumulation in each cycle as so called ratcheting strain, which might cause additional damage and result in shorter fatigue life. However, for the strain-controlled test, mean stress relaxation will occur during the early stage, which may ease the mean stress effect. As suggested in (Xia et al., 1996), ratcheting strain effect on fatigue life may be decoupled from mean stress effect in stress-controlled fatigue test.

Mean stress/strain effect on fatigue life of this epoxy polymer material has been identified by introducing mean stress/strain functions into the damage parameters in Section 3.3. The mean stress/strain functions were calibrated by strain-range-controlled uniaxial fatigue tests with various mean strain ratios, $R_{m,strain}$, as in Eq.(3.31). The relations between the damage parameters and the fatigue lives were calibrated as Eq.(3.22), (3.26) and (3.29). Because of ratcheting strain accumulation, the strain approach is not suitable for fatigue life prediction of stress-controlled fatigue tests. Therefore, equivalent stress amplitude (left hand side of Eq.(3.26)) and total strain energy density (left hand side of Eq.(3.29)) of each test were calculated and plotted against fatigue life in Fig.3.38 and Fig.3.39 for the stress approach and the energy approach, respectively. In order to compare the fatigue life from strain-range-controlled tests and stress-controlled tests, results of strain-range-controlled tests with various mean strain ratios were also plotted in Fig.3.38 and Fig.3.39.

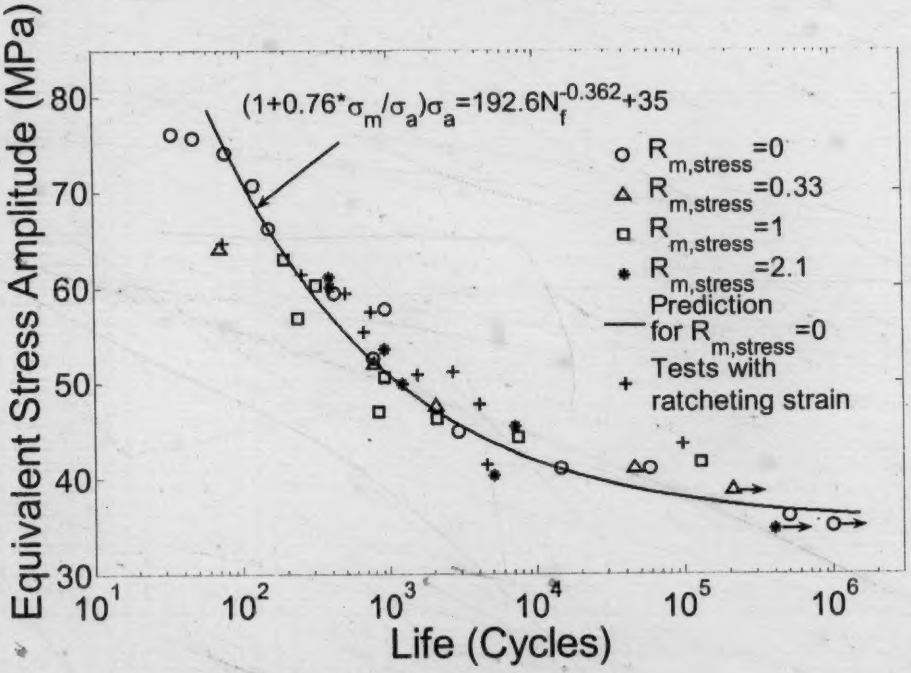

Fig. 3.38 Equivalent stress amplitude vs. fatigue life in stress-controlled fatigue tests with mean stresses.

It can be seen that all the test points with ratcheting strains basically fell within the scatter bands of the points of the strain-range-controlled fatigue tests. Equations (3.26) and (3.29) are also applicable to the stress-controlled fatigue tests. Therefore, contrary to the fatigue behavior of metals, for the epoxy polymer studied no distinctive ratcheting strain effect on fatigue life can be observed. This might be attributed to the different ratcheting mechanism of epoxy polymer material in comparison to the metals, as explained later.

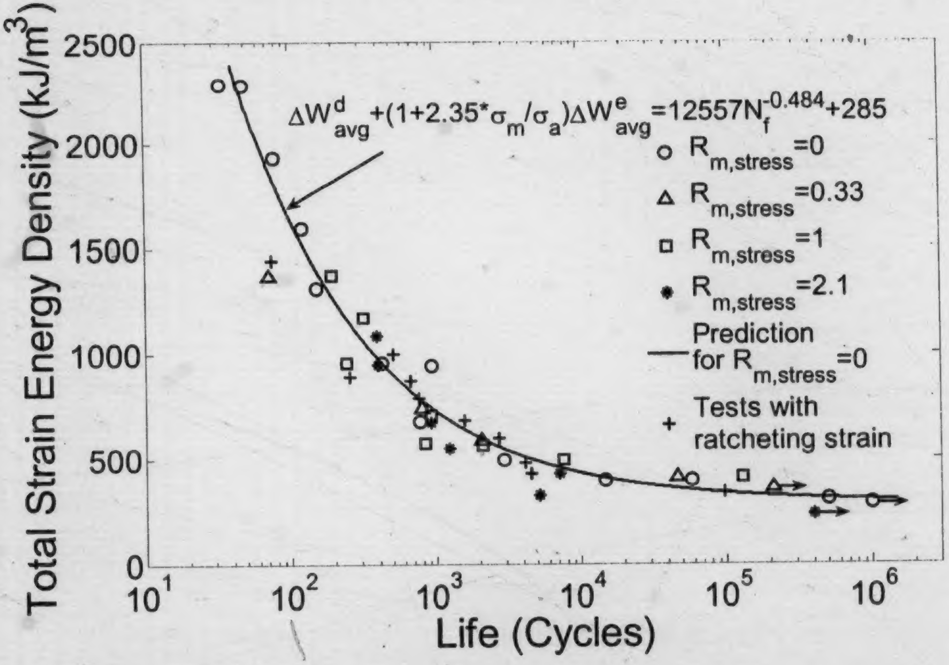

Fig. 3.39 Total strain energy density vs. fatigue life in stress-controlled fatigue tests with mean stresses.

Comparing Fig.3.38 and Fig.3.39, one can see that the energy parameter has a better correlation with fatigue life than that for stress amplitude. This is attributed to the ability of the energy approach to inherently include the stress-strain relation in the damage parameter. However, for stress approach or strain approach, only a stress or strain parameter is considered and their relationship is usually omitted.

3.4.5 Mechanism of ratcheting strain in epoxy polymer

To investigate the mechanism of ratcheting strain of this epoxy polymer, 2 more tests (S11-S12) were carried out under the same stress range as S3 but with multiple resting periods (zero loading) during the fatigue processes. Resting period equivalent to the time of 3000 cycles was applied following each 500 cycles and 300 cycles of cyclic loading for S11 and S12, respectively. Ratcheting strain of tests S11 and S12 were plotted against S3 in Fig.3.40, where the resting periods were omitted in the abscissa but the vertical lines show the recovery of the ratcheting strains during the resting period. It can be observed that most of the ratcheting strain was already recovered during the resting period, although the recovery process may still continue if a longer resting period was applied. Moreover, it can be observed in Fig.3.40 that after each resting period ratcheting strain increased rapidly and asymptotically reached the ratcheting strain curve without the resting periods. No significant difference in fatigue life was noticed between test S11, S12 and S3. This has further confirmed the observation from all other stress-controlled or strain-range-controlled fatigue tests of the current epoxy polymer material that the ratcheting strain accumulated during the stress-controlled cyclic loading has essentially no detrimental effect on the fatigue life.

This phenomenon might be explained as follows. The ratcheting strain in the epoxy polymer is generally composed of two parts, viscoelastic and viscoplastic. The former is recoverable after the load is removed with enough resting time elapsed and the latter is unrecoverable permanent deformation. For the current epoxy, experiments show that the ratcheting strain is primarily viscoelastic in nature. The recoverable viscoelastic strain had not introduced damage in the epoxy and therefore will not influence the fatigue life.

This is in contrast to metallic materials where the ratcheting strain accumulated is primarily plastic in nature. After a resting period, when the specimen is reloaded under the same condition as before resting, there is a short transition period where the viscoelastic ratcheting strain accumulates quickly again and then the total ratcheting strain will reach a stable state which coincides with the test without resting period. This could be another indication of the recoverability of the ratcheting strain.

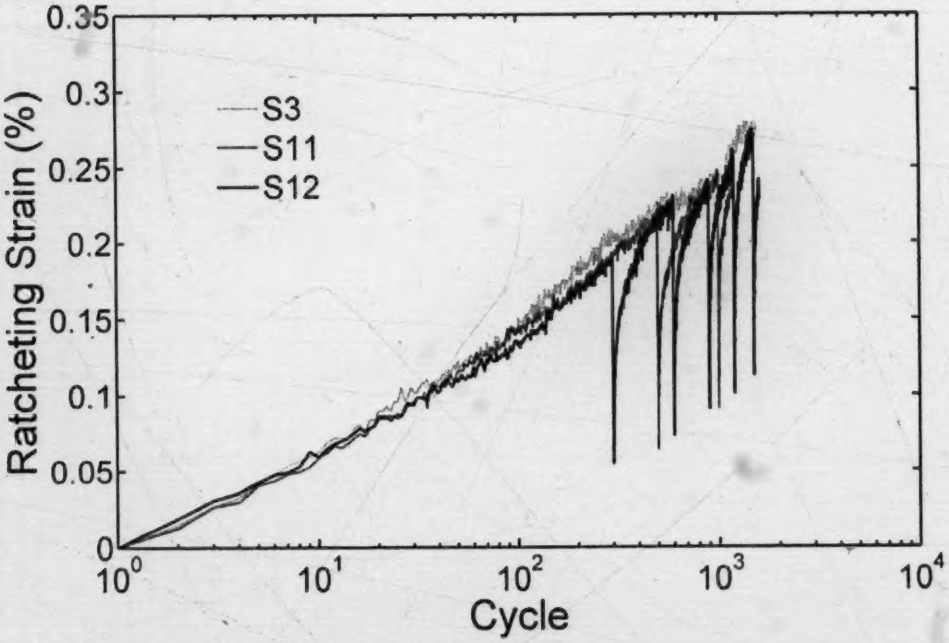

Fig. 3.40 Ratcheting strain of fatigue tests with and without resting period.

3.5 Conclusions

Uniaxial fatigue tests have been performed on an Epon 826 Resin and Epi-Cure Curing Agent 9551 system (a bisphenol A / non-MDA (methylene dianiline) polyamine system) under both stress-controlled and strain-range-controlled mode with and without mean stress/strain. By using the non-contact real-time strain measurement and control system, engineering strain could be precisely measured during the entire fatigue life. Therefore, the evolution of mechanical properties of the epoxy polymer during fatigue process can be retrieved from the recorded stress-strain data and quantitatively analyzed, such as the stress/strain range, elastic modulus, nonlinear effect in stress-strain relation, mean stress, ratcheting strain, elastic and dissipated strain energy densities, and etc. The quantitative investigation of the degradation of mechanical properties during fatigue process enabled the in-depth study of the fatigue mechanism. Modulus drop and decrease of nonlinear strain range are found to be two basic phenomena observed in all uniaxial fatigue tests. The former causes a decrease in stress range and the latter causes an increase in stress range in strain-range-controlled fatigue tests. As a combined effect of these two factors, cyclic hardening was observed in the fatigue tests with higher tensile mean strain whereas cyclic softening was observed in the fatigue tests with lower mean strain and in the fully-reversed fatigue tests. The evolution of strain energy densities also depends on the combination of these two effects.

- Basic phenomenological fatigue life prediction functions (stress-, strain- and energy-based approaches) were obtained by strain-range-controlled fully-reversed fatigue tests, where no mean stress/strain exists. Fractographic analysis clearly show three stages of fatigue crack propagation on the ruptured surfaced of the specimens. A typical feature of fatigue crack propagation, i.e. striations, was observed in the stable fatigue crack propagation zone.

For strain-range-controlled fatigue tests with mean stresses, mean stress relaxation has been observed. It was found that mean stress level relaxed during the initial stage of fatigue process and then a nearly saturated state was achieved which occupied rest part of the fatigue life. Therefore, the mean stress/strain effect was able to be characterized by introducing a mean stress/strain function into the damage parameters. The procedure to calibrate the mean stress/strain function was illustrated in terms of the three approaches, respectively. Good agreement can be seen between the experimental data and fatigue life prediction curves for all these three approaches, among which energy approach was found to be the best, especially in high cycle regime.

Series of stress-controlled fatigue tests with mean stresses were also performed to study the ratcheting strain effect on fatigue life. By comparing fatigue life results with strain-range-controlled fatigue test results in which the ratcheting strains were restrained, it was found that the ratcheting strain has essentially no detrimental effect on the fatigue life of the epoxy material studied. Therefore, the stress or energy density based fatigue theories can be well correlated to the fatigue lives of this epoxy material either under stress- or strain-range-controlled cyclic loading with mean stress or mean strain. The mechanism of such observation was further investigated by performing additional cyclic tests with multiple resting periods. It was found that ratcheting strain in this epoxy polymer is mainly recoverable viscoelastic deformation which will not introduce damage in the material.

Bibliography

1. Chen X, Hui S. Ratcheting behavior of PTFE under cyclic compression. Polymer Testing 2005; 24(7):829-833.
2. Chen X, Kim K. Modeling of ratcheting behavior under multiaxial cyclic loading. Acta Mechanica 2003; 163(1-2):9-23.
3. Clark TR, Hertzberg RW, Mohammadi N. Fatigue mechanisms in poly(methyl methacrylate) at threshold: effects of molecular weight and mean stress. J Mat Sci 1993;28(19):5161-5168.
4. Ellyin F. Fatigue Damage, Crack Growth, and Life Prediction. Chapman & Hall, London, UK, 1997.
5. Fang D, Berkovits A. Mean stress models for low-cycle fatigue of a nickel-base superalloy. Int J Fatigue 1994;16(6):429-437.
6. Gerber H. Bestimmung der zulassigen Spannungen in eisen Constructionen. Z Bayer Arch Ing Ver 1874;6:101-110.
7. Goodman J. Mechanics applied to engineering. London: Longmans, Green and Company, 1899.
8. Hassan T, Kyriakides S. Ratcheting of cyclically hardening and softening materials: I. Uniaxial behavior. Int J Plast 1994a;10(2):149-184.
9. Hassan T, Kyriakides S. Ratcheting of cyclically hardening and softening materials: I. Multiaxial behavior. Int J Plast 1994b;10(2):185-212.

10. Ishiyama C, Asai T, Kobayashi M, Shimojo M, Higo Y. Fatigue Crack Propagation Mechanisms in Poly(methyl methacrylate) by In Situ Observation with a Scanning Laser Microscope. Journal of Polymer Science: Part B: Polymer Physics 2001; 39(24):3103-3113.
11. Kang G, Gao Q, Yang X. A visco-plastic constitutive model incorporated with cyclic hardening for uniaxial/multiaxial ratcheting of SS304 stainless steel at room temperature. Mechanics of Materials 2002; 34(9):521-531.
12. Kujawski D, Ellyin F. A unified approach to mean stress effect on fatigue threshold conditions. Int J Fatigue 1995;17(2):101-106.
13. Kwofie S. An exponential stress function for predicting fatigue strength and life due to mean stresses. Int J Fatigue 2001;23(9):829-836.
14. McClaflin D, Fatemi A. Torsional deformation and fatigue of hardened steel including mean stress and stress gradient effects. Int J Fatigue 2004;26(7):773-784.
15. Morrow J. In 'Internal Friction, Damping, and Cyclic Plasticity', ASTM STP 378, American Society for Testing and Materials, Philadelphia, 1965;45-87.
16. Koh SK, Oh SJ, Li C, Ellyin F. Low-cycle fatigue life of SiC-particulate-reinforced Al-Si cast alloy composites with tensile mean strain effects. Int J Fatigue 1999;21(10):1019-1032.
17. Mallick PK, Zhou Y. Effect of mean stress on the stress-controlled fatigue of a short E-glass fiber reinforced polyamide-6,6. Int J Fatigue 2004;26(9):941-946.
18. Rider RJ, Harvey SJ, Chandler HD. Fatigue and ratcheting interactions. Int J Fatigue

1995;17(7):507-511.

19. Sauer JA, McMaster AD, Morrow DR. Fatigue behavior of polystyrene and effect of mean stress. J Macromol Sci Phys 1976;B12(4):535-562.

20. Shen X, Xia Z, Ellyin F. Cyclic Deformation Behavior of an Epoxy Polymer. Part I: Experimental Investigation. Polym Eng and Sci 2004;44(12):2240-2246.

21. Smith KN, Watson P, Topper TH. Stress-strain function for the fatigue of metals. J Mater, JMLSA 1970;5(4):767-778.

22. Soderberg CR, Sweden V. Factor of Safety and Working Stress. ASME Transaction, AER-IS, 1930;52(2):13-28.

23. Strizak JP, Mansur LK. The effect of mean stress on the fatigue behavior of 316 LN stainless steel in air and mercury. J Nuclear Mat 2003;318:151-156.

24. Wöhler A. Tests to determine the forces acting on railway carriage axles and the capacity of resistance of the axles. Engineering 1871; 11.

25. Xia Z, Ellyin F. A constitutive model with capability to simulate complex multiaxial ratcheting behavior of materials. Int J Plast 1997; 13(1-2):127-142.

26. Xia Z, Kujawski D, Ellyin F. Effect of mean stress and ratcheting strain effect on fatigue life of steel. Int J Fatigue 1996;18(5):335-341.

27. Xia Z, Shen X, Ellyin F. Biaxial Cyclic Deformation of an Epoxy Resin: Experiments and Constitutive Modeling. J Mat Sci 2005;40(3):643-654.

Chapter 4

Multiaxial Fatigue Behavior

4.1 Introduction

Multiaxial fatigue life prediction of engineering materials had challenges over the past decades, especially, when superimposed mean stresses were applied. However, an effective multiaxial fatigue life prediction method would be valuable for practical applications since most of the load-bearing components serve under complex multiaxial loading conditions, such as the landing gear of the aircraft, the oil transportation pipeline. The epoxy polymers as the matrix-phase in fiber-reinforced composites usually experience complicated multiaxial cyclic stresses in their service lives. And the fatigue crack usually initiates in the relative weak matrix or fiber-matrix interface. Therefore, investigation on multiaxial fatigue behavior of the epoxy polymer would improve our fundamental understanding of the mechanism of the cyclic degradation and fatigue behavior of not only the epoxy material itself but also the reinforced composite materials.

As a typical multiaxial fatigue test, cyclic shear fatigue test has been extensively adopted in investigations for metals (Mayer, 2006, Chen et al., 2006, Marquis et al., 2000) and for composites (Lee et al., 2004, Li et al., 2003, Lease et al., 1996). (The pure shear is equivalent to a biaxial principal stress state having the same amplitude but opposite signs in the two principal directions.) Moreover, axial-shear combined cyclic loading are also very popular in investigations of multiaxial fatigue behavior of materials (Gude et al., 2006, de Freitas et al., 2006, Qi et al., 2007). Some research work has been reported on the uniaxial fatigue behavior of epoxy polymers. However, there have been still few data on their multiaxial fatigue behavior (Isayev et al., 1981). One reason could be attributed to the lack of effective non-contact strain measurement devices in multiaxial fatigue tests of such soft materials. Moreover, synchronized measurement of normal and shear strains and stresses in multiaxial fatigue tests also increases the complexity. With the help of the non-contact real-time strain measurement system described in Chapter 2, more precise strain measurement can be conducted for full fatigue lives of the specimens and thus allowing an in-depth investigation on multiaxial fatigue behavior of the epoxy polymer.

In this Chapter, fatigue test results of the epoxy polymer under pure shear loading and combined proportional axial-shear loading with and without mean stress/strain are presented. Based on the retrieved stress-strain data the evolution of mechanical properties, such as shear modulus, stress/strain range, mean stress/strain and strain energy densities were analyzed. Fatigue life predictions were performed based on stress approach, strain approach and energy approach, respectively.

4.2 Fully-reversed cyclic shear fatigue

4.2.1 Experimental procedure

The tubular specimen for multiaxial fatigue test is as shown in Fig.2.1. Totally 10 tests were carried out under fully-reversed cyclic torsional load. The test parameters and fatigue life results were listed in Table 4.1.

Table 4.1. Parameters and results of fully-reversed cyclic shear fatigue tests

No.	γ_a (%)	τ_a (MPa)	ΔW^d_{avg} (kJ/m^3)	ΔW^e_{avg} (kJ/m^3)	N_f (cycles)
S1	5.61	38.7	524.0	996.3	137
S2	5.37	38.2	455.8	961.6	158
S3	5.17	36.9	413.5	876.2	407
S4	4.21	31.3	261.5	602.4	816
S5	3.60	27.7	175.4	463.3	1341
S6	3.47	26.9	171.2	430.9	6843
S7	3.16	25.3	145.4	367.2	11361
S8	2.83	24.2	95.1	324.1	22936
S9	2.56	22.2	81.0	266.4	192605
S10	2.23	20.9	51.2	223.1	>1000000

Since previous uniaxial fatigue tests were conducted at loading rate of 10MPa/s, in order to compare current test results with them, specimens S1-S8 were tested under strain-range-controlled mode with an equivalent loading rate of 6.19MPa/s determined by Stassi criterion which will be described later. Specimens S9 and S10 were tested under stress-controlled mode with a loading rate of 61.9MPa/s for the purpose of reducing the test time. As the material response was dominantly elastic in the two later tests with smaller strain/stress amplitudes, the difference between strain-range-controlled and stress-controlled modes became insignificant. Moreover, no distinct time-dependent viscoelastic deformation will occur at such low strain levels. All the fatigue tests were lasted until structural failure.

4.2.2 Evolution of mechanical properties

Figure 4.1 shows typical stress-strain loops of the first, mid and last cycle of test S2. With increasing cycles, decreases of the modulus and the nonlinearity of the stress-strain relation can be observed. Such similar trends were also observed in the uniaxial fatigue tests of this epoxy polymer.

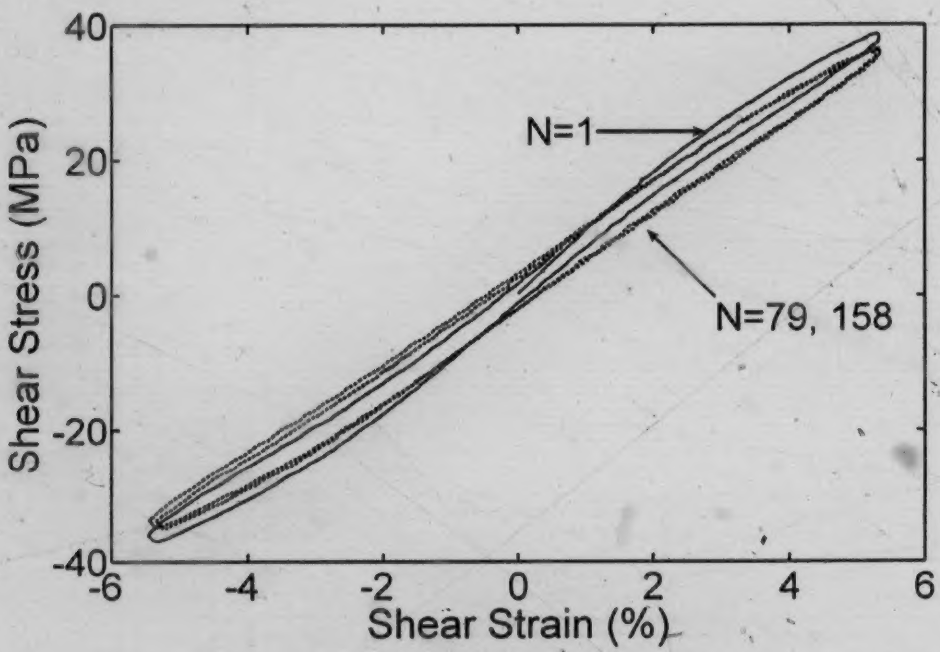

Fig. 4.1 Evolution of stress-strain loop of fatigue test S2.

Evolutions of mechanical parameters (shear modulus, shear stress range and strain energy densities) of tests S1-S8 were retrieved from the stress-strain data and they are shown as below.

- **Shear modulus**

For each test, the shear modulus was calculated as the slope of the best fitting line of the stress-strain curve at the initial part of loading stage in each cycle. The evolution of the shear modulus for individual test is shown in Fig.4.2.

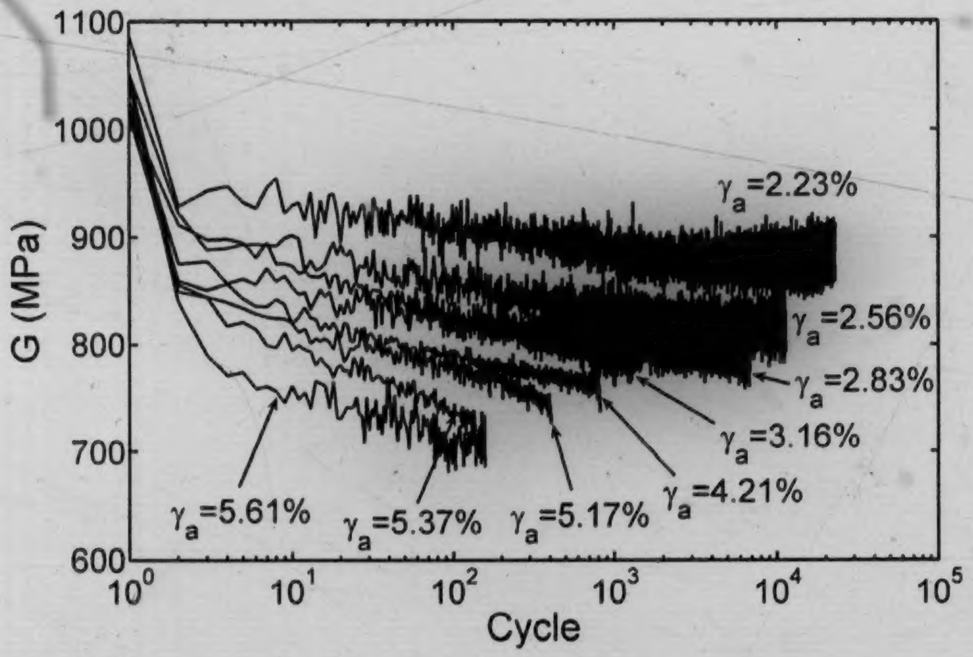

Fig. 4.2 Evolutions of shear modulus during the entire fatigue life periods of strain-range-controlled fully reversed cyclic torsional fatigue tests.

A precipitous drop of the shear modulus can be seen during the initial two cycles for all tests. As the number of cycles increases, the rate of modulus drop slows down. Stable levels of shear modulus could be achieved in the rest life of tests with low strain amplitudes. While for the high strain amplitude tests, no stable stages can be observed. It can also be observed that with the increase of the strain amplitude, the shear modulus drop becomes more severe. All these observations are found in consistency with the modulus drop phenomenon in the uniaxial fatigue tests of this epoxy polymer as demonstrated in Chapter 3. According to the elasticity theory, the shear modulus can be calculated as $G = 0.5E/(1+\upsilon)$, where E is the elastic modulus and υ is the Poisson's ratio. Taking $E = 2900MPa$ from section 3.2.2 and $\nu = 0.42$ from previous results (Xia et al., 2003), the shear modulus of the specimen at virgin stage (first cycle) was calculated as 1021MPa, which is consistent with current test results.

- **Shear stress range**

The evolution of shear stress range of each test was retrieved from the stress-strain data and is plotted in Fig.4.3. A decreasing trend with increasing cycles is observed for all these tests, indicating a cyclic softening phenomenon. In addition, an approximate linear relationship of stress range with number of cycles can be observed in the semi-log scale graphics. The rate of decrease of shear stress range becomes higher with the increase of strain amplitude. As explained in Chapter 3, the evolution of stress range during cyclic loading is due to the competition between modulus drop and decrease of nonlinearity of the stress-strain relation. In a strain-range-controlled cyclic fatigue test, the former would lead to a stress range decrease whereas the latter would result in a stress range increase. In the current cyclic shear tests, the effect of modulus drop is more severe than that of the decrease of nonlinearity of stress-strain relation, resulting in the phenomenon of cyclic softening.

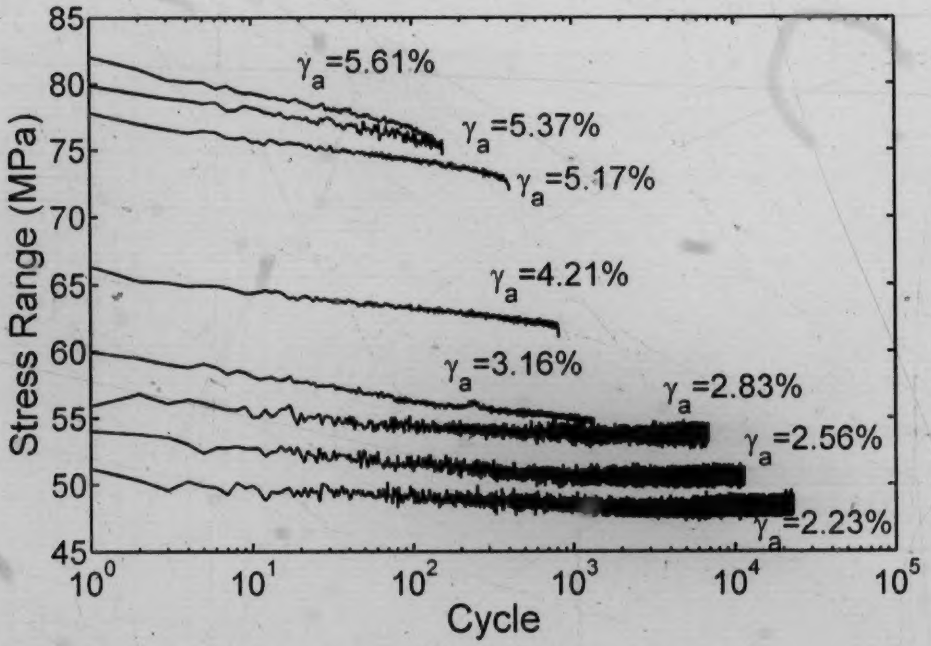

Fig. 4.3 Evolutions of shear stress ranges during the entire fatigue life periods of strain-range-controlled fully reversed cyclic torsional fatigue tests.

- **Strain energy densities**

As an important parameter to evaluate the fatigue damage of the specimen, Dissipated Strain Energy Density (DSED), ΔW^d, was calculated from the area enclosed by the stress-strain hysteresis loop as shown in Fig. 4.4.

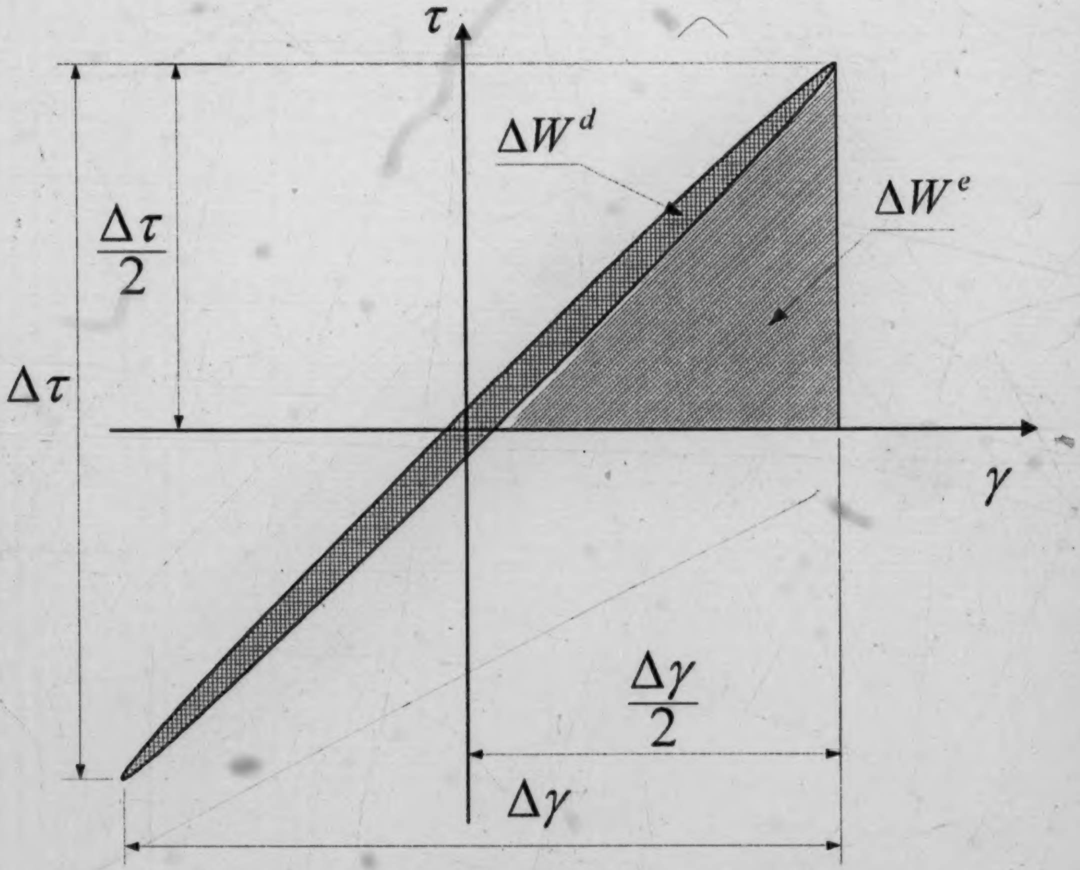
τ
ΔW^d
ΔW^e
$\frac{\Delta\tau}{2}$
$\Delta\tau$
γ
$\frac{\Delta\gamma}{2}$
$\Delta\gamma$

Fig. 4.4 Illustration of the strain energy density components.

The evolution of ΔW^d of each test is plotted in Fig.4.5. At high strain amplitude level, an increasing trend can be observed in the semi-log scale. Whereas at low strain amplitude level, ΔW^d keeps almost constant through the fatigue process. ΔW^d_{avg}, the average value of ΔW^d of all cycles in each test, was chosen as the parameter of DSED as listed in Table 4.1.

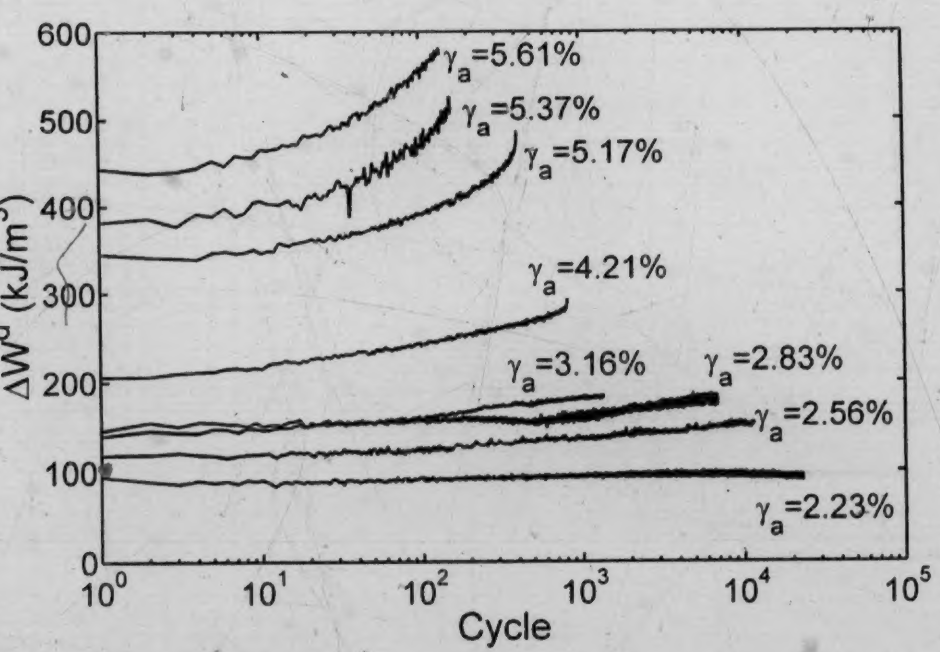

Fig. 4.5 Evolutions of dissipated strain energy densities during the entire fatigue life periods of strain-range-controlled fully reversed cyclic torsional fatigue tests.

To consider the hydrostatic pressure effect, in addition to DSED, Elastic Strain Energy Density Amplitude (ESEDA) was also considered to contribute to the damage in the specimen during cyclic loading as the same manner in Chapter 3. In the case of pure shear loading, ESEDA can be expressed as:

$$\Delta W^e = \int_{\sigma_1^m}^{\sigma_1^{max}} \sigma_1 d\varepsilon_1^e + \int_{\sigma_2^m}^{\sigma_2^{max}} \sigma_2 d\varepsilon_2^e \qquad (4.1)$$

where σ_1, σ_2, ε_1^e and ε_2^e are stress and elastic strain components in the principle directions. Superscript "max" and "m" indicate maximum stress and mean stress, respectively. In the principle directions, $\sigma_1 = \tau$, $\sigma_2 = -\tau$, $\varepsilon_1 = \frac{\gamma}{2}$, $\varepsilon_2 = -\frac{\gamma}{2}$,

$\sigma_1^m = \sigma_2^m = \tau^m$, $\sigma_1^{\max} = \tau^{\max}$ and $\sigma_2^{\max} = -\tau^{\min}$. In the case of fully reversed cyclic shearing test, $\tau^{\max} = -\tau^{\min}$. Therefore, Eq.(4.1) can be written as:

$$\Delta W^e = \int_{\tau^m}^{\tau^{\max}} \tau d\frac{\gamma^e}{2} + \int_{\tau^m}^{\tau^{\max}} (-\tau) d\left(-\frac{\gamma^e}{2}\right) = \int_{\tau^m}^{\tau^{\max}} \tau d\gamma^e \tag{4.2}$$

which is represented by the area indicated in Fig.4.4. ΔW^e of all tests are plotted in Fig.4.6. It can be seen that ΔW^e decreases with increasing cycles in the tests with larger strain amplitudes, while it is almost unchanging in the tests with lower strain amplitudes. This can be attributed to the cyclic softening of this material. Similarly, ΔW^e_{avg}, the average value of ΔW^e, is chosen as the representative parameter of ESEDA in the next section's analysis.

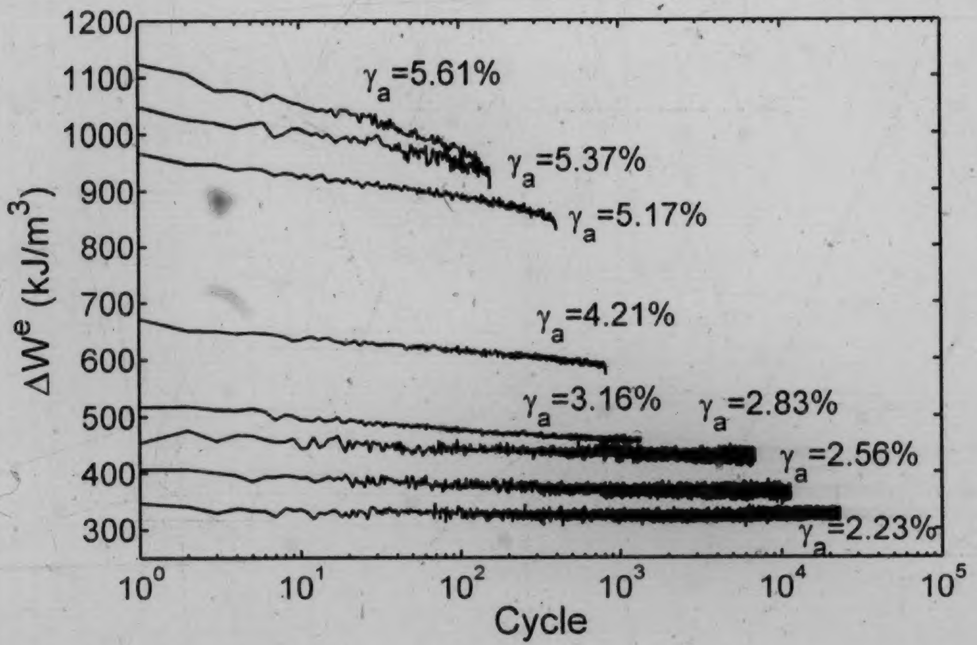

Fig. 4.6 Evolutions of elastic strain energy density amplitudes during the entire fatigue life periods of strain-range-controlled fully reversed cyclic torsional fatigue tests.

4.2.3 Fatigue life prediction with three approaches

Equivalent stress/strain concepts were usually adopted to unify the multiaxial fatigue theories with the uniaxial fatigue theories (Ellyin, 1997). Therefore, selecting an appropriate equivalent stress/strain is the most important step to obtain a good correlation of the multiaxial fatigue data with the uniaxial one. Moreover, as in the uniaxial fatigue behavior analysis in Chapter 3, the total strain energy density is also chosen as a damage parameter in fatigue life prediction. Comparisons are made between shearing fatigue results and results of uniaxial fatigue tests in the context of three life prediction approaches: stress-based approach, strain-based approach and energy-based approach, respectively.

- **Stress-based approach**

The shear stress ranges show an approximately linear decreasing trend with increasing cycles in the semi-log scale as in Fig.4.3. The averaged value of stress amplitude in each test, which is half of the shear stress range, was considered as a parameter to correlate the fatigue life data and it is listed in Table 4.1. To compare with the uniaxial fatigue test results, an appropriate equivalent stress should be defined. For metallic materials, von Mises equivalent stress is most commonly adopted. While for polymers, Stassi criterion (Stassi-D'Alia, 1967) is usually considered more appropriate due to the asymmetry of tensile and compressive mechanical behavior. Von Mises equivalent stress can be expressed as:

$$\sigma_{eq} = \left[\frac{1}{2}\left[(\sigma_x - \sigma_y)^2 + (\sigma_y - \sigma_z)^2 + (\sigma_z - \sigma_x)^2 + 6\left(\tau_{xy}^2 + \tau_{yz}^2 + \tau_{zx}^2\right)\right]\right]^{\frac{1}{2}} \tag{4.3}$$

In the case of pure shear loading, von Mises equivalent stress is reduced as:

$$\sigma_{eq} = \sqrt{3}\tau_{xy} \tag{4.4}$$

To consider the asymmetry of tensile and compressive mechanical behavior of this epoxy polymer, the Stassi equivalent stress is defined from the following equation:

$$R\sigma_{seq}^2 - (R-1)I_1\sigma_{seq} - \sigma_{eq}^2 = 0 \tag{4.5}$$

where I_1 is the first invariant of the stress tenor, σ_{eq} is the von Mises equivalent stress, σ_{seq} is the Stassi equivalent stress and R is the ratio of the uniaxial compressive yield stress to the uniaxial tensile yield stress. Solving Eq.(4.5), the Stassi equivalent stress can be expresses as:

$$\sigma_{seq} = \frac{(R-1)I_1 + \sqrt{(R-1)^2 I_1^2 + 4R\sigma_{eq}^2}}{2R} \tag{4.6}$$

Note that $R = 1$ will result in $\sigma_{seq} = \sigma_{eq}$. The ratio R of this epoxy polymer was determined as 1.15 in a previous paper (Xia et al., 2003). For biaxial normal stress state, Eq.(4.5) can be written as:

$$\sigma_x^2 - \sigma_x\sigma_y + \sigma_y^2 + (R-1)\sigma_{seq}(\sigma_x + \sigma_y) - R\sigma_{seq}^2 = 0 \tag{4.7}$$

Figure 4.7 shows the comparison between the von Mises equivalent stress envelope and the Stassi equivalent stress envelop, assuming the same equivalent tensile stress level.

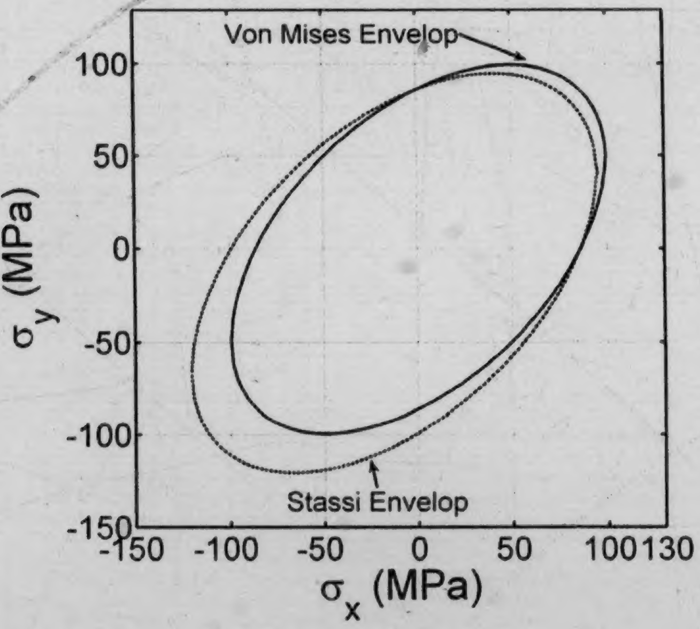

Fig. 4.7 Comparison of von Mises and Stassi equivalent stress envelops of Epon 826 Resin/Epi-Cure Curing Agent 9551.

In the case of pure shear loading, $I_1 = 0$ and the Stassi equivalent stress will be simplified as:

$$\sigma_{seq} = \frac{\sigma_{eq}}{\sqrt{R}} = \sqrt{\frac{3}{R}}\tau_{xy} \tag{4.8}$$

For $R > 1$, the Stassi equivalent stress is less than the von Mises equivalent stress. From previous uniaxial fatigue test results in Chapter 3, the following correlation between the stress amplitude and fatigue life has been obtained (Eq.(3.24)):

$$\sigma_{eq} = 192.6 \cdot N_f^{-0.362} + 35 \tag{4.9}$$

where N_f is the fatigue life and the stress unit is in MPa. The data points of both von Mises and Stassi equivalent stress amplitudes versus fatigue lives are plotted on Fig.4.8. It can be seen that most von Mises stress amplitude points are above the predictive curve, Eq.(4.9). While most Stassi stress amplitude points are below the curve. However, both seem reasonably close to the predictive curve which is obtained from the uniaxial fatigue tests. The correlation coefficient of the previous uniaxial test data and the current data with von Mises equivalent stress approach to the predictive curve, Eq.(4.9), is 0.969 which is comparable to 0.970 obtained from the Stassi equivalent stress approach. The standard deviation between the Stassi equivalent stress amplitudes and the prediction curve was calculated as 2.88 MPa, a little better than 2.98 MPa from the von Mises equivalent stress amplitude approach.

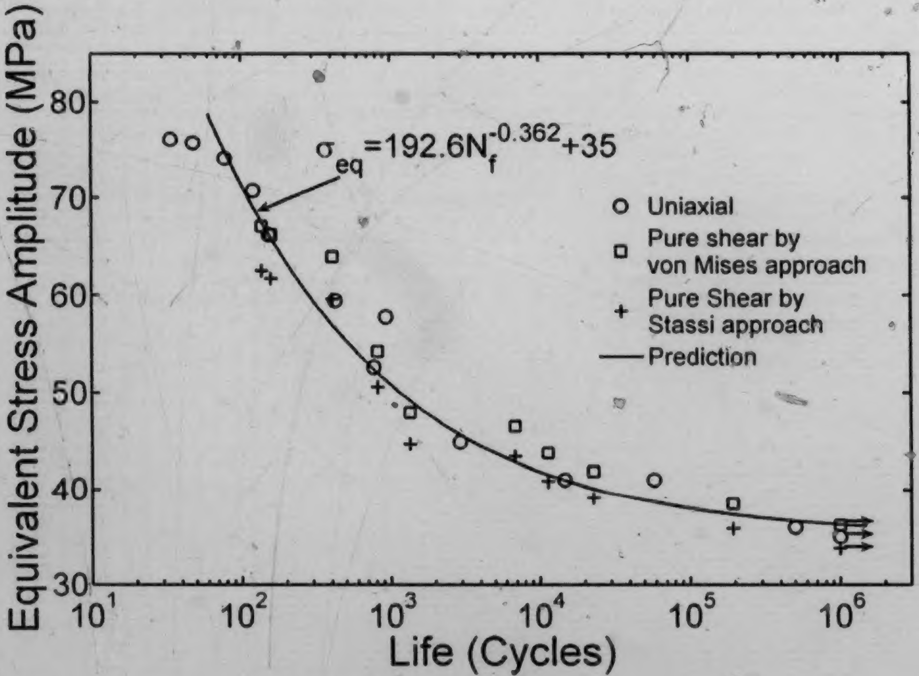

Fig. 4:8 Equivalent stress amplitude vs. fatigue life.

- **Strain-based approach**

The strain amplitude vs. fatigue life function obtained from our previous uniaxial fatigue test results is (Eq.(3.19)):

$$\varepsilon_{eq} = 0.1 \cdot N_f^{-0.347} + 1.3\% \qquad (4.10)$$

where ε_{eq} is the equivalent strain amplitude, N_f is the fatigue life. Similar to the stress approach, von Mises equivalent strain was adopted firstly:

$$\varepsilon_{eq} = \frac{1}{1+\upsilon}\left[\frac{1}{2}\left[(\varepsilon_x - \varepsilon_y)^2 + (\varepsilon_y - \varepsilon_z)^2 + (\varepsilon_z - \varepsilon_x)^2 + \frac{3}{2}\left(\gamma_{xy}^2 + \gamma_{yz}^2 + \gamma_{zx}^2\right)\right]\right]^{\frac{1}{2}} \qquad (4.11)$$

where υ is the Poisson's Ratio. In the case of pure shear loading, von Mises equivalent strain is simplified as:

$$\varepsilon_{eq} = \frac{\sqrt{3}}{2(1+\upsilon)}\gamma_{xy} \qquad (4.12)$$

Substituting shear strain amplitudes into Eq.(4.12) and taking $\upsilon = 0.42$ (Xia et al., 2003), the von Mises equivalent strain amplitudes were obtained. Then the experimental data of von Mises equivalent strain amplitudes vs. fatigue lives were plotted against the predictive curve in Fig.4.9. The correlation coefficient is 0.972.

Similarly to the Stassi equivalent stress, an alternate Stassi equivalent strain is defined as:

$$\varepsilon_{seq} = \frac{\varepsilon_{eq}}{\sqrt{R}} \qquad (4.13)$$

where ε_{seq} represents the Stassi equivalent strain and ε_{eq} is the von Mises equivalent strain. The data points of Stassi equivalent strain amplitude vs. fatigue life are also plotted in Fig.4.9 for a comparison. The correlation coefficient in this case is 0.983. The standard deviation between the Stassi equivalent strain amplitudes and the prediction curve was calculated as 0.16%, which is much better than 0.30% from the von Mises equivalent strain amplitude approach. It can be seen that Stassi criterion seems to be more appropriate to evaluate the equivalent strain in multiaxial fatigue of this epoxy polymer.

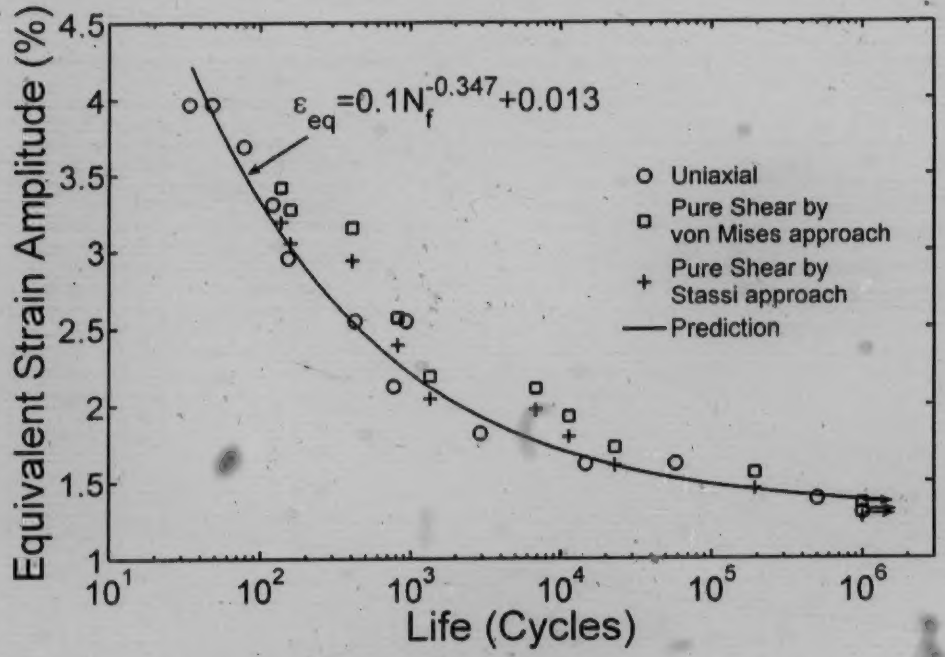

Fig. 4.9 Equivalent strain amplitude vs. fatigue life.

- **Energy-based approach**

Under the premise that the damage in the specimen is related to the input mechanical energy during the fatigue process, strain energy density based damage parameter demonstrated good correlation with a wide range of experimental data in fatigue tests of metals (Ellyin, 1997). Due to the advantage of unifying both macroscopic and microscopic aspects of fatigue process, strain energy density approach also showed good performance in fatigue life prediction in uniaxial fatigue of this epoxy polymer in Chapter 3. Moreover, stress-strain relationship is inherently included in strain energy density based damage parameter. Therefore, strain energy density approach was also adopted to unify the multiaxial and uniaxial fatigue test results.

For fully-reversed uniaxial fatigue tests, the total strain energy density vs. fatigue life function was obtained in Chapter 3 (Eq.(3.27)). Fairly good agreement can be seen between current test results and previous uniaxial fatigue test results in Fig.4.10. The correlation coefficient of the uniaxial data points and the shear data points to the predictive curve, Eq.(3.27), is 0.984.

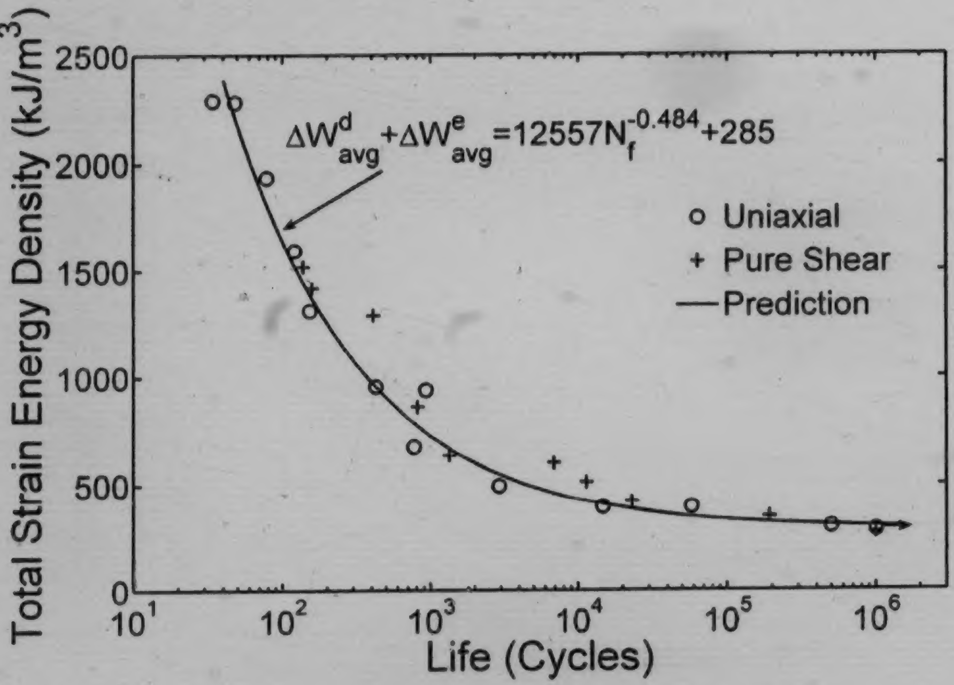

Fig. 4.10 Total strain energy density vs. fatigue life.

4.3 Proportional axial-shear fatigue tests with mean strains

4.3.1 Experimental procedure

Totally 16 multiaxial fatigue tests with mean strains were carried out under strain-range-controlled mode with equivalent loading rate of 10MPa/s. All the results are listed in Table 4.2, where the S1 series are pure shear tests, the S2 and S3 series are tests under combined proportional axial-shear loading with loading ratios of 1:1.1 and 1:0.7, respectively. The principle stresses in combined axial-shear loading condition can be obtained by:

$$\sigma_{1,2} = \frac{\sigma_x \pm \sqrt{\sigma_x^2 + 4\tau_{xy}^2}}{2} \tag{4.14}$$

where σ_x is the axial stress and τ_{xy} is the shear stress. Therefore, the principle stress ratio can be expressed as:

$$\frac{\sigma_2}{\sigma_1} = \frac{\dfrac{\sigma_x - \sqrt{\sigma_x^2 + 4\tau_{xy}^2}}{2}}{\dfrac{\sigma_x + \sqrt{\sigma_x^2 + 4\tau_{xy}^2}}{2}} \tag{4.15}$$

Substituting the loading ratios $\sigma_x/\tau_{xy} = 0:1$, $\sigma_x/\tau_{xy} = 1:1.1$ and $\sigma_x/\tau_{xy} = 1:0.7$ into Eq.(4.15), 3 different principle stress ratios can be obtained as -1(tg45°), -0.41(tg22.5°) and -0.27(tg15°) for S1, S2 and S3 series, respectively, as shown in Fig.4.11. Both axial mean strain ratio and shear mean strain ratio are controlled around 1 in all the above 3 groups of biaxial axial-shear fatigue tests. ($\varepsilon_{x,m}/\varepsilon_{x,a} \approx 1, \gamma_{xy,m}/\gamma_{xy,a} \approx 1$)

Table 4.2 Parameters and results of proportional axial-shear fatigue tests

No.	Axial						Shear						N
	$\varepsilon_{x,a}$ (%)	$\varepsilon_{x,m}$ (%)	$\sigma_{x,a}$ (MPa)	$\sigma_{x,m}$ (MPa)	$\Delta W^d_{x,avg}$ (kJ/ m^3)	$\Delta W^e_{x,avg}$ (kJ/ m^3)	$\gamma_{xy,a}$ (%)	$\gamma_{xy,m}$ (%)	$\tau_{xy,a}$ (MPa)	$\tau_{xy,m}$ (MPa)	$\Delta W^d_{xy,avg}$ (kJ/ m^3)	$\Delta W^e_{xy,avg}$ (kJ/ m^3)	(cycles)
S1-1	0	0	0	0	0	0	3.14	3.11	23.77	18.07	135.94	378.62	579
S1-2	0	0	0	0	0	0	3.02	2.99	22.94	17.82	121.38	353.60	803
S1-3	0	0	0	0	0	0	2.69	2.70	21.62	16.52	73.64	296.14	5850
S1-4	0	0	0	0	0	0	2.39	2.38	20.20	16.15	48.24	248.05	18621
S1-5	0	0	0	0	0	0	2.20	2.20	19.46	15.27	47.53	216.77	17371
S1-6	0	0	0	0	0	0	2.22	0.75	20.82	5.57	55.32	224.37	400000
S2-1	1.04	1.09	20.81	14.26	73.85	99.26	3.10	3.10	22.17	15.71	204.98	329.93	331
S2-2	0.72	0.76	16.90	14.41	27.58	58.14	2.20	2.34	17.72	15.91	67.53	197.41	896
S2-3	0.51	0.55	13.13	11.89	13.07	30.79	1.50	1.69	13.34	13.11	24.94	100.46	3968
S2-4	0.48	0.48	12.87	9.67	7.71	30.58	1.59	1.43	14.43	10.59	23.41	115.42	22782
S2-5	0.45	0.45	12.28	9.84	9.63	25.74	1.30	1.37	12.14	10.85	19.35	78.07	17463
S3-1	1.26	1.26	26.60	19.75	92.83	166.06	2.72	2.51	19.06	13.94	138.00	259.36	129
S3-2	1.04	1.04	24.66	19.05	51.89	127.64	2.15	2.10	16.90	13.48	62.17	187.98	737
S3-3	0.78	0.79	20.30	16.71	25.52	78.62	1.61	1.61	13.83	11.82	26.99	114.49	1634
S3-4	0.65	0.65	17.80	13.85	11.80	58.77	1.43	1.28	12.85	9.82	16.94	93.28	9652
S3-5	0.55	0.55	15.25	12.32	8.00	42.47	1.17	1.05	11.01	8.75	11.46	63.90	16320

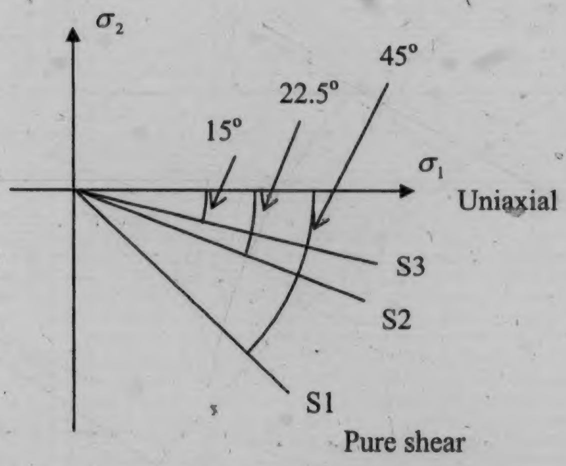

Fig. 4.11 Illustration of biaxial principle stress ratio.

4.3.2 Mechanical properties

Stress-strain data were recorded during the entire fatigue process for all the tests. The stress-strain loops of the first, the mid-life and the last cycle of a typical pure shear test (S1-5) are plotted in Fig.4.12. Quantitative mechanical components, such as the stress amplitude $\tau_{xy,a}$, strain amplitude $\gamma_{xy,a}$, mean stress $\tau_{xy,m}$, mean strain $\gamma_{xy,m}$, dissipated strain energy density ΔW_{xy}^{d} and elastic strain energy density amplitude ΔW_{xy}^{e} (demonstrated in Fig.1.16) were retrieved from the stress-strain data and plotted in Fig.13. It can be seen that the shear stress amplitude increased as the number of cycles increased. This is due to the phenomenon of combined effect of modulus drop and decrease of nonlinearity in stress-strain relation as discussed in Chapter 3. Distinct mean stress relaxation which is a typical phenomenon in strain-controlled or strain-range-controlled cyclic test can be observed. The stress-strain relation of the specimen became more linear after being cyclically loaded and it resulted in the decrease of dissipated strain energy density. While the elastic strain energy density amplitude kept almost constant during the entire fatigue process. It can also be noticed that the mechanical response of the specimen became much stable after the mid-life cycle.

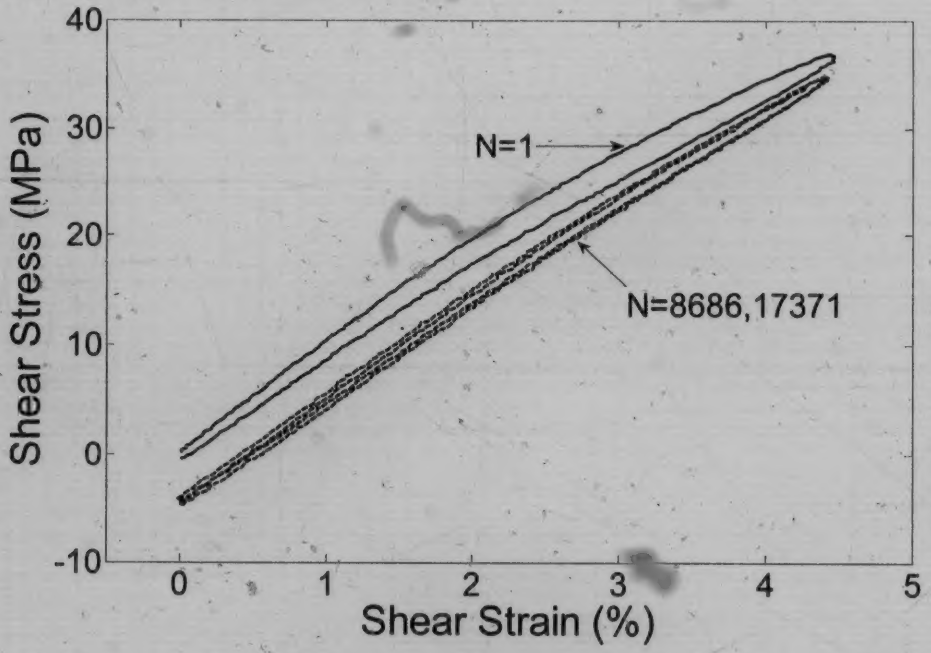

Fig. 4.12 Stress-strain loops of test S1-5

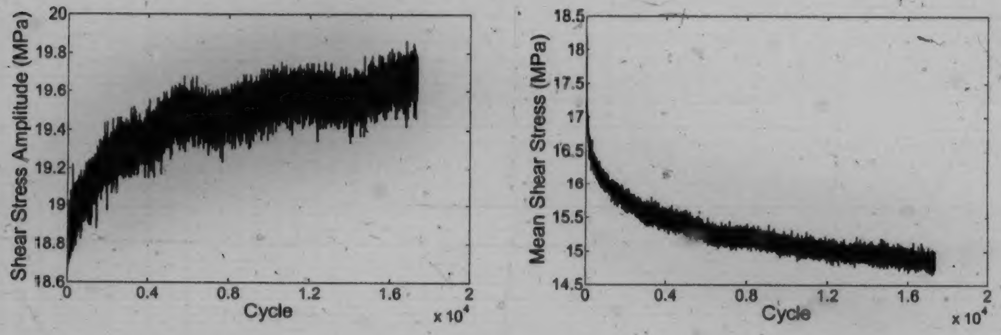

(a) (b)

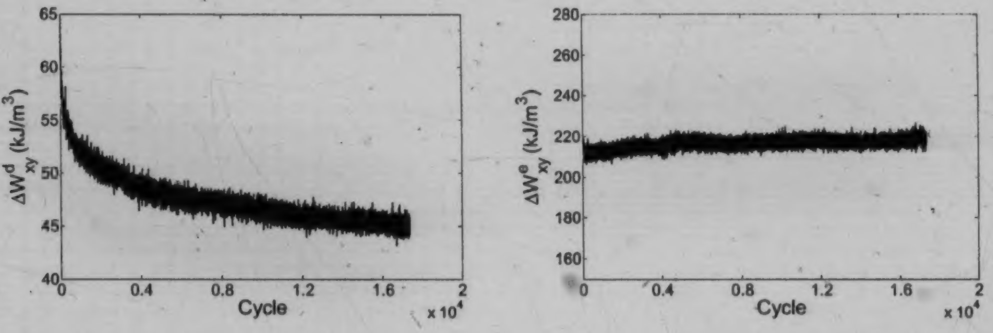

(c) (d)

Fig. 4.13 Evolution of mechanical components of test S1-5. (a) Stress amplitude; (b) Mean Stress; (c) Dissipated strain energy density; (d) Elastic strain energy density amplitude.

The first, the mid-life and the last cycle of stress-strain loops in axial and shear directions of a typical combined proportional axial-shear test (S3-2) are plotted in Fig.4.14 (a) and (b), respectively. And the retrieved mechanical components in axial (with subscript "x") and shear (with subscript "xy") directions are shown in Fig.4.15 and Fig.4.16, respectively. Again, slight increase of both axial and shear stress amplitudes can be noticed. Stress relaxations occurred in both axial and shear directions. Dissipated strain energy density in both axial and shear directions decreased due to the decrease of stress-strain nonlinearity which can be easily noticed in Fig.4.14. And the elastic strain energy density amplitudes kept almost unchanged. Nearly stable mechanical responses were achieved after mid-life cycle in both axial and shear directions. Mean values of the mechanical parameters (stress/strain amplitude, mean stress/strain, strain energy densities) of all the tests were chosen as the representative values and listed in Table 4.2.

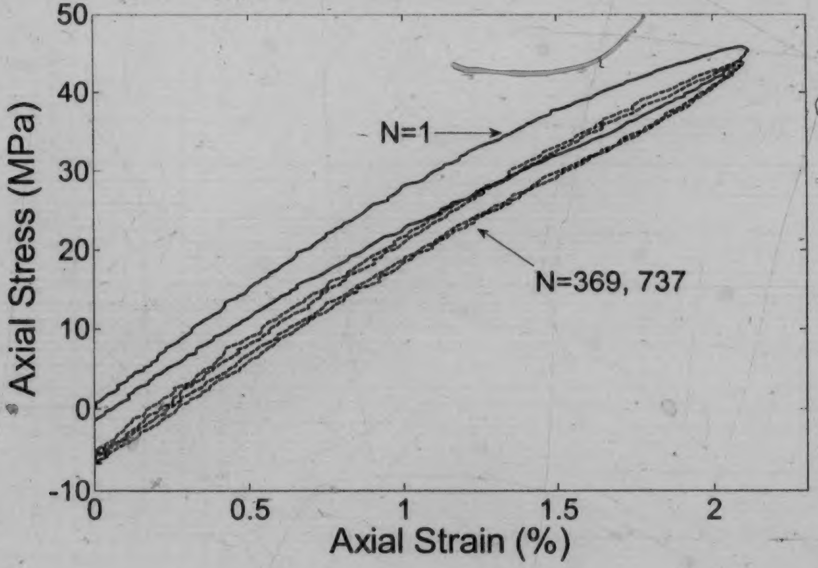

(a)

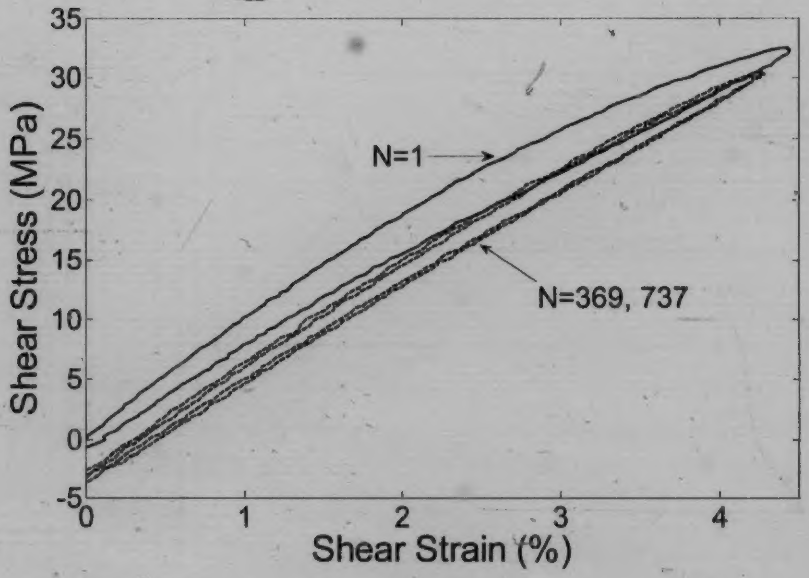

(b)

Fig. 4.14 Stress-strain loops of test S3-2. (a) Axial; (b) Shear.

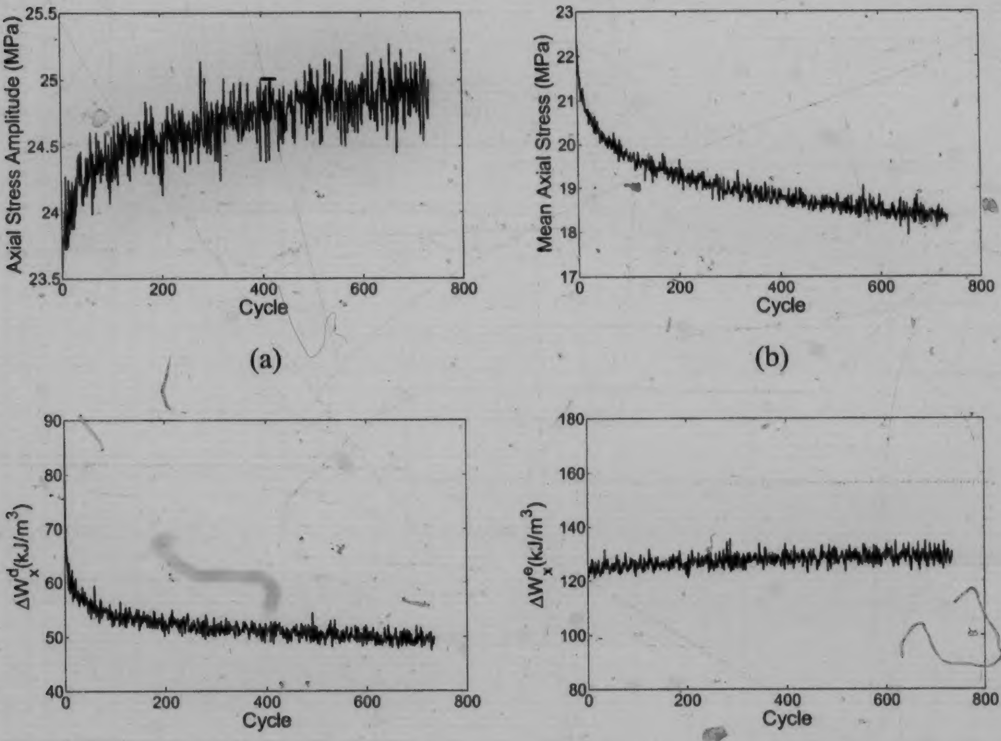

(a) (b)

(c) (d)

Fig. 4.15 Evolution of mechanical components of test S3-2 in axial direction. (a) Stress amplitude; (b) Mean Stress; (c) Dissipated strain energy density; (d) Elastic strain energy density amplitude.

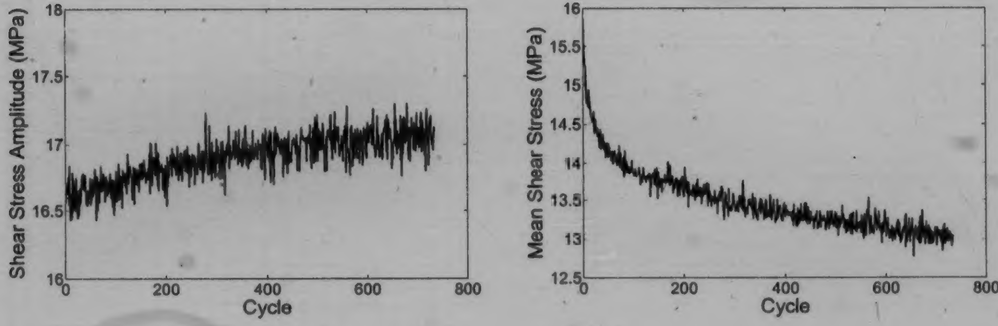

(a) (b)

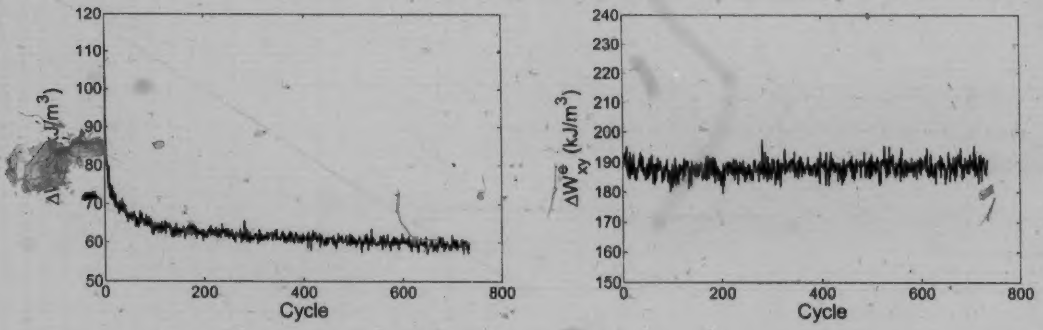

(c) (d)

Fig. 4.16 Evolution of mechanical components of test S3-2 in shear direction. (a) Stress amplitude; (b) Mean Stress; (c) Dissipated strain energy density; (d) Elastic strain energy density amplitude.

4.3.3 Fatigue life prediction with three approaches

Various multiaxial fatigue life prediction models have been proposed in the past decades. In general, they can be classified within three groups, stress-based, strain-based and energy-based. The so-called critical plane approach (Findley, 1959, McDiarmid, 1991, Fatemi et al., 1988, Jiang, 2000), which became popular in recent years, can also be regarded as special cases of stress-based or strain-based approaches depending on the parameters chosen. As in the previous fully-reversed pure shear fatigue test results, multiaxial fatigue life prediction was extended from the uniaxial models by adopting equivalent stress and strain as the governing parameters. Due to the unique property of asymmetry in tension and compression of this epoxy polymer, the Stassi criteria (Stassi-D'Alia, 1967) seems to perform better than the von Mises criteria in evaluating the equivalent stress and strain as shown in section 4.2 for fully-reversed cyclic pure shear fatigue test results. Therefore, in this section, Stassi equivalent stress/strain is adopted.

4.3.3.1 Equivalent Stress/Strain

The von Mises equivalent stress and the Stassi equivalent stress are expressed in Eq.(4.3) and (4.6), respectively. In the case of pure shear loading, the von Mises and the Stassi equivalent stresses can be simplified as Eq.(4.4) and (4.8), respectively. For proportional axial-shear loading, the von Mises and the Stassi equivalent stresses can be reduced as the following equations, respectively:

$$\sigma_{eq} = \sqrt{\sigma_x^2 + 3\tau_{xy}^2} \tag{4.16}$$

$$\sigma_{seq} = \frac{(R-1)\sigma_x + \sqrt{(R-1)^2\sigma_x^2 + 36R\sigma_{eq}^2}}{6R} \tag{4.17}$$

In strain-based approach, equivalent strain should be adopted for multiaxial loading. The von Mises equivalent strain is expressed in Eq.(4.11). Similar to the Stassi equivalent stress criteria, the Stassi equivalent strain can be expressed as:

$$\varepsilon_{seq} = \frac{(R-1)I_1^{\varepsilon} + \sqrt{(R-1)^2 I_1^{\varepsilon 2} + 4R\varepsilon_{eq}^2}}{2R} \tag{4.18}$$

where I_1^{ε} is the first invariant of the strain tenor, ε_{eq} is the von Mises equivalent strain. Then for pure shear loading, the von Mises and Stassi equivalent strains can be simplified as Eq.(4.12) and (4.13), respectively. And for proportional axial-shear loading, the von Mises and the Stassi equivalent strains can be reduced as the following, respectively.

$$\varepsilon_{eq} = \frac{1}{1+\upsilon}\sqrt{\varepsilon_x^2 + \frac{3}{4}\gamma_{xy}^2} \tag{4.19}$$

$$\varepsilon_{seq} = \frac{(R-1)\varepsilon_x + \sqrt{(R-1)^2\varepsilon_x^2 + 36R\varepsilon_{eq}^2}}{6R} \tag{4.20}$$

4.3.3.2 Mean Stress/Strain Effect

To consider the mean stress effect, a mean stress function was introduced in section 3.3 for uniaxial fatigue with mean stress:

$$f\left(\frac{\sigma_m}{\sigma_a}\right) = 1 + \eta_\sigma \frac{\sigma_m}{\sigma_a} \tag{4.21}$$

where σ_m is the mean stress, σ_a is the stress amplitude and η_σ is a material constant reflecting the sensitivity to the mean stress on fatigue life. Similarly, in the case of strain-based approach, the mean strain function was defined as:

$$f\left(\frac{\varepsilon_m}{\varepsilon_a}\right) = 1 + \eta_\varepsilon \frac{\varepsilon_m}{\varepsilon_a} \tag{4.22}$$

where ε_m is the mean strain, ε_a is the strain amplitude and η_ε is a materials constant reflecting the sensitivity to the mean strain on fatigue life.

To consider the mean stress/strain effect in multiaxial fatigue of the epoxy polymer, the Stassi criteria is adopted to evaluate the equivalent mean stress/strain and stress/strain amplitude, i.e. taking mean stress/strain or stress/strain amplitude components into

Eq.(4.6) and Eq.(4.18) to obtain the equivalent mean stress/strain and equivalent stress/strain amplitude, respectively.

Therefore, deriving from the uniaxial fatigue tests, fatigue life prediction models for multiaxial fatigue of the epoxy polymer are:

Stress approach: $$\left(1+\eta_{\sigma}\frac{\sigma_{seq,m}}{\sigma_{seq,a}}\right)\sigma_{seq,a}=192.6\cdot N_f^{-0.362}+35 \tag{4.23}$$

Strain approach: $$\left(1+\eta_{\varepsilon}\frac{\varepsilon_{seq,m}}{\varepsilon_{seq,a}}\right)\varepsilon_{seq,a}=0.1\cdot N_f^{-0.347}+1.3\% \tag{4.24}$$

Energy approach: $$\Delta W_{avg}^{d}+\left(1+\eta_{W}\frac{\sigma_{seq,m}}{\sigma_{seq,a}}\right)\Delta W_{avg}^{e}=12557\cdot N_f^{-0.484}+285 \tag{4.25}$$

where η_{σ}, η_{ε} and η_{W} were calibrated as 0.76, 0.55 and 2.35 in the case of uniaxial fatigue. ΔW_{avg}^{d} in Eq.(4.25) is the summation of dissipated strain energy density of both axial and shear part, $\Delta W_{x,avg}^{d}$ and $\Delta W_{xy,avg}^{d}$, respectively. And it is also the same with elastic strain energy density amplitude, i.e. $\Delta W_{avg}^{e}=\Delta W_{x,avg}^{e}+\Delta W_{xy,avg}^{e}$.

4.3.3.3 Hydrostatic Pressure Effect

As observed in the experiments, the sensitivity of mean stress/strain effect on fatigue life of this epoxy polymer was found to vary for different biaxial loading paths in Fig.4.11. From the uniaxial to pure shear loading (loading path S1), a decrease of mean stress effect was observed. This might be attributed to the difference in hydrostatic stress state of these different biaxial loading paths. Therefore, mean stress/strain sensitivity factors

η_σ, η_ε and η_W in Eq.(4.23-4.25) should be functions of the hydrostatic stress in the case of multiaxial fatigue. The hydrostatic stress ratio is therefore further defined as the ratio of the first invariant of stress tensor to the Stassi equivalent stress:

$$\chi = \frac{I_1^\sigma}{\sigma_{seq}} \tag{4.26}$$

Note that in the case of biaxial loading, Eq.(4.26) can be expressed as:

$$\begin{aligned} \chi &= \frac{\sigma_1 + \sigma_2}{\dfrac{(R-1)(\sigma_1+\sigma_2) + \sqrt{(R-1)^2(\sigma_1+\sigma_2)^2 + 2R\left[(\sigma_1-\sigma_2)^2 + \sigma_2^2 + \sigma_1^2\right]}}{2R}} \\ &= \frac{2R(1+\dfrac{\sigma_2}{\sigma_1})}{(R-1)\left(1+\dfrac{\sigma_2}{\sigma_1}\right) + \sqrt{(R-1)^2\left(1+\dfrac{\sigma_2}{\sigma_1}\right)^2 + 2R\left[\left(1-\dfrac{\sigma_2}{\sigma_1}\right)^2 + \left(\dfrac{\sigma_2}{\sigma_1}\right)^2 + 1\right]}} \end{aligned} \tag{4.27}$$

For each biaxial loading path (as shown in Fig.4.11), the values of mean stress/strain sensitivity factors η_σ, η_ε and η_W were determined by best fitting between the experimental data and the fatigue life prediction curves with stress-based, strain-based and energy-based approaches, respectively, and these values are marked in Fig. 4.17. Note that the most right points in Fig. 4.17 correspond to the uniaxial loading ($\chi = 1$) and the most left points ($\chi = 0$) correspond to the pure shear loading. From this figure one can see that as the biaxial stress state shifts from uniaxial to pure shear loading, the mean stress/strain sensitivity factors decreases. This could be attributed to the decrease of tensile hydrostatic stress, which usually facilitates the fatigue crack opening and therefore results in acceleration of crack propagation and reduction of fatigue life.

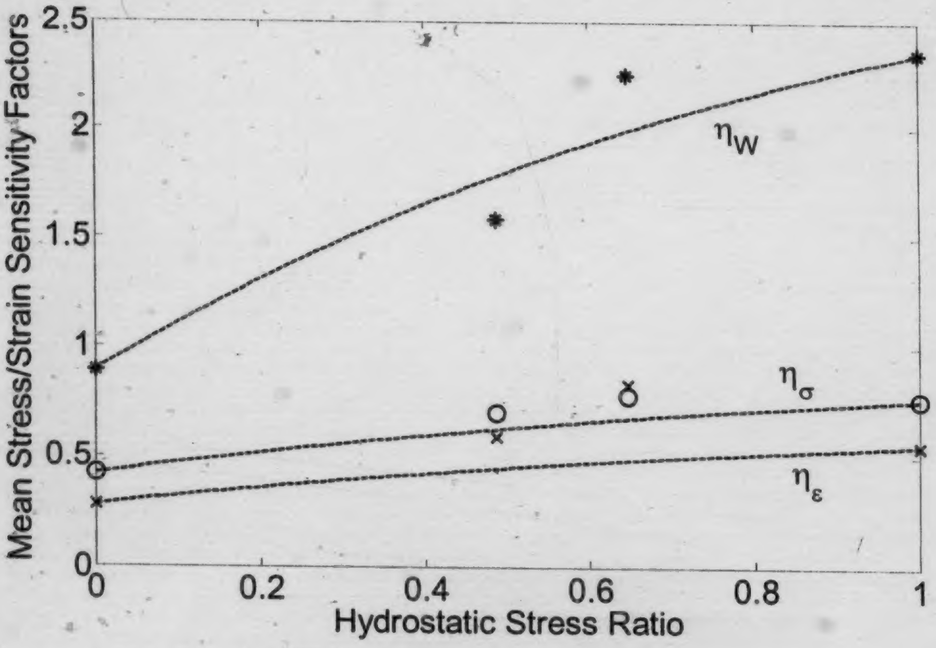

Fig. 4.17 Mean stress/strain sensitivity factors

From these data points in Fig.4.17, simple exponential functions are selected to reflect the variation of mean stress/strain sensitivity factors to the hydrostatic stress ratio as shown in the following equations 4.29-4.31. The two constants in each equation were simply determined based on the two values from the uniaxial and the pure shear test results.

$$\eta_\sigma = 0.96 - 0.54e^{-x} \tag{4.28}$$

$$\eta_\varepsilon = 0.71 - 0.43e^{-x} \tag{4.29}$$

$$\eta_W = 3.20 - 2.31e^{-x} \tag{4.30}$$

4.3.3.4 Fatigue Life Prediction

Fatigue life prediction curves with experimental data in the case of stress-based, strain-based and energy-based approaches are plotted in Fig.4.18, Fig.4.19 and Fig.4.20, respectively. Among these, stress-based and energy-based approaches yield good agreement between the prediction curves and the experimental data. While relatively large dispersion can be noticed in the strain-based approach, which could be attributed to its inability to include the effect of mean stress relaxation under strain-range-controlled test mode. The best prediction is observed with the energy-based approach and it could be due to the reason that the strain energy density inherently takes account of the stress-strain relation of the material.

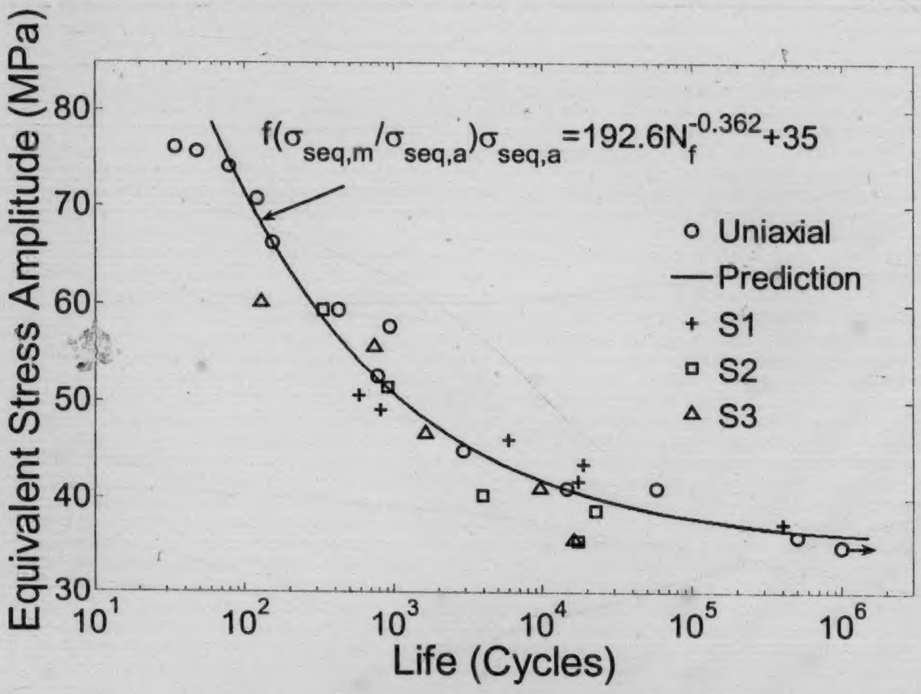

Fig. 4.18 Equivalent stress amplitude vs. fatigue life.

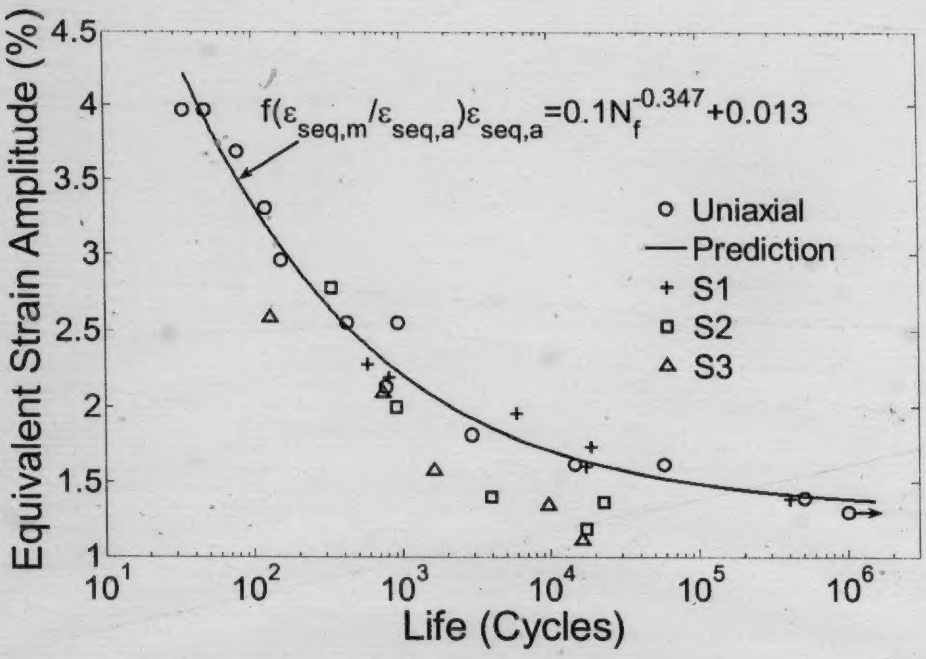

Fig. 4.19 Equivalent strain amplitude vs. fatigue life.

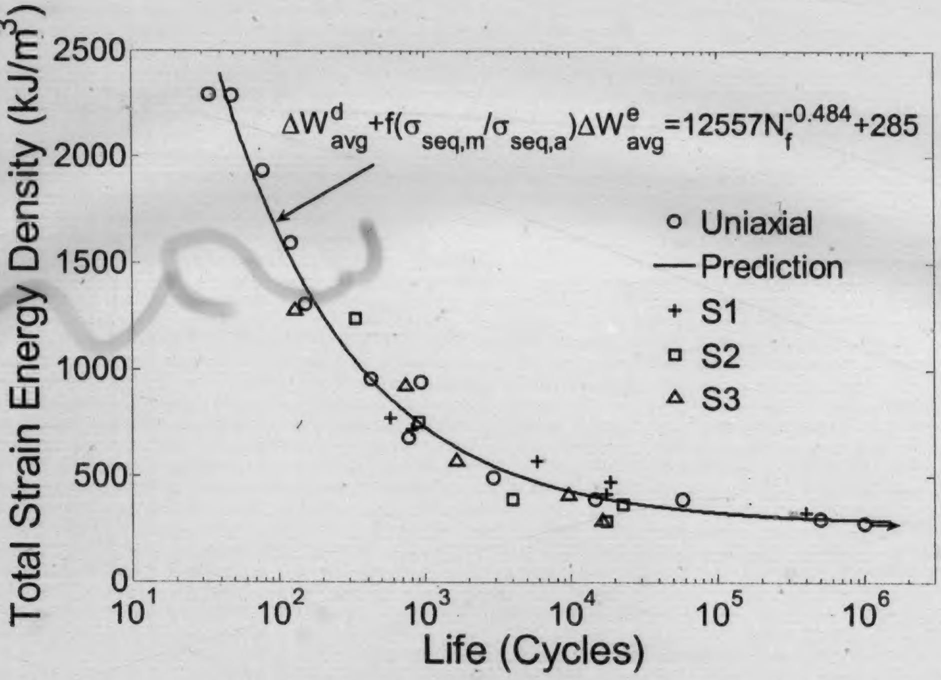

Fig. 4.20 Total strain energy density vs. fatigue life.

4.4 Conclusions

Strain-range-controlled fatigue tests of tubular specimens made of an epoxy polymer were conducted under cyclic shear loading and proportional axial-shear combined loading with and without mean strains. The stress-strain data were measured and recorded by a non-contact real-time strain measurement and control system during the entire fatigue process. Quantitative results of various mechanical parameters, such as shear modulus, stress/strain amplitudes, mean stress/strain and strain energy densities were retrieved from the stress-strain data. Fatigue life predictions were performed with the stress-, strain- and energy-based approaches by comparing with previous uniaxial fatigue test results. In the stress-based and strain-based approaches, Stassi criteria seems to perform better than von Mises criteria in evaluating equivalent stress/strain for this epoxy polymer which exhibits asymmetry in tensile and compressive mechanical behavior. Mean stress/strain effect was also included in the damage parameters by incorporating the mean stress/strain functions. It was observed that as the biaxial stress state shifts from pure shear to uniaxial ones, the mean stress/strain effect increases. This could be due to the increase of tensile hydrostatic stress, which usually facilitates fatigue crack opening, crack propagation and reduction of failure life. The mean stress/strain sensitivity factors as functions of hydrostatic stress ratio were calibrated. In the fully-reversed cyclic shear fatigue tests, all the three approaches yield good predictions for both the uniaxial and biaxial experimental data. In biaxial fatigue tests with mean strains, good agreement between the prediction curve and experimental data were obtained in stress-based and energy-based approaches, among which the energy-based approach showed the best performance. Relatively large dispersion was observed in the strain-based approach and it could be due to its inability to include the effect of mean stress relaxation. It should be pointed out that the calibration of the mean stress/strain functions in this study was based on test results of the four proportional stress paths shown in Fig.4.11 only. Further experimental studies are required to determine whether these mean stress function relations are appropriate to be extended to more wide range of multiaxial stress/strain combinations such as the cases with more detrimental equi-biaxial tensile mean stress or with beneficial compressive mean stress.

Bibliography

1. Chen X, Song J, Kim KS. Fatigue life of 63Sn-37Pb solder related to load drop under uniaxial and torsional loading. Int J Fatigue 2006; 28(7):767-76.
2. de Freitas M, Reis L, Li B. Comparative Study on biaxial low-cycle fatigue behavior of three structural steels. Fatigue Fract Engng Mater Struct 2006; 29(12):992-9.
3. Ellyin F. Fatigue Damage, Crack Growth, and Life Prediction. Chapman & Hall, London, UK. 1997.
4. Fatemi A, Socie DF. A Critical plane approach to multiaxial fatigue damage including out of phase loading. Fatigue Fract Eng Mater Struct 1988; 11:149-65.
5. Findley WN. A theory for the effect of mean stress on fatigue of metals under combined torsion and axial load or bending. J Engng Ind Trans ASME 1959; 81:301-6.
6. Gude M, Hufenbach W, Koch I, Protz R. Fatigue failure criteria and degradation rules for composites under multiaxial loadings. Mechanics of Comp Mater 2006; 42(5):443-50.
7. Isayev AI.., Katz D, Smooha Y. Dynamic properties of crosslinked epoxy resin at large cyclic and static deformation. Polym Eng Sci 1981; 21(9):566-70.
8. Jiang Y. A fatigue criterion for general multiaxial loading. Fatigue Fract Eng Mater Struct 2000; 23:19-32.
9. Lease K, Stephens R, Jiang Y, Kurath P. Fatigue of a particulate reinforced aluminium metal matrix composite subjected to axial, torsional and combined

axial/torsional loading conditions. Fatigue Fract Engng Mater Struct 1996; 19(8):1031-43.

10. Lee D, Kim J, Hwang H. Torsional fatigue characteristics of aluminum-composite co-cured shafts with axial compressive preload. J Composite Mater 2004; 38(9):737-56.
11. Li Y, Zhang K, Zhang B. Shear fatigue test and life prediction of composite laminates. Key Eng Mater 2003; 243-2:63-68.
12. Marquis G, Socie D. Long-life torsion fatigue with normal mean stresses. Fatigue Fract Engng Mater Struct 2000; 23(4):293-300.
13. Mayer H. Ultrasonic torsion and tension-compression fatigue testing: Measuring principles and investigations on 2024-T351 aluminium alloy. Int J Fatigue 2006; 28(11):1446-55.
14. McDiarmid DL. A general criterion for high cycle multiaxial fatigue failure. Fatigue Fract Engng Mater Struct 1991; 14(4):429-53.
15. Qi D, Cheng G. Fatigue behavior of filament-wound glass fiber reinforced epoxy composite tubes under tension/torsion biaxial loading. Polym Comp 2007; 28(1):116-23.
16. Stassi-D'Alia F. Flow and Fracture of Materials According to a New Limiting Condition Yielding. Meccanica 1967; 3:178-95
17. Xia Z, Hu Y, Ellyin F. Deformation Behavior of an Epoxy Resin Subject to Multiaxial Loadings. Part II: Constitutive Modeling and Prediction. Polym Eng Sci

2003; 43(3):734-48.

Chapter 5

Summary

The objective of this thesis was to investigate the fatigue behavior of an EPON 826/EPI-CURE Curing Agent 9551 polymer system under various uniaxial and multiaxial loading conditions. The results of this research provide fundamental understanding of the polymer's fatigue mechanism and valuable references of life prediction models for load-bearing components made of epoxy polymers or of fiber-reinforced epoxy matrix composites, in which, as in most cases, fatigue crack initiate within the relative weak matrix phase or fiber-matrix interface. The established experimental facility and strategy would also provide an effective fatigue test platform for various polymeric materials.

The full research project included designing the fatigue testing system and test strategy, conducting uniaxial and multiaxial fatigue tests under various loading conditions and establishing multiaxial fatigue life prediction models.

1. Fatigue Testing System

A non-contact real-time strain measurement and control system based on Digital Image Correlation Method was successfully established for fatigue test of soft materials, such as polymers (Tao et al., 2005). It possesses superior advantage over traditional strain measurement devices, such as extensometers, which usually introduce considerable stress concentration on the surface of the specimens and accelerate failure. By tracking the in-plane displacements of the pre-painted marks on the surface of the specimen, this system is able to simultaneously measure the strains in two dimensions, i.e. axial strain and shear strain. Therefore, it is well suited for multiaxial fatigue test. High strain measurement resolution is obtained as of 0.002%, which is comparable to traditional extensometers. A high data acquisition frequency of 60Hz is achieved based on current computer and camera system. With the rapid development of computer and image sensor technologies, a potential increase of measurement precision and acquisition frequency of the system can be expected.

Since strain can be measured in real-time, strain-range-controlled fatigue tests can be performed with this system. In strain-range-controlled mode, the measured strain is compared to the predefined upper and lower strain range in real-time. If the strain exceeds the predefined range, the load direction will be reversed. In strain-range-controlled mode, the ratcheting strain is restrained and therefore possible ratcheting effect on fatigue life can be eliminated.

2. Uniaxial and multiaxial fatigue tests with fatigue life prediction models

Fully-reversed uniaxial fatigue tests have been carried out under strain-range-controlled mode to obtain the basic fatigue life prediction curves in stress-, strain- and energy-based approaches.

Quantitative results on the evolution of mechanical properties, such as modulus, stress/strain range, mean stress/strain, nonlinear strain, dissipated strain energy density and elastic strain energy density amplitude were retrieved from the stress-strain data. Modulus drop and decrease of nonlinearity of stress-strain relation were found to be two basic phenomena during fatigue process of the epoxy polymer. And the evolution of the other mechanical components can be attributed to the combined effect of these two factors (Tao et al., 2007a).

Mean stress/strain effect in uniaxial fatigue was identified by performing strain-range-controlled fatigue tests with various mean strain ratios (Tao et al., 2007c). Mean stress/strain functions were introduced in the damage parameters of fatigue life prediction models in three approaches and the mean stress/strain sensitivity factors were calibrated.

To investigate the ratcheting strain effect, uniaxial fatigue tests were performed under stress-controlled mode with mean stresses (Tao et al., 2007d). However, no distinct ratcheting strain effect on fatigue life was observed, although it has been identified in most metals. This could be attributed to the different mechanism of ratcheting strain in metals and epoxy polymers. The ratcheting strain in the epoxy polymer is mainly recoverable viscoelastic strain, which may not introduce considerable damage, while the plastic ratcheting strain in metals would cause slippage and dislocation in the microstructure of metals and therefore leads to damage.

Multiaxial fatigue behavior of this epoxy polymer has been studied by performing pure shear tests (Tao et al., 2007b) and combined axial-shear tests under strain-range-controlled mode. By adopting the equivalent stress/strain concept, good agreement was found between uniaxial fatigue and fully-reversed pure shear fatigue test results in stress- and strain-based approaches. In addition, the Stassi criteria seem to perform better in evaluating equivalent stress/strain of materials that exhibits asymmetric mechanical response in tension and compression. Good fatigue life predictions were also obtained by energy-based approach.

In combined axial-shear fatigue tests, it was found that the sensitivity of fatigue life to mean stress/strain decreases from uniaxial stress state to pure shear stress state. Mean stress/strain sensitivity factors were calibrated as functions of hydrostatic pressure ratio and incorporated into the damage parameters in stress-, strain- and energy-based fatigue life prediction models. Good results were obtained from stress-based and energy-based approaches. While relatively large dispersion was observed with the strain-based approach. This could be attributed to its inability to account for the mean stress relaxation in strain-range-controlled fatigue tests.

3. Recommendations for future work

In addition to current investigations, continuing researches are required in the following topics:

a) The effect of compressive mean stress on fatigue life of the epoxy polymer under both uniaxial and multiaxial loading conditions. The mean stress/strain functions should be extended to compressive mean stress/strain conditions.

b) Multiaxial fatigue behavior of the epoxy polymer under equi-biaxial loading conditions. Sensitivity of mean stress/strain effect to hydrostatic pressure needs to be further verified.

c) Fatigue behavior of the epoxy polymer under non-proportional multiaxial loading conditions.

Bibliography

1. Tao G, Xia Z. A non-contact real-time strain measurement and control system for multiaxial cyclic/fatigue tests of polymer materials by digital image correlation method. Polymer Testing, 2005; 24(7):844-55.
2. Tao G, Xia Z. An experimental study of uniaxial fatigue behavior of an epoxy resin by a new non-contact real-time strain measurement and control system. Polym Eng Sci, 2007a; 47(6):780-8.
3. Tao G, Xia Z. Fatigue behavior of an epoxy polymer subjected cyclic shear loading. Materials Science and Engineering A, 2007b. In Press.
4. Tao G, Xia Z. Mean stress/strain effect on fatigue behavior of an epoxy resin. Int J Fatigue, 2007c. In Press, doi:10.1016/j.ijfatigue.2006.12.009.
5. Tao G, Xia Z. Ratcheting behavior of an epoxy polymer and its effect on fatigue life. Polym Testing, 2007d; 26(4):451-60.